INTENSE FIELD ELECTRON EXCITATION IN TRANSPARENT MATERIALS

DISSERTATION

Presented in Partial Fulfillment of the Requirements for

the Degree Doctor of Philosophy in

the Graduate School of The Ohio State University

By

Georgia C. Modoran, B.S., M.S.

* * * * *

The Ohio State University

2005

Dissertation Committee:

Professor Douglass Schumacher, Advisor

Professor Dongping Zhong

Professor Eric Herbst

Professor Frank C. De Lucia

Approved by

_____

Advisor
Graduate Program in Physics

ABSTRACT

The propagation of an intense laser through transparent materials can only be understood by considering a wide range of nonlinear effects and their simultaneous interaction. Electron plasma formation plays a crucial role and is the focus of this work. The mechanisms of the nonlinear ionization are not well understood. There are two proposed interactions that contribute to electron plasma formation: photoionization and avalanche ionization, but the individual contribution of each of these ionization processes is controversial. Keldysh theory has been proposed as a description of photoionization. Two models for avalanche ionization are used in the literature, but with different intensity dependence. We address and resolve these issues.

In this thesis we present a spectrally resolved pump-probe experiment that directly measures the nonlinear ionization rates and plasma evolution in solid state media. Both pump and probe are derived from an 800 nm, 120 fs laser. The maximum ionization rates were obtained in sapphire ($\sim 1.9\times10^{18}$ $fs^{-1}\cdot cm^{-3}$), while in water ($\sim 7.2\times10^{17}$ $fs^{-1}\cdot cm^{-3}$), fused silica ($\sim 8.6\times10^{17}$ $fs^{-1}\cdot cm^{-3}$) and methanol ($\sim 6.6\times10^{17}$ $fs^{-1}\cdot cm^{-3}$) the ionization rates were slightly different.

Our measured ionization rates are consistently larger that the theoretical rate given by Keldysh theory, suggesting that this theory does not correctly describe the photoionization process.

We also present measurements that separate the two excitation processes and identify the role played by each in the ionization of media. The idea underneath these experiments is a very simple one: since the two ionization processes have different intensity dependence, the absorption of light in the medium should differ similarly. Therefore it should be possible to distinguish the two mechanisms by looking at the energy dependence of the absorption. From our result we find that avalanche and multiphoton ionization have varying relative contributions, depending on the band gap. For example, in sapphire (band gap ~ 9.0 eV) avalanche accounts for 70% whereas in methanol (band gap ~ 6.5 eV) contributes only 15%.

ACKNOWLEDGMENTS

Many people stood by me throughout the graduate school years. I am grateful to each of them.

First, this work could not been done without the support of my adviser, Douglass Schumacher. He has constantly encouraged and guided me through all these years. His friendship is something I will always value.

Next, I would like to thank my former lab mates Kenn Bates and Jennifer Tate for their encouragement and for never-failing to improve my English. Kenn has done an exceptional job in teaching me, when I first joined the lab, all the details of the project we worked on. He was always ready to listen to me in difficult times and to talk physics when I needed it. Thank you for being there. Jennifer and I were, at some point, the only grad students in the lab. It was she who was there to discuss the every day problems and make the grad student life a bit more fun. The work in this thesis is based on an experiment she first studied. Her insight was very useful in understanding some of the physics behind this thesis. Your help is being appreciated.

I wish to sincerely thank Tom Kelch - who always gave me invaluable help and advice and Kent Ludwig, in the low temperature shop, - who promptly solved various technical problems. I would also like to thank Brenda Mellet who went out of her way to assist and help.

Mada, Cristi, Camelia – you have been my support through many days. Your friendship is deeply appreciated. My good and old friends Diana, Florin, Gabi – I will never forget our days in Magurele.

Nothing I have done so far in my life would have been possible without the love of my family. They are far away from here, but always in my heart. Finally, all my love goes to my husband, Andrei. There is no one like you.

VITA

1997 ……...……	B.S. Physics, University of Bucharest – Romania
1998……	M.S., Physics University of Bucharest – Romania
1998-1999 ……..……...	Research Assistant, National Institute for Laser, Plasma and Radiation Physics, Bucharest, Romania
1999-present ……...……..…	Graduate Teaching and Research Assistant Physics Department The Ohio State University

PUBLICATIONS

"Highly perturbed States of Barium in an Electric Field", K. Bates, C. Vasilescu (Modoran), J.Masae and D. Schumacher, Phys.Rev.A. 64, 033409 (2001).

FIELD OF STUDY

Major Field: Physics

TABLE OF CONTENTS

LIST OF TABLES

LIST OF FIGURES

CHAPTER 1

INTRODUCTION

When a powerful ultrashort laser pulse propagates through an optical medium, self-focusing[3,11] and ionization occur and the intensity inside the material is clamped down to a high but limited value ($\sim 1.5 \cdot 10^{13}$ W/cm^2 in solids). The spectrum of the pulse broadens dramatically (supercontinuum generation[3,31,33]) from the near ultraviolet to the near infrared and the pulse emerges as white light. The spectral width depends on the properties of the media (ionization potential or band gap). These physical phenomena are universal and they manifest equally in gases, liquids and solids. The properties of filamentation, nonlinear ionization and self-transformation (that includes other phenomena such as self-phase modulation and self-steepening) constitute a challenging topic of research in physics and also have important practical applications. Tightly focused ultrashort pulses can be used to precisely deposit energy inside the bulk of transparent materials producing permanent material changes[18,19,20,21,22,23] at the focus. This is a feature that cannot be matched by any other technique. Notably, there have been

demonstrated direct writing of optical waveguides [33] and other optical devices [33] and the disruption of sub-cellular structures inside single cells. [33] The white light, which is one of the most extraordinary examples of the difference between the interaction of ultrashort, powerful lasers and normal light with transparent materials, has important practical applications. The white light is a widely used light source. When a short pulse propagates in the atmosphere, for example, it can be considered as a lamp in the air. [68] This lamp has been used to induce absorption of various types of pollutant molecules in the atmosphere [69]. Other applications include optical short pulse generation [70], high speed communications [71] and time/frequency metrology. [72,73]

This thesis is concerned with the highly nonlinear interaction between intense femtosecond lasers and transparent materials and it focuses on nonlinear ionization. In a transparent material there is no linear absorption of the low energy incident light. If the laser intensity is high enough, electrons can be promoted from the valence band to the conduction band of the material by nonlinear processes. Despite extensive research on the nonlinear ionization mechanisms, much still remains unclear. This thesis proposes an experimental technique, based on the plasma-induced blue shifting, which separates the ionization process from all the other competing nonlinear phenomena and allows a real time and precise measurement of the ionization rates, in a solid, while the laser is propagating through the material. We use the experimentally measured ionization rates to identify which ionization process (multiphoton ionization, avalanche ionization or both) contribute to the generation of free electrons inside the solid. Another simple, absorption experiment makes possible the separation of the individual contribution of each of the ionization processes involved. Also, a prism technique experiment allows easy access to

directly measuring the length of the light filament and the plasma dynamics. These processes are precisely monitored in real time over a wide range of path lengths. We find that the supercontinuum generation, the plasma formation, self-focusing, self-phase modulation and all the other nonlinear processes involved in the ultrashort laser propagation require a threshold propagation distance of 50 μm. We also measured a light filament of 1.8 mm – 2.0 mm.

This thesis is organized as it follows. **Chapter 2** discusses some theoretical aspects such as the linear and nonlinear propagation of the electromagnetic waves in materials, self-focusing and self-phase modulation. Nonlinear ionization mechanisms and a short introduction on Keldysh theory are also presented. Drude plasma model is introduced in this chapter and the plasma frequency, plasma absorption and plasma defocusing are discussed. The chapter also includes subsections that make a short review of the other nonlinear processes involved in the ultrashort laser propagation (white light, self-steepening, space-time focusing) and of the short pulse laser system. **Chapter 3** describes the measurements of the nonlinear ionization rates in four solid state media (sapphire, fused silica, water and methanol). A pump-probe technique and the concept of plasma induced blue shifting are introduced. The experimentally measured peak ionization rates and the peak densities for each material are compared to theoretical results as given by the Keldysh theory. **Chapter 4** is a review of the experiments that directly or indirectly dealt with the problem of ionization in the field of ultrashort, powerful laser pulses and discusses the results and conclusions obtained from these experiments. **Chapter 5** addresses a simple absorption experiment that looks at the nonlinear absorption of light at different colors in a sapphire sample. Multiphoton

ionization followed by the avalanche ionization is observed and the relative contribution of the two processes to the ionization is discussed. **Chapter 6** presents a prism technique that allows a real time monitoring of the plasma dynamics at various propagation distances. Measurements such as the supercontinuum generation threshold distance, plasma induced blue shifting and the filament lengths are discussed. Finally, **Chapter 7** draws a brief conclusion on the work described in the thesis.

CHAPTER 2

INTERACTION OF ULTRAFAST LASER PULSES WITH TRANSPARENT MATERIALS

2.1 Ultrashort Laser Propagation

2.1.1 Introduction

Chapter 2 discusses some theoretical background necessary to understand phenomena described in all subsequent chapters. Processes such as linear and nonlinear propagation of electromagnetic waves in materials, self-focusing and self-phase modulation are discussed. Nonlinear ionization mechanisms and a short introduction to Keldysh theory are also presented. Drude plasma model is introduced in this chapter and the plasma frequency, plasma absorption and plasma defocusing are discussed. The chapter ends with two subsections that make a short review of the other nonlinear

processes involved in the ultrashort laser propagation (white light, self-steepening, space-time focusing) and of the short pulse laser system. SI units are used throughout this work unless stated otherwise.

2.1.2 Linear Propagation

The interaction of the electromagnetic waves with matter is described by Maxwell's equations[1]

$$\vec{\nabla} \times \mathbf{E} = -\frac{\partial}{\partial t}\mathbf{B}$$

$$\vec{\nabla} \times \mathbf{H} = \mathbf{J} + \frac{\partial}{\partial t}\mathbf{D}$$

$$\vec{\nabla} \cdot \mathbf{D} = \rho$$

$$\vec{\nabla} \cdot \mathbf{B} = 0$$

along with the material equations[1]

$$\mathbf{J} = \sigma \mathbf{E}$$

$$\mathbf{D} = \varepsilon_0 \mathbf{E} + \mathbf{P}$$

$$\mathbf{H} = \frac{1}{\mu_0}\mathbf{B} - \mathbf{M}.$$

Throughout this work we will consider materials with no intrinsic free carriers, no conductivity and no magnetization. Therefore ρ, σ and $\mathbf{M}$ are taken to be zero. Combining the four Maxell's equations and taking into account only the dipole response of the material, we obtain the wave equation:

$$\vec{\nabla} \times \vec{\nabla} \times \mathbf{E}(\mathbf{r}, t) + \frac{1}{c^2} \frac{\partial^2}{\partial t^2} \mathbf{E}(\mathbf{r}, t) = \frac{-1}{\varepsilon_0 c^2} \frac{\partial^2}{\partial t^2} \mathbf{P}(\mathbf{r}, t).$$

In optics it is adequate to consider only the interaction of the material with the electric field since the effect of the magnetic field is negligible. When the electric field is significantly less than the field that binds the valence electrons to their ions (typical atomic fields are of the order of 10^9 V/cm), the relation between the response of the media, given by the induced dipole moment or polarization **P**(**r**, t), and the electric field is linear:

$$\mathbf{P}(\mathbf{r}, t) = \varepsilon_0 \tilde{\chi}^{(1)} \mathbf{E}(\mathbf{r}, t)$$

where $\tilde{\chi}^{(1)}$ is the linear susceptibility tensor. The quantities mathematically described by tensors will be indicated by the use of the symbol tilde. Both **E**(**r**, t) and **P**(**r**, t) are complex quantities. We assume that the response of the material is instantaneous (no ferroelectric effect). For an isotropic material the linear susceptibility is a scalar quantity and it is related to the refractive index n of the medium:

$$n = \sqrt{1 + \chi^{(1)}} \ .$$

The refractive index of any material is not a constant at all but is a function of frequency. This means that it has different values for propagating waves at different frequencies. In the most general case the refractive index is:

$$n = n_0 + i\alpha \ .$$

The real part of the refractive index (n_0) is related to dispersion while the imaginary part (α) describes the absorption. Let's look at the physical meaning of n_0 and α by looking

at an electromagnetic wave traveling through a medium with such an index. For simplicities' sake, we do it one-dimensional:

$$E(z,t) = E_0(z,t)\cdot \exp i\cdot(k_z z - \omega t)$$

$$= E_0(z,t)\cdot \exp i\cdot\left(\frac{(n_0 + i\alpha)\omega}{c} - \omega t\right)$$

$$= E_0(z,t)\cdot \exp\left(-\frac{\alpha\omega}{c}\right)\cdot \exp\left(\frac{n_0\omega}{c} - \omega t\right).$$

The real part of the refractive index gives the factor by which the phase velocity is reduced in the medium, and the imaginary party shows that the amplitude of the wave is attenuated exponentially as it propagates.

2.1.3 Nonlinear Propagation

When the electric field of the light is high enough, the interaction between light and the material can no longer be described through a linear relation. In other words, any real physical oscillating system exhibits a nonlinear response when it is overdriven. The polarization must be expanded in terms of sequentially higher order in the field strength: [2,3,4]

$$\mathbf{P} = \varepsilon_0 \tilde{\chi}^{(1)}\mathbf{E} + \varepsilon_0 \tilde{\chi}^{(2)}\mathbf{EE} + \varepsilon_0 \tilde{\chi}^{(3)}\mathbf{EEE} + \ldots$$

$$= \mathbf{P}^{(1)} + \mathbf{P}^{(2)} + \mathbf{P}^{(3)} + \ldots$$

The quantities $\tilde{\chi}^{(n)}$ with $n>1$ are known as the n-th order nonlinear optical susceptibilities and $\mathbf{P}^{(n)}$ as the n-th order nonlinear polarizations. The tensor nature of the nonlinear susceptibilities resides in the fact that because of the molecular or lattice

structure of materials, the nonlinear response will in general depend on the state of the polarization of the optical fields.[7] The above equation is not rigorously correct because it assumes the response is instantaneous. However, for the case of bound-electronic nonlinearity this assumption is valid because the response is very fast (the time scale is femtoseconds).[7] According to the wave equation, a time-varying polarization can act as a source of new frequency components in the electric field. Each of the nonlinear polarization terms gives rise to a series of physical processes. If we propagate two driving fields $\mathbf{E}^{(1)}$ at frequency ω_1 and $\mathbf{E}^{(2)}$ at frequency ω_2 and assume that the two fields are linearly polarized, so that $\tilde{\chi}^{(2)}$ is a scalar, then second-order nonlinear polarization can have various frequency components:[3]

$$\mathrm{P}^{(2)}(2\omega_1) \sim \chi^{(2)}\mathrm{E}_1^2$$

$$\mathrm{P}^{(2)}(2\omega_2) \sim \chi^{(2)}\mathrm{E}_2^2$$

$$\mathrm{P}^{(2)}(\omega_1+\omega_2) \sim 2\chi^{(2)}\mathrm{E}_1\mathrm{E}_2$$

$$\mathrm{P}^{(2)}(\omega_1-\omega_2) \sim 2\chi^{(2)}\mathrm{E}_1\mathrm{E}_2^*$$

$$\mathrm{P}^{(2)}(0) \sim 2\chi^{(2)}(\mathrm{E}_1\mathrm{E}_1^* + \mathrm{E}_2\mathrm{E}_2^*).$$

The first two terms describe second-harmonic generation; the next two terms give rise to sum-frequency generation and difference-frequency generation, respectively. The last equation describes optical rectification. However, in order to generate radiation via these terms using macroscopic media, the input and output fields must be correctly phased or "phase matched". For example, assume that the sample has a certain number of atoms and that each atom develops an electric dipole that oscillates at the frequency $2\omega_1$. The emitted light has a different frequency from the driving field and therefore a different

phase velocity. It turns out that a significant transfer of energy from the driving field to the new wave happens only when the phase velocities are equal. In order to obtain this condition a birefringent material is angle-tuned or temperature-tuned.[3,5]

The number of possible nonlinear terms is even higher for the third-order nonlinear polarization and they result in different physical phenomena such as the intensity-dependent refractive index, two-photon resonant absorption, third-harmonic generation and, more generally, four-wave-mixing.

2.2 Third Order Nonlinear Effects in Centrosymmetric Media

Many crystals, liquids, gases and amorphous solids display inversion symmetry.[3] In this thesis we will only be concerned with materials that have this property. They are referred to as centrosymmetric media. In these materials all the even-order terms from the polarization expansion vanish, including the second-order nonlinear polarization. For systems with inversion symmetry we have upon inversion $\mathbf{P}^{(2)} \rightarrow -\mathbf{P}^{(2)}$, $\mathbf{E} \rightarrow -\mathbf{E}$, but $\tilde{\chi}^{(2)} \rightarrow \tilde{\chi}^{(2)}$. Thus, after inversion we must have:

$$-\mathbf{P}^{(2)} = \varepsilon_0 \tilde{\chi}^{(2)}(-\mathbf{E})(-\mathbf{E}) = \mathbf{P}^{(2)}.$$

We see that the above equation can be satisfied only when $\mathbf{P}^{(2)} = 0$, which means $\tilde{\chi}^{(2)} = 0$. In order to simplify the equations we assume that the material is isotropic, which means that **P** and **E** are parallel vectors (and we can drop the vector notation) and that $\tilde{\chi}^{(3)}$ is a scalar. The total polarization has the form:[6]

$$\mathrm{P} = \mathrm{P}^{(1)} + \mathrm{P}^{(3)}$$

$$= \varepsilon_0 \chi^{(1)} \mathrm{E} + \frac{3}{4} \varepsilon_0 \chi^{(3)} |\mathrm{E}|^2 \mathrm{E}.$$

The term involving $\chi^{(3)}$ implies that three optical waves interact in order to produce a fourth one. Therefore a $\chi^{(3)}$-process is a four-photon process. The third-order polarization term alone leads to 81 terms corresponding to all possible permutations of the fields at three different frequencies. This does not mean that there are 81 distinct processes involved. The 81 permutations are obtained by taking into account different time ordering of the three different beams distinguished by frequency, wave vector and polarization. When the system is driven by a single beam, the third-order response involves only two terms: [7]

$$P = \varepsilon_0 \left\{ \chi^{(1)}(\omega) E + \frac{3}{8} \chi^{(3)}(\omega) E^2 E \right\}$$

The intensity of the laser is:

$$\mathrm{I} = \frac{1}{2} \varepsilon_0 c n_0 |\mathrm{E}|^2$$

and the polarization becomes:

$$\mathrm{P} = \varepsilon_0 \left(\chi^{(1)} + \frac{3}{4\varepsilon_0 c n_0} \chi^{(3)} \mathrm{I} \right) \mathrm{E}$$

$$= \varepsilon_0 \chi_{eff} \mathrm{E}$$

where χ_{eff} is an intensity-dependent effective susceptibility. The index of refraction then becomes:

$$n = \sqrt{\varepsilon} = \sqrt{1 + \chi_{eff}}$$

$$= \sqrt{1 + \chi^{(1)} + \frac{3}{4\varepsilon_0 c n_0} \chi^{(3)} I}\,.$$

Assuming the nonlinear term to be small compared to the linear one, the index of refraction becomes:

$$n = n_0 + n_2 \mathrm{I}.$$

The term n_2 is referred to as the nonlinear index of refraction and the phenomenon of a nonlinear component in the index of refraction is called the Kerr effect. From a classical viewpoint, the Kerr effect can be understood by using the harmonic/anharmonic oscillator picture. When the electric field of the light is low the dipole moment induced in the atom acts as a harmonic oscillator. The dipole moment per unit volume, which is the polarization of the medium, will oscillate at the same frequency as the driving field giving rise to the familiar expression of the refractive index $n = \sqrt{1 + \chi^{(1)}}$. When the electric field is sufficiently large the electron will see a modified potential and its motion is analog to that of an anharmonic oscillator. This will give rise not only to a polarization that oscillates at the same frequency with electric field of the light, but also to a nonlinear polarization that oscillates with a frequency that is the third harmonic of the original frequency of the light. This nonlinear polarization is term that gives rise to the intensity dependence of the refractive index. The nonlinear index of refraction has the following expression:

$$n_2 = \frac{3\chi^{(3)}}{4\varepsilon_0 c n_0^2}\,.$$

The nonlinear refractive index is almost always positive, but there are some media that exhibit a negative nonlinear refractive index.[72] Optical transitions that give rise to the third-order nonlinear susceptibility are associated with the bound electronic motion, molecular vibrations or molecular rotations of the system. The electronic transitions involve the largest energy separation while the rotational ones the smallest. This implies that the nonlinearities associated with the electronic transitions give the fastest response time. In large gap materials and for the cases where the energy of the laser photons is much smaller than the energy of the band gap, the response time can be very fast (<< 10 fs). For most applications the response time can be assumed instantaneous.[7] In a given material (solid, liquid, gas) one or more of these excitations may contribute to the optical Kerr effect.

The Kerr effect gives rise to self-focusing and self-phase modulation. These phenomena play an important role in the propagation of ultrashort laser pulses in transparent materials.

2.2.1 Self-focusing

Self-focusing (SF) arises from the intensity dependence of the refractive index and it essentially means that an ultrashort pulse creates a lens for itself as it propagates through a medium. To exemplify the point, assume that a Gaussian laser pulse propagates through such a nonlinear medium with positive n_2:

$$I(r,t) = I_0 \cdot e^{-4\ln 2\frac{r^2}{r_0^2}} \cdot e^{-4\ln 2\frac{t^2}{\tau^2}},$$

where I_0 is the peak intensity and r_0, τ are full width half maximum in the space and time domain, respectively.

According to the formula $n = n_0 + n_2 \cdot I$, the refractive index will also display a spatial variation, as seen in the Fig. 2.1.

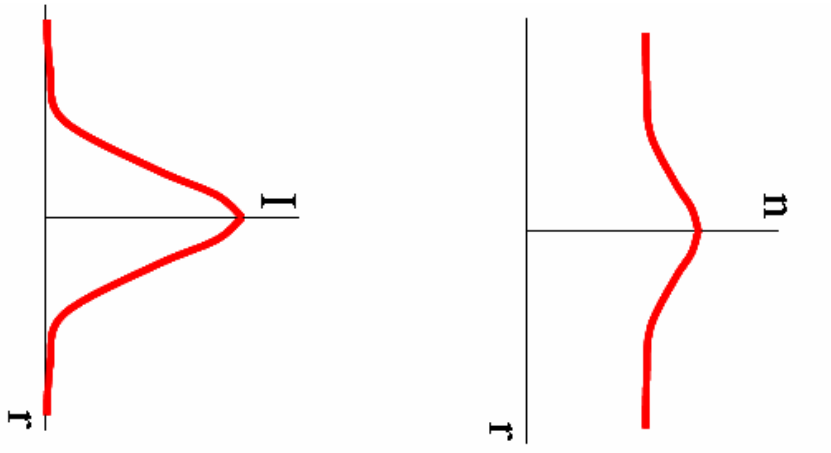

Figure 2.1 The refractive index displays a spatial variation. The peak of the pulse experiences a larger refractive index than the wings of the profile due to the higher intensity.

The peak of the beam experiences a larger refractive index than the wings of the profile due to the higher intensity. Therefore the central part travels at a slower phase velocity than the edges and the wavefront of the beam is distorted in a similar fashion to a focusing lens, as depicted in Fig. 2.2. The nonlinear refractive index depends on the intensity of the light, but not on its frequency. This means that the group velocity of the light, which depends on frequency derivative of the refractive index, is unaffected and

only the phase velocity of the light changes. The group velocity dispersion gives rise to the modification of the pulse shape. In the case of self-focusing, where only the phase velocity is modified, there will be no changes in the pulse shape.

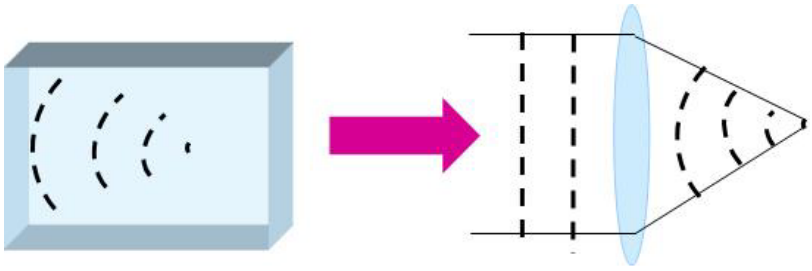

Figure 2.2 The wavefront of the beam is distorted in a similar fashion to a focusing lens and the beam creates a lens for itself as it propagates through the medium.

In the absence of any other processes the beam would catastrophically collapse. However there are competing linear and nonlinear processes that prevent this from happening. For example, any beam of finite width will suffer from diffraction, with the longer waves diffracting more than the shorter ones. The transverse amplitude distribution of optical beams from lasers has a Gaussian distribution, as do the propagation modes of some optical fibers and the cavity modes of Fabry-Perot resonators with spherical mirrors. In the Gaussian beam approximation the formula for the angular spread (see Fig. 2.3) due to diffraction is:[8]

$$\theta_{diff} = \frac{\lambda}{\pi w_0}$$

where λ is the wavelength of the light and w_0 is the minimum half-width of the Gaussian function describing the amplitude distribution of the electric field.

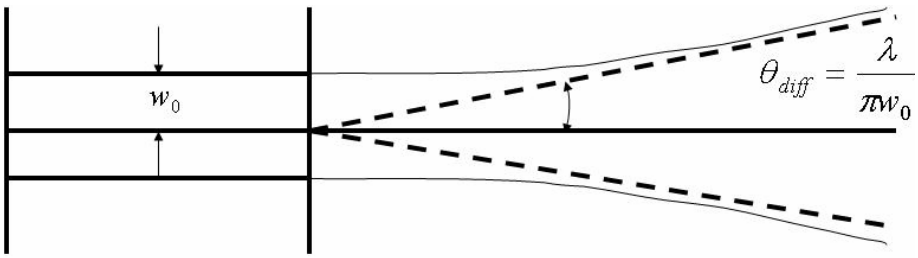

Figure 2.3 Any beam of finite width suffers from diffraction. The diffraction angle is wavelength dependent.

Depending on which process dominates (self-focusing or diffraction) a beam with finite diameter will either diverge, focus further or propagate with a constant diameter. It is important to note that the power, not the intensity, of the laser beam is crucial in determining if self-focusing will occur.[3] When the input power reaches a threshold value referred to as the critical power, the self-focusing balances diffraction and the beam propagates with a constant diameter (it forms a filament). However, this is generally true if the length of the medium is very long. In our experiment, where we use media with thicknesses of one to several millimeters and the beam needs to have a power which is several times larger than the critical power in order to self-focus. The filaments propagate over distances varying from hundreds of meters (in air)[9] to several millimeters (in solids).[10] This is the process of self-trapping.[3] An approximate formula for the critical

power can be derived following the arguments presented in Ref. 3 and Ref. 11. We assume a flat top intensity distribution. The refractive index inside the medium will therefore have a distribution as shown in Fig. 2.4:

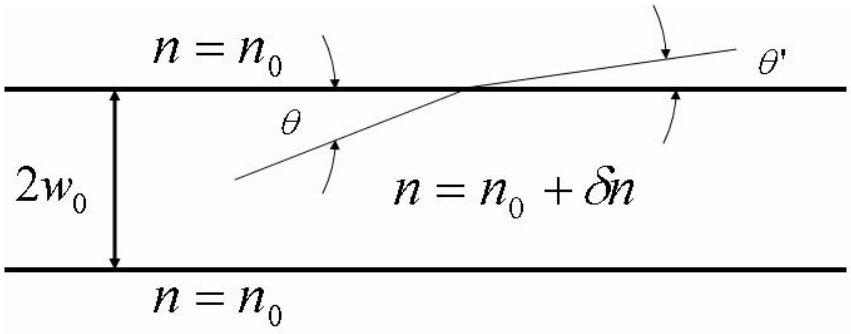

Figure 2.4 The distribution of the refractive index inside the nonlinear media due to a flat-top intensity distribution. A ray will remain trapped within the laser beam if it undergoes total internal reflection at the boundaries of the two regions.

The ray shown in the picture above will remain trapped within the laser beam if it undergoes total internal reflection at the boundary between the two regions. Total internal reflection occurs if θ is less than the critical angle θ_0 for total internal reflection, which is given by:

$$\cos\theta_0 = \frac{n_0}{n_0 + \delta n}.$$

Assuming that δn is much smaller than n_0 and therefore θ_0 is much smaller than unity, the above equation can be written as

$$1-\frac{1}{2}\theta_0^2 = 1-\frac{\delta n}{n_0}.$$

The critical angle is related to the nonlinear change in the refractive index by

$$\theta_0 = \sqrt{\frac{2\delta n}{n_0}}.$$

Setting equal the diffraction angle and the critical angle and solving for the critical power gives:

$$P_{crt} \approx 4\frac{\lambda_0^2}{8\pi n_0 n_2}.$$

A more advanced treatment[12] gives the factor of 3.77 instead of 4 in front of the above ratio.

For the case in which the input power is larger than the critical power a steady-state theoretical analysis predicts that the pulse will undergo catastrophic collapse.[13] In actuality this is prevented because the intensity of the self-focused light becomes so high that it starts ionizing the medium. The electron plasma contributes a negative refractive index change that acts like a divergent lens, as it will be explained in the next chapter of this thesis. The lens defocuses the beam, drops the intensity and thus prevents the collapse. Typical values for the nonlinear refractive index are of the order of $n_2 \sim 10^{-16}$ cm^2/W which lead to critical powers of the order of a few megawatts. Dispersion and other effects that change the pulse shape can also affect the self-focusing of the pulse. For example, it has been shown that small normal time dispersion delays the onset of self-focusing and causes the temporal splitting of the pulse into two peaks that continue to focus.[73]

2.2.2 Self-phase Modulation

Self-phase modulation (SPM) is due to the temporal dependence of the laser intensity, and hence the index of refraction, and results in the spectral broadening of the propagating beam. As in the case of SF, we assume that a Gaussian laser pulse propagates through a nonlinear medium with a nonlinear refractive index n_2. Since the laser intensity varies in time n_2 will also have a temporal dependence which produces a time-dependent phase shift of the pulse. In the slowly-varying envelope approximation, the electric field of the pulse has the form

$$E(z,t) = E_0(z,t)e^{i(kz-\omega t)} + c.c$$

where $E_0(z,t)$ is the slowly varying envelope of laser pulse. After propagating a distance L through a material, the pulse acquires a phase ϕ

$$\phi = kL - \omega t$$

$$= \frac{n(t)\omega}{c} L - \omega t$$

$$= \frac{\omega L}{c}(n_0 + n_2 I) - \omega t .$$

The "instantaneous frequency", given by the negative of the time derivative of the phase has the following form:

$$\omega(t) = -\frac{\partial \phi}{\partial t} = \omega - \frac{n_2 \omega L}{c}\frac{\partial I}{\partial t} .$$

In can clearly be seen from the above formula that new frequencies are generated and that the instantaneous frequency is red shifted on the leading edge of the pulse and is blue-shifted on the trailing edge (see Fig 2.5).

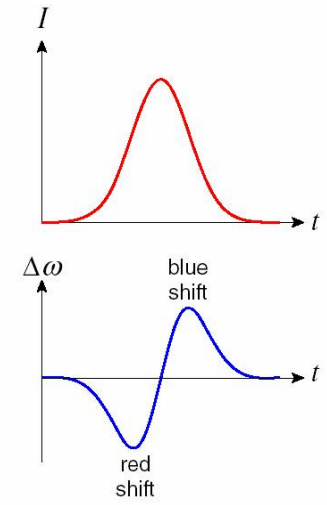

Figure 2.5 Self-phase modulation results in generation of new frequencies.

Qualitatively, we can understand SPM in terms of phase velocity. The refractive index is the largest at the peak of the pulse and thus the phase velocity will be slower in the middle of the pulse than at the front or back end. This results in a chirp across the pulse as seen in Fig. 2.6.

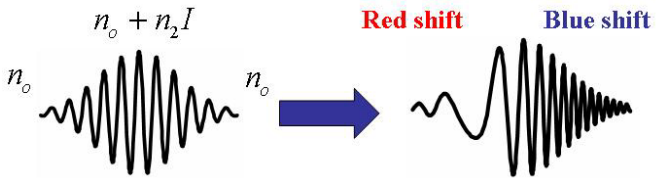

Figure 2.6 Self-phase modulation results in a linear chirp across the pulse.

2.3 Nonlinear Excitation

We have seen so far that if an ultrashort laser pulse, propagating through a transparent material, has sufficient power it self-phase modulates, self-focuses and forms a filament. As the pulse self-focuses the intensity of the light increases and it can reach a value such that significant ionization occurs. For a solid material this means that electrons are promoted from the valence band (VB) to the conduction band (CB). There are two important excitation mechanisms: photoionization (PI) and avalanche (collisional) ionization (AI).

2.3.1 Photoionization

Transparent materials have band gaps (E_g) of the order of a few electronvolts. For example, sapphire has a band gap of ~ 9.0 eV.[14] For fused silica and water the BG is ~ 7.5 eV[15] and for methanol the band gap is ~ 6.2 eV.[16] However these values should be regarded only as an approximate since they vary widely in the literature (± 2.5 eV). If

we compare the band gap of the transparent solids to the energy of a single photon 1.5 eV (at 800 nm), we see that multiple photons must be absorbed in order to excite an electron (see Fig. 2.7).

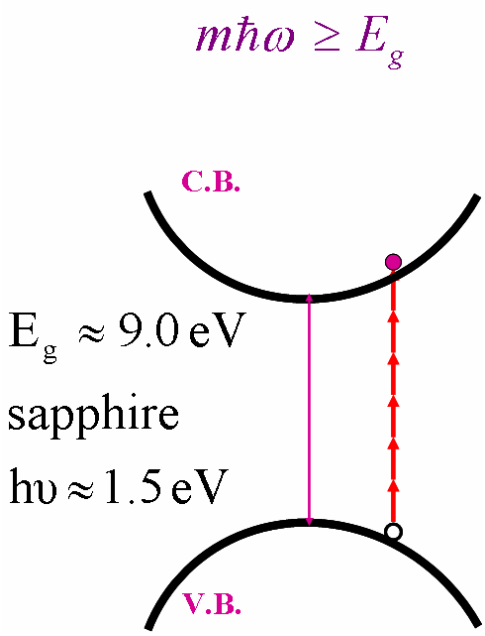

Figure 2.7 Multiphoton ionization.

Depending on the intensity and the frequency of the laser light, there are two regimes of the photoionization: multiphoton ionization (MPI) and tunneling ionization (TI). Keldysh showed for the first time that these two processes can be described in the framework of the same theory[17]. The photoionization rate per unit volume (in $m^{-3}s^{-1}$) was found to be:

$$w = \frac{2\omega}{9\pi}\left(\frac{\sqrt{1+\gamma^2}}{\gamma}\frac{m\omega}{\hbar}\right)^{3/2} Q\left(\gamma, \frac{\widetilde{\Delta}}{\hbar\omega}\right)\exp\left\{-\pi\left\langle\frac{\widetilde{\Delta}}{\hbar\omega}+1\right\rangle\times\frac{K\left(\frac{\gamma}{\sqrt{1+\gamma^2}}\right)-E\left(\frac{\gamma}{\sqrt{1+\gamma^2}}\right)}{E\left(\frac{1}{\sqrt{1+\gamma^2}}\right)}\right\}$$

where the quantities appearing in the above equation are explained in the Table 2.1.

F-the electric field Δ-the band gap
$\gamma = \frac{\omega\sqrt{m\Delta}}{eF}$-the Keldysh parameter
$\widetilde{\Delta} = \frac{2}{\pi}\Delta\frac{\sqrt{1+\gamma^2}}{\gamma}E\left(\frac{1}{\sqrt{1+\gamma^2}}\right)$-the effective ionization potential
$K(x) = \int_0^1 \frac{1}{(1-y^2)(1-x^2y^2)}dy$ - complete elliptical integral of the first kind $E(x) = \int_0^1 \frac{\sqrt{1-x^2y^2}}{\sqrt{1-y^2}}dy$ - complete elliptical integral of the first kind

Table 2.1Explanation of the Quantities Entering the Keldysh PI Formula.

Table 2.1 (continued)

$$Q(\gamma,x)=\left[\frac{\pi}{2K\left(\frac{1}{\sqrt{1+\gamma^2}}\right)}\right]^{1/2}\times\sum_{n=0}^{\infty}\exp\left\{-\pi\frac{\left[K\left(\frac{\gamma}{\sqrt{1+\gamma^2}}\right)-E\left(\frac{\gamma}{\sqrt{1+\gamma^2}}\right)\right]n}{E\left(\frac{1}{\sqrt{1+\gamma^2}}\right)}\right\}\times$$

$$\Phi\left\{\left[\frac{\pi^2\left(2\langle x+1\rangle-2x+n\right)}{2K\left(\frac{1}{\sqrt{1+\gamma^2}}\right)E\left(\frac{1}{\sqrt{1+\gamma^2}}\right)}\right]^{1/2}\right\}$$

$\Phi(z)=\int_0^z e^{y^2-z^2}\,dy$ - probability integral

TI and MPI have two very different physical pictures and different intensity dependences. The full Keldysh formula can be approximated to describe one process or another. The two regimes can be distinguished by looking at the Keldysh parameter, γ. If we replace the electric field with the corresponding intensity, γ has the form:

$$\gamma=\frac{\omega}{e}\left(\frac{mcn_0\varepsilon_0\Delta}{2I}\right)^{1/2}$$

where m is the reduced mass of the electron, c, ω, I are the velocity, the frequency and the intensity of light, n_0 is the refractive index of the material and ε_0 is the permittivity of the free space.

For very strong fields and low frequencies such that γ is much smaller than 1, the nonlinear photoionization is a tunneling process. This means that the electric field of the laser is strong enough to lower the energy barrier sufficient that the bound electron can tunnel through it during one optical cycle. For high frequencies (but not high enough to permit single photon transition) and lower intensities such that γ is much larger than 1, the nonlinear ionization is a multiphoton process. That means that an electron is promoted into the CB by simultaneously absorbing several photons. When γ is close to 1 one can think about the nonlinear photoionization as a mixture between TI and MPI. The MPI rate[18,19,20,21,22,23] is P(I) = $\sigma_k \mathrm{I}^k$, where k is the number of photons required to cross the band gap and σ_k is the multiphoton ionization cross-section . It can be seen that the MPI rate has very strong intensity dependence. The TI rate scales more weakly with the intensity than the MPI rate. The multiphoton ionization and the tunneling rates are obtained from the Keldysh formula using the approximations of the PI formula for $\gamma >> 1$ and $\gamma << 1$, respectively.[17]

$$w_{tunneling} = \frac{2}{9\pi^2}\frac{\Delta}{\hbar}\left(\frac{m\Delta}{\hbar^2}\right)^{3/2}\left(\frac{e\hbar F}{m^{1/2}\Delta^{3/2}}\right)^{5/2} \times \exp\left\{-\frac{\pi}{2}\frac{m^{1/2}\Delta^{3/2}}{e\hbar F}\left(1-\frac{1}{8}\frac{m\omega^2\Delta}{e^2F^2}\right)\right\}$$

$$w_{MPI} = \frac{9}{2\pi}\omega\left(\frac{m\omega}{\hbar}\right)^{3/2}\Phi\left[\left(2\left\langle\frac{\tilde{\Delta}}{\hbar\omega}+1\right\rangle-\frac{2\tilde{\Delta}}{\hbar\omega}\right)^{1/2}\right]\times$$

$$\times\exp\left\{2\left\langle\frac{\tilde{\Delta}}{\hbar\omega}+1\right\rangle\left(1-\frac{e^2F^2}{4m\omega^2\Delta}\right)\right\}\times\left(\frac{e^2F^2}{4m\omega^2\Delta}\right)^{\left\langle\frac{\tilde{\Delta}}{\hbar\omega}+1\right\rangle}$$

$$\tilde{\Delta} = \Delta + \frac{e^2F^2}{4m\omega^2\Delta}$$

Figure 2.8 shows the PI rate and the Keldysh parameter as a function of the laser intensity for λ = 800 nm and a band gap of 7.5 eV.

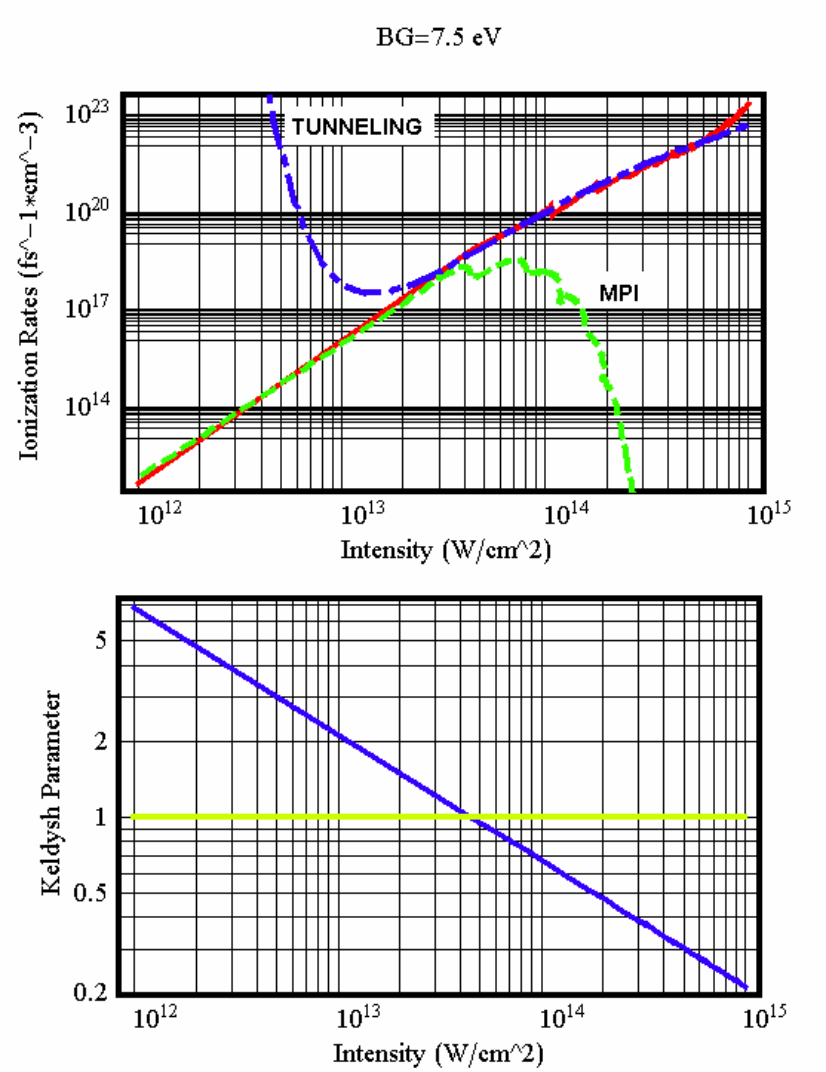

Figure 2.8 Photoionization rate as given by Keldysh formula (red), tunneling rate (blue), MPI rate (green) and the Keldysh parameter as a function of the laser intensity for light at 800 nm and a band gap of 7.5 eV.

It can be seen that MPI, TI and the full photoionization rate formulae agree with each other only for a Keldysh parameter close to 1. The tunneling ionization rate gives the same answer as the full formula only for γ down to 1 and then overestimates the rate. The multiphoton ionization rate agrees with the full Keldysh formula for γ up to 1 and then underestimates the rate. It is still not clear if this theory correctly describes the excitation process in solids for all wavelengths, band gaps and a large range of intensities. There are research groups that successfully match their data with this theory[20,21,23] but there are others that question its validity.[18,19] The work described here demonstrates conclusively that it does not.

2.3.2 Avalanche Ionization

If the intensity of a laser pulse propagating through a transparent material is high enough an electron can simultaneously absorb several photons and be promoted into the conduction band. The free electron in the CB can continue to absorb several photons and when the energy is equal or larger than the band gap of the material the electron can collisionally ionize another electron from the valence band. The result is two electrons in the CB, each of which can subsequently ionize more valence band electrons (see Fig. 2.9).

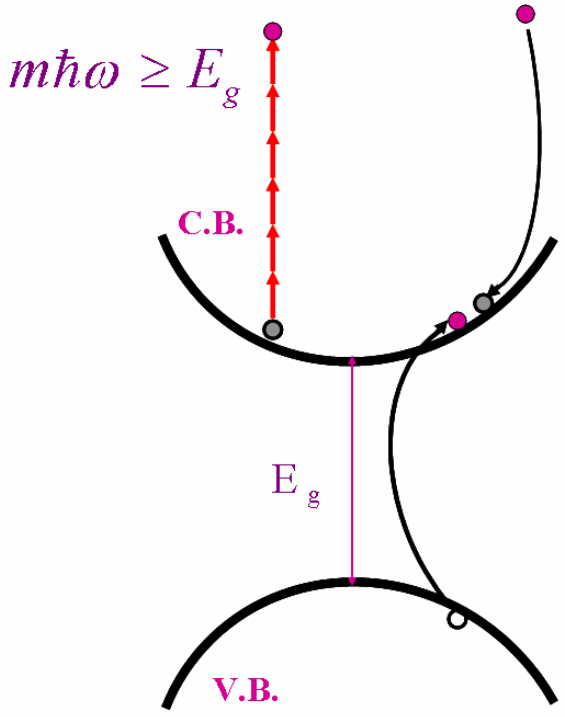

Figure 2.9 Avalanche Ionization.

AI has different intensity dependence than the MPI rate or the tunneling rate. A widely used formula for the AI rate[18,19,20,21,23] is $w_{avalanche} = \alpha$ I, where α is the avalanche ionization cross-section. This formula can be derived using a classical model.[74] The equation of motion of the electron, assuming that between collisions with the lattice ions the electron oscillates with the electric field, is:

$$\ddot{x} = -eE_0 \exp(-i\omega t).$$

The average oscillating energy is then

$$U_{osc} = \frac{e^2 E_0^2}{4m\omega^2}.$$

The electron's motion consists of translational and oscillating components. An elastic collision between the electron and a lattice ion leaves the initial kinetic energy unchanged (because of the large ration between the electron and lattice ion masses), but the translational motion changes. The electron has a completely new direction with respect to the field and the oscillating motion of the electron is built up anew. In conclusion, the electron acquires an average additional energy of the order of U_{osc}.

After the collision the momentum changes by $\Delta\vec{v}$ and thus the force acting during the collision is given by $\left\langle m \cdot \Delta\vec{v} / \tau \right\rangle$ (the angular brackets denote a temporal average). The equation of motion can be written in the form

$$m\dot{v} = -\frac{mv}{\left\langle \tau \right\rangle_\theta} - eE_0 \exp(-i\omega t),$$

where $\left\langle \tau \right\rangle_\theta$ is the average time between collisions, which takes into account the direction between the initial and the final velocities (θ). The solution for the above differential equation is

$$v = \frac{-eE_0}{m\left(\omega + \frac{i}{\left\langle \tau \right\rangle_\theta}\right)}.$$

The work done by the electric field per unit time is $-e\left\langle E \cdot v \right\rangle$. The rate of increase of the electron energy in the light field is

$$\frac{dU}{dt} = \frac{e^2 \left|\left\langle E \right\rangle\right|^2 \left\langle \tau \right\rangle_\theta}{m\left(1 + \omega^2 \left\langle \tau \right\rangle_\theta^2\right)}.$$

However a dependence of $w_{avalanche}$ to the square root of the intensity has been also predicted.[25] Utilizing changes in the carrier distribution function by magnitude and momentum scaling of scattering rates as well as taking into account phonon scattering and thermal effects, K. K. Thornber[25] derives the following avalanche ionization rate

$$w_{avalanche}(E) = \frac{E}{U_i}\exp\left(-\frac{E_i}{E(1+E/E_r)+E_{kT}}\right),$$

where U_i is the effective ionization energy, and E_{kT}, E_r and E_i are the threshold fields for carriers to overcome the decelerating effects of thermal (or quasielestic), optical-phonon, and ionization scattering, respectively.

2.4 Plasma Absorption and Defocusing

When a sinusoidally varying electric field is applied to a material the bound electrons from the valence band will oscillate at the same frequency as the driving field but the phase and the amplitude of the oscillation will be determined by the binding and the damping forces.[1] The oscillation is described by the following equation of motion:

$$m\frac{d^2x}{dt^2} + m\Gamma\frac{dx}{dt} = -eE_0e^{-i\omega t}.$$

In the above equation m is the mass of the electron and E_0, ω are the amplitude and the frequency of the applied field. The first term on the left hand side of the equation contains two terms: a term that describes the velocity-dependent damping force and the driving force applied to the electron. The solution of the inhomogeneous second-order differential equation has the form

$$x = x_0 e^{-i\omega t} = \frac{eE_0}{m(\omega^2 + i\Gamma\omega)} e^{-i\omega t}.$$

The oscillatory motion gives rise to a dipole moment $p(t) = -ex(t)$. For a sample with N free electrons the total polarization is:

$$P(t) = -Nex = -\frac{Ne^2 E_0}{m(\omega^2 + i\Gamma\omega)} e^{-i\omega t}$$

$$\equiv \varepsilon_0 \chi_e E(t)$$

The contribution of the electrons to the dielectric constant $\varepsilon = 1 + \chi_e$ has the form:

$$\varepsilon(\omega) = 1 - \frac{Ne^2}{m\varepsilon_0(\omega^2 + i\Gamma\omega)} = \varepsilon'(\omega) + i\varepsilon''(\omega).$$

If the damping is negligible $\Gamma << \omega$ the imaginary part of the free electron contribution vanishes and the real part becomes

$$\varepsilon'(\omega) = 1 - \frac{Ne^2}{m\varepsilon_0\omega^2} \equiv 1 - \frac{\omega_p^2}{\omega^2} \text{ with}$$

$$\omega_p = \frac{Ne^2}{m\varepsilon_0}$$

The quantity ω_p is referred to as the plasma frequency. The refractive index of the free electrons or plasma is n = $\sqrt{1 - \omega_p^2 / \omega^2}$. It can be seen that for frequencies larger than the plasma frequency the dielectric constant becomes negative and the refractive index is purely imaginary. Thus the electromagnetic wave does not penetrate the plasma and most of the light is reflected. When the light frequency is above the plasma frequency the electromagnetic waves propagate through the medium and for very high frequencies the

material becomes transparent. For intrinsic semiconductors, for example, the plasma frequency lies in the microwave or infrared part of the electromagnetic spectrum. [6]

The free electrons contribute negatively to the refractive index of the media. [26,27,28,29] Plasma action is equivalent to that of a negative lens and thus the laser beam is defocused as it will be explained in the Chapter 3 of this thesis. The effect of the plasma besides absorbing energy from the light is therefore to stop the self-focusing and prevent the catastrophic collapse of the beam.

2.5 Supercontinuum Generation and Other Nonlinear Effects

When an intense short pulse laser propagates through a transparent material it strongly perturbs or modifies the properties of the material. We have seen that a usually transparent material absorbs light with photon frequencies much smaller than the band gap and that the refractive index of the material becomes intensity dependent. The light changes the medium but the medium also changes the light. We have seen that a nearly monochromatic light pulse experiences a broadening of its spectrum as it propagates through the sample (SPM). Besides the self-focusing and SPM there are other nonlinear effects taking place: self-steepening, space-time focusing or stimulating Raman scattering (SRS). [30]

Self-steepening is a consequence of the intensity dependence of the refractive index. Whereas the intensity dependence of the phase velocity gives rise to SPM, the intensity dependence of the group velocity results in self-steepening. The peak of the pulse envelope has a smaller group velocity than the wings according to

$$v_g = \frac{c}{n + \omega \frac{dn}{d\omega}}.$$

Thus the peak of the envelope falls away from the leading edge and into the trailing edge, giving rise to a steep edge at the back of the pulse. Physically this can result in more blue-shifted than red-shifted frequencies being generated. This happens because the blue-shifted frequencies, as we have seen in the description of self-phase modulation, are generated in the trailing edge.

If the blue frequencies are generated more towards the back of the pulse, then the leading and the trailing edges of the pulse will diffract differently. This is basically the phenomenon of space-time focusing and results in an increase of the intensity at the back of the pulse which in turn gives rise to more blue-broadening.

Raman scattering is the result of the interaction of the light with the vibrational modes of the molecules in a sample and it can be regarded as light scattering from optical and acoustic phonons.[3] The scattered light contains frequencies different from the original light frequency. The components having frequencies lower than the driving one are referred to as Stokes components. Those with the frequencies larger than that of the excitation are named anti-Stokes components. The Stokes components are typically order of magnitudes more intense than the anti-Stokes ones.[3] One consequence of Raman scattering is obviously spectral broadening.

All the linear and nonlinear processes mentioned in this chapter compete and together give rise to one of the most interesting phenomenon in nonlinear optics, namely supercontinuum generation. SCG (see Fig. 2.10) is the dramatic spectral broadening (for

example, from 300 nm to 4500 nm[32] bandwidth) of a powerful laser pulse propagating through a nonlinear medium (solids, liquids, gases).

Figure 2.10 Pictures of white light viewed on a card. The pump laser wavelengths are, from left to right, 600 nm, 700 nm, 800 nm.

It was first observed by Alfano and Shapiro[31] in 1970 and since then it has been extensively studied. The spectral broadening ($\Delta\omega$) of the SCG follows a few rules of thumb:

- $\Delta\omega$ increases as the pulse width decreases;[3]
- $\Delta\omega$ increases as the frequency of the driving light decreases;[33]
- $\Delta\omega$ varies proportionally to the band gap of the material.[33]

2.6 Ultrashort Pulse Laser System

Ultrafast lasers, which generate pulses in the femtosecond range, have advanced greatly in recent years. Currently the shortest pulse duration is around 5 fs[34], average

powers reach 60 W[35] and pulse repetition rates can be as high as 100 GHz[36]. The technique that makes possible the generation of ultrashort pulses from lasers is referred to as modelocking.[37] There are two kinds of modelocking, active and passive, but the passive modelocking produces the shortest pulses.

In general, for a laser to produce short pulses, a couple of conditions must be fulfilled.[38] The laser must have a broadband gain medium and a large spectral emission since a large spectrum corresponds to a short pulse in the time domain. For Ti:sapphire lasers, which are the best for ultrashort pulse generation, the fluorescence has a bandwidth of almost 200. The large number of frequencies propagates with different group velocities in optics and therefore there must be a method to control the dispersion. Typically, a pair of prisms is used to compensate for the dispersion in the cavity[39] although chirped mirrors[40] (with better results) have also been used. We are talking here about pulsed lasers and therefore there must be an element that makes the laser run in the pulsed regime. The amplitude of the laser is modulated by using a saturable absorber[41] that introduces intensity-dependent losses for the intracavity laser radiation. The optical Kerr effect, described previously in this chapter, can play the role of a saturable absorber. The peak of the pulse, with the highest intensity, has a smaller loss (saturates the gain of the medium more strongly) than the low-intensity wings. This effect, in combination with a "hard" or "soft" aperture (the pump itself) gives rise to very short pulses.

Modelocked lasers output very short pulses, but they usually have low energies, of the order of nanojoules. In order to obtain considerable more energy, as is desired for many applications, the short pulses need to be amplified. This is not a simple task since as the energy of the pulse increases all the nonlinear processes described in this chapter

come into play resulting in distortion of the pulse. Another effect is that undesired damage to the optical components can happen due to the absorption of the light into them. A method has been designed to avoid these problems and it is referred to as chirp pulse amplification (CPA). [42]

Essentially the method consists in stretching out in time the short pulses coming out of the oscillator, amplify them and recompress them back to a short pulse. By amplifying a longer pulse, all the undesired effects mentioned above are avoided. The stretching/recompressing of the pulse is achieved by using a pair of antiparallel/parallel gratings that cause the redder frequency components to travel a larger/shorter pathlength. The amplification is obtained by switching selected pulses in and out of a second laser cavity (regenerative amplification).

The work in this thesis was done by using a CPA-based laser system that outputs pulses with duration of 60-70 fs (FWHM), energy of 1.2 mJ at a repetition rate of 1 kHz.

CHAPTER 3

DIRECT MEASURAMENT OF INTENSE FIELD IONIZATION RATES IN TRANSPARENT MATERIALS

3.1 Introduction

This chapter describes an experimental method based on plasma-induced blue-shifting that allows direct, time-resolved measurement of the electron excitation rate in transparent solids. The basic underlying idea has been used in gases [27,29] before but this is the first time to our knowledge when it has been employed in studying solids.

W. M. Wood and co-workers (Ref. 27) showed, for the first time that during the photoionization in high pressure gasses spectral blueshifting constitutes an alternative diagnostic to ion-yield and photoelectron spectroscopy. These techniques can no longer be used to monitor the atomic ionization dynamics since ionization via electron impact and collective effects begin to play a significant role. They showed that the blueshifting technique is suitable to femtosecond time-resolved pump-probe measurements and

provides information on the temporal dependence of the ionization rate within the ionizing pulse. The experiments were performed in atmospheric density nitrogen and most of the noble gases (He, Ne, Ar, Kr, Xe).

S. P. Le Blanc and R. Sauerbrey (Ref. 28) also studied the spectral, temporal and spatial characteristics of the plasma-induced spectral blue-shifting in atmospheric-density rare gases by a two-color, pump-probe technique. They showed that the blue-shifted spectra had an oscillatory-like structure, attributed to interference effects between frequency components occurring at different times in the laser pulse. Spectral shifts as large as 2 nm were observed.

For this work we used a pump-probe technique to measure the plasma-induced blue-shifting in four transparent solids (sapphire, fused silica, water, and methanol) with various band gaps and different nonlinear refractive indices. We observed considerably larger blueshifts (~ 75 nm, in sapphire) and directly determine the excitation rates and calculated the peak excitation densities in these solids. The importance of our study resides in the fact that despite a long history and numerous studies related to material processing,[18–21,23,43–45] laser propagation[13,22,46] and supercontinuum generation,[15,16,47] the excitation mechanisms in solids are yet to be well understood and even less quantified. Moreover, given the multitude of experimental techniques and the various experimental conditions employed, the results and the interpretations vary widely among different research groups as will be described in detail later. We will see that theoretical models[17,25] also yield results which range from several orders of magnitude difference to complete agreement.

3.2 Pump-probe Technique

The dynamics of ultrashort laser-excited plasmas cannot be studied using conventional time-resolved apparatus such as a streak camera or fast photodiode because of the short duration of the pulse. As a consequence, pump-probe optical techniques are used. These techniques have been widely employed in the study of solid state materials,[48] molecular reactions and dynamics,[48] plasma physics[49] and material damage studies.[50]

In general a powerful laser pulse, the pump, is used to perturb the sample. A second much weaker pulse, the probe, is used to measure the changes induced by the pump. The probe is variably delayed with respect to the pump and its transmission, reflectivity or phase shift is measured at these delays, resulting in a time-resolved measurement (Fig. 3.1). The time resolution is given by the probe pulse width in most cases.

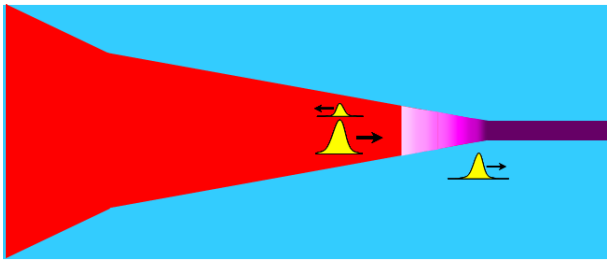

Figure 3.1 Pump-probe experiment. The pump creates an electron plasma that changes the refractive index of the media. The index of refraction leads to some reflection or scattering.

In our case a short, intense laser pulse excites electrons from the valence to the conduction band of a transparent material. This results in a change in the refractive index of the sample. From a strictly classical point of view the change in the index of refraction leads to some reflection or scattering. We collect the scattered light and measure the intensity [51] or spectrum.

3.3 Plasma-Induced Blue Shifting and Excitation Rates

When an intense short pulse propagates through a transparent material, it undergoes a wide range of competing linear and nonlinear processes, among them self-focusing and filamentation. If filamentation occurs, the intensity of the light is greatly increased and the ionization will occur. The conduction electrons generated in the process change the refractive index of the medium proportional to their time-varying density:

$$n(t) = \left(n_0 - \frac{N_e(t)}{N_{crt}} \right)^{1/2},$$

where N_e and $N_{crt} = \frac{\varepsilon_0 m_e \omega_0^{\,2}}{e^2}$ are the electron density and the critical density respectively, and n_0 and $n(t)$ are the refractive index of the unperturbed and perturbed medium. A second, much weaker pulse (the probe), copropagating through the material will encounter this time-varying refractive index of refraction, and therefore its phase will be modulated according to:

$$\varphi(t) = \frac{2\pi}{\lambda_0} n(t) L,$$

where λ_0 and L are the carrier wavelength of the probe and the interaction length respectively. The phase modulation gives rise to a spectral modification:

$$\Delta\omega(t) = -\frac{d\varphi}{dt} = \frac{\pi L}{\lambda_0 N_{crt}} \frac{dN_e}{dt}$$

where $\Delta\omega$ is the shift with respect to the original carrier frequency in the spectrum of the probe. The probe spectrum blue shifts ($\Delta\omega > 0$) when the electron density increases ($dN_e / dt > 0$). In fact, the blue shifting is a direct measure of the ionization rate, up to some constants. Note also that unless the probe pulse encounters a time-varying electronic density its spectrum will remain unshifted: $\Delta\omega = 0$.

3.4 Experimental Apparatus

Our experimental apparatus was straightforward and is shown in Fig. 3.2. The100 fs, nearly transform-limited light came from a Ti:sapphire based CPA laser system operating at a repetition rate of 1 kHz and wavelength of 800 nm. The light was sent into a Mach-Zender interferometer which split each pulse into two identical pulses. We discriminated between the two linearly polarized pulses by rotating the polarization of the probe by 90^0. The probe is attenuated and then delayed with respect to the pump by using a computer controlled delay line. The delay line consisted of two mirrors placed on a linear translation stage which was controlled by a Melles Griot Nanomotion II Micropositioner (nanomover). The nanomover had a travel line of 25 mm and a resolution of 10 nm. The probe and the pump were focused by a 100 mm lens into a 1 mm or 3 mm sapphire or fused silica substrate or into a 20 mm glass cell filled with water

or methanol. The sapphire substrate had a device grade polish and its c axis was perpendicular to its surface. The delay time is defined as being negative when the probe pulse precedes the pump. At positive delays the probe comes after the pump. The probe interacts with the plasma and is scattered, its amplitude being proportional to the size and the density of the sampled plasma. In our experiments we measure the spectrum of the scattered light, on each laser shot, with a Thermo Jarrel Ash MonoSpec 18 spectrometer. The spectrometer had a 50 μm input slit and a 156 mm focal length. The output slit was replaced with a CCD line camera from Unidata, Inc. The spectral bandwidth of the system was 90 nm with a resolution of 1 nm. The forward or backward scattered signal was sent into a Glan-Thompson polarizer to separate the probe pulse from the cross-polarized pump pulse. The main source of noise in the detection system came from the pump: depolarized pump light and white light leaked through the polarizer. However, the scattered light had slightly different angular distribution than the noise. Therefore it was possible to steer the beam in such a way that only the scattered light was correctly going into the detector and gave rise to a signal. An experimental run consisted in measuring the scattered light spectrum while changing the time delay between the two pulses.

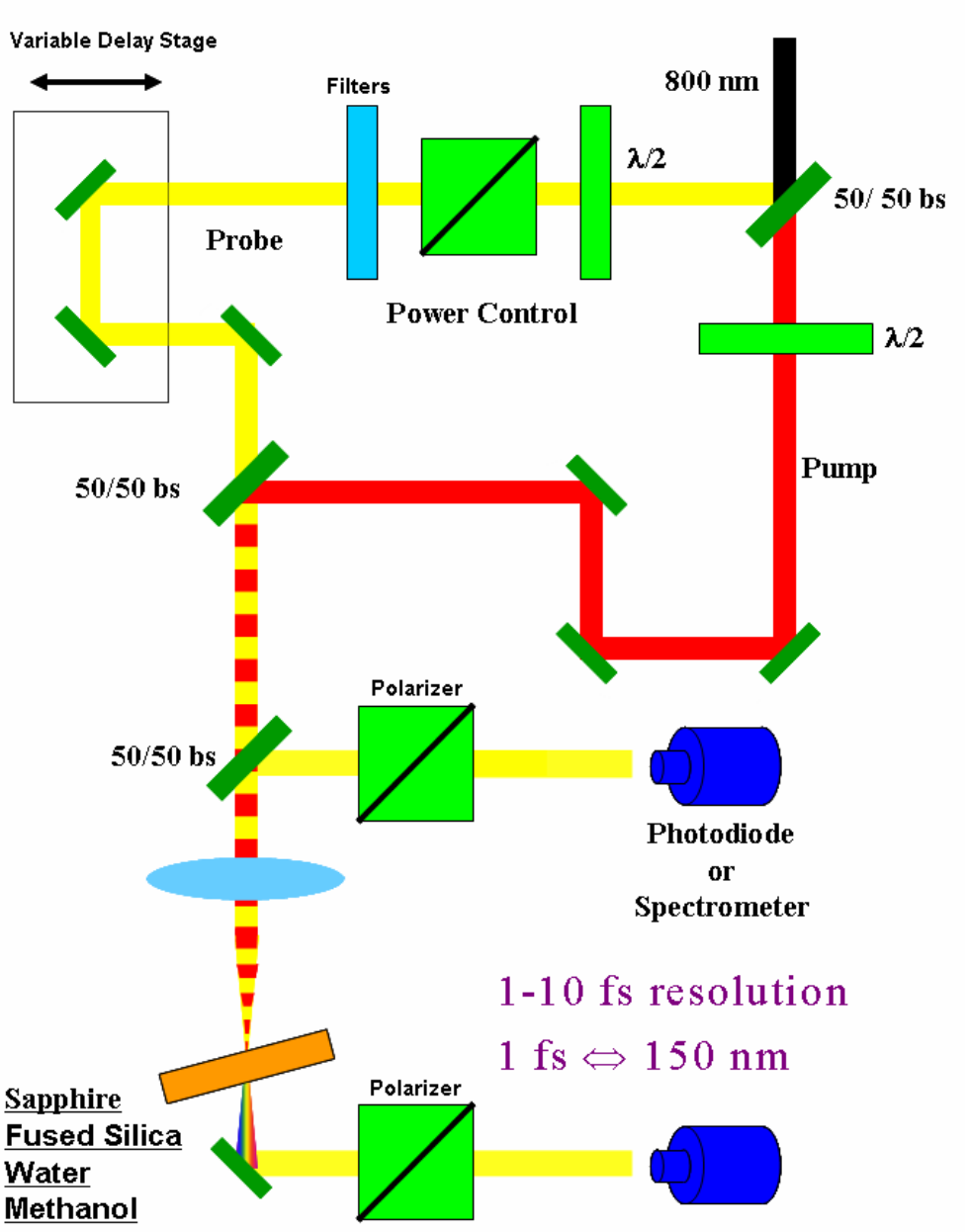

Figure 3.2 The experimental setup is straightforward. The light was sent into a Mach-Zender interferometer which split each pulse into two identical pulses. We discriminated between the two linearly polarized pulses by rotating the polarization of the probe by 90^0.

Experiments were performed in four dielectrics with different band gaps (see Table 3.1): sapphire (9.0 eV), water (7.5 eV), fused silica (7.5 eV) and methanol (6.5 eV). It is worth noting that the values for the band gaps vary widely in the literature. For water, for example, one can find band gap values from 6.5 eV [52] to 9.0eV [53]. For fused silica there were used values from 7.1 eV [55] to 9.0 eV. [18] Methanol and sapphire are less studied materials and there are only few references to their band gaps. For all materials we chose the values that have been most frequently used throughout the literature.

Material	Sapphire	Water	Fused Silica	Methanol
Band Gap (eV)	9.0	7.5	7.5	6.5
Refractive Index n_0	1.70	1.33	1.45	1.33
Nonlinear Refractive Index n_2 (cm^2/W)	$3 \cdot 10^{-16}$	$1 \cdot 10^{-14}$	$3 \cdot 10^{-16}$	$1 \cdot 10^{-16}$
Number of photons to cross band gap	6	5	5	4

Table 3.1 Linear and nonlinear refractive indices of the four dielectrics used in our experiments. The number of photons needed to cross the band gaps vary from 4 to 6.

3.5 Experimental Spectra in Sapphire, Water, Fused Silica and Methanol

Typical results, showing the spectrally integrated signal as a function of delay from 3 mm thick sapphire crystal are shown in Figure 3.3. The reflected probe is proportional to the plasma size and density in the medium. Negative delays times indicate that the probe pulse entered the sample before the pump pulse and therefore propagated unmodified. Positive delays indicate that the probe pulse entered the crystal after the pump pulse and encounter the electron plasma.

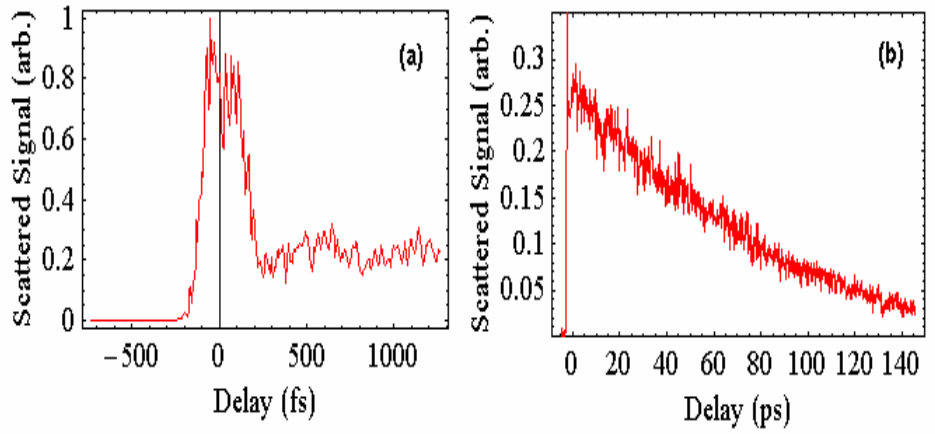

Figure 3.3 Scattered probe power as a function of delay between the pump and the probe pulses. (a) The small delay range measurement allows estimate of the plasma rising time (b) The larger delay range measurement shows the plasma lifetime.

The most noticeable feature in the above pictures is the spike at zero delay. This is not a plasma effect, but is due to four-wave mixing between the pump and probe and provides a convenient zero-delay marker. The four-wave mixing signal and the plasma reflected probe have different angular distributions so they can be separated if desired. Underneath the four wave mixing peak there is a true plasma signal with a rising time of the order of 300 fs. Figure 3.3 (b) shows the plasma decay, which is exponential. This picture shows that plasma is present out to delays as large as 150 ps. A more detailed analysis of these results will be presented in Chapter 6 of this thesis.

Sample results of spectrally resolved signal in sapphire are shown in Figures 3.4 (a) and (b).

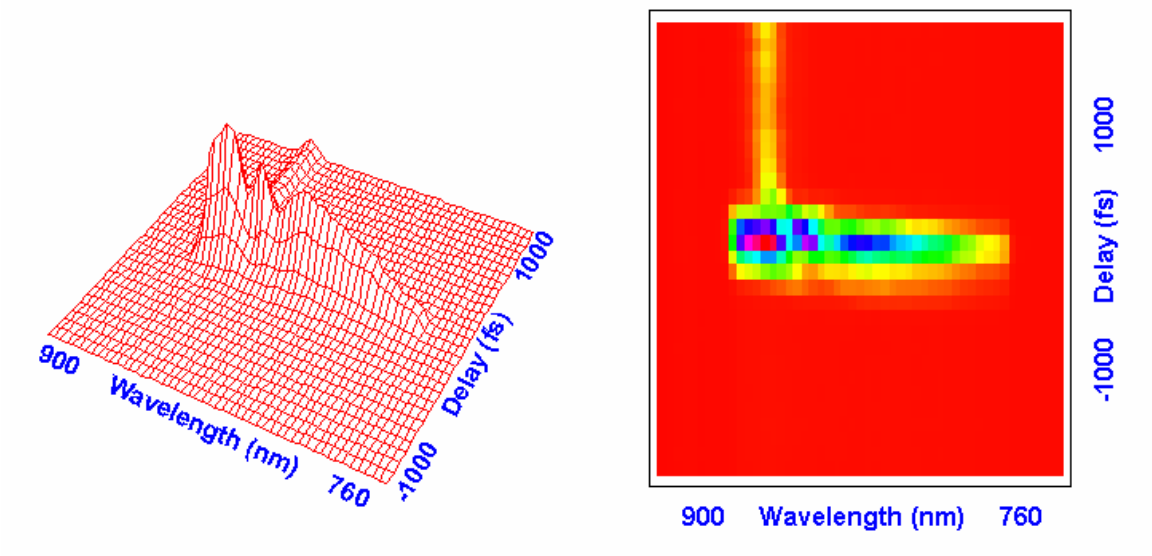

Figure 3.4 Sapphire-(a) Spectrum of the forward scattered probe. The data in this figure has been normalized to the maximum value of the signal in each run. In this run, the pump had an energy of 4.0 μJ. (b) Contour plot of the forward scattered probe due to IFE from the pump pulse for a 3 mm propagation length.

The data in these figures have been normalized to the maxim value of the signal in each run. In this runs, the pump had an energy of 4.0 μJ. This is the energy at which, under our experimental conditions, the white light was perfectly stable. When the probe enters the sample well before the pump, the plasma has not been created yet and therefore, there is no scattered probe, as it can be seen at negative delays. As the probe is brought closer to the pump and starts sampling plasma created on the pump's leading edge, we detect a signal with small amplitude, but with a clearly modified spectrum, shifted towards smaller wavelengths. As the probe and the pump overlap more in time, the amplitude of the scattered light increases reaches a maximum and then decreases, all in about 300 fs. At positive delays there is always a signal, but the spectrum is shifted back to 800 nm, since the probe does not encounters a time varying electron density, but rather a very slowly decaying plasma (~ 150 ps decay time)[51]. At positive delays, where the spectrum is shifted back to the original shape, the amplitude remains smaller, though, because of the absorption of the plasma generated by the pump pulse.

Typical results of spectrally resolved signal in water, fused silica and methanol are shown in Figures 3.5 (a) and (b), 3.6 (a) and (b), 3.7 (a) and (b).

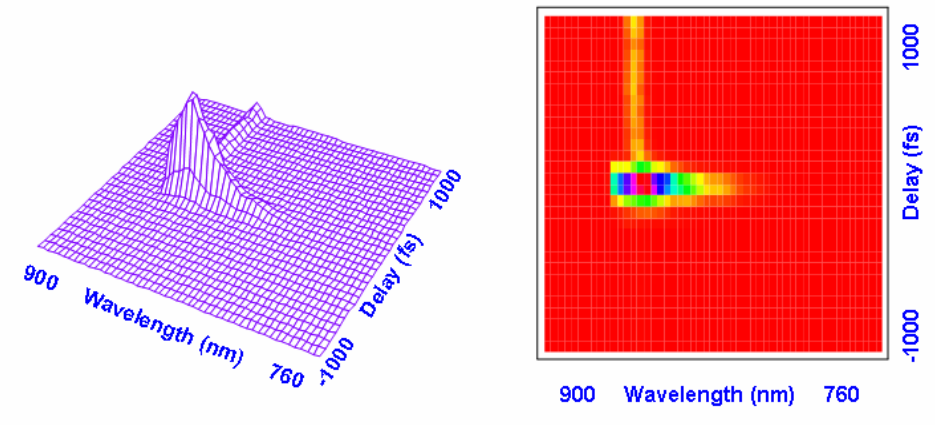

Figure 3.5 Water-(a) Spectrum of the forward scattered probe. The data in this figure has been normalized to the maximum value of the signal in each run. In this run, the pump had an energy of 2.5 μJ. (b) Contour plot of the forward scattered probe due to IFE from the pump pulse for a 20 mm propagation length.

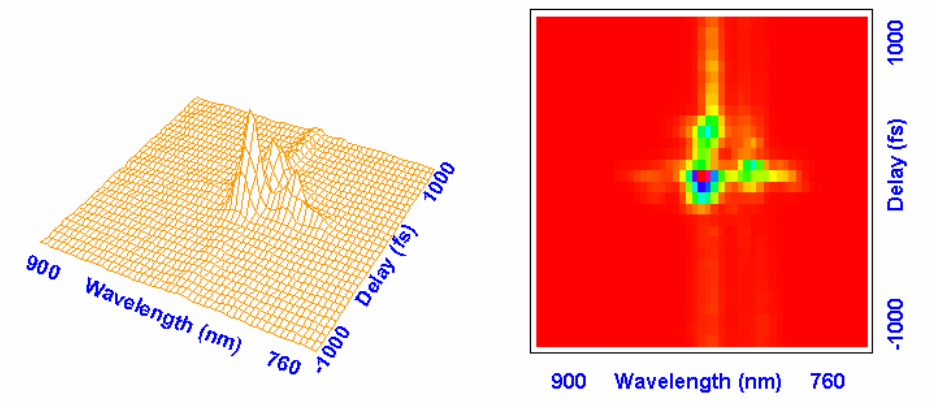

Figure 3.6 Fused Silica-(a) Spectrum of the forward scattered probe. The data in this figure has been normalized to the maximum value of the signal in each run. In this run, the pump had an energy of 4.5 μJ. (b) Contour plot of the forward scattered probe due to IFE from the pump pulse for a 3 mm propagation length.

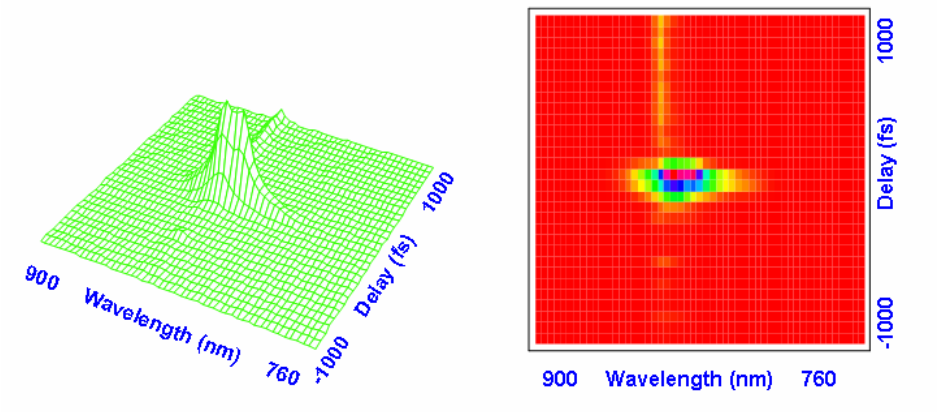

Figure 3.7 Methanol-(a) Spectrum of the forward scattered probe. The data in this figure has been normalized to the maximum value of the signal in each run. In this run, the pump had an energy of 2.5 μJ. (b) Contour plot of the forward scattered probe due to IFE from the pump pulse for a 20 mm propagation length.

The data in the above figures have been normalized to the maximum value of the signal in each run. In these runs, the pump had an energy of 4.5 μJ (fused silica) and 2.5 μJ (water and methanol). These pump energies gave rise, in each case, to a stable supercontinuum generation. In fact, for all of our runs the experimental conditions were such that the pump drove a stable supercontinuum generation (SCG). There was no apparent damage to the sapphire or fused silica samples.

It is well known[58] that when the laser power is much higher than the critical power for self-focusing, multiple filaments will be generated. The process of multifilamentation is due to the intensity perturbations across the wavefront, such as the imperfections in the initial beam. Also refractive index fluctuations are sources of perturbation and will easily induce the formation of multiple filaments. It has been

observed[58] that, during propagation, filaments can dynamically interfere with each other. There are also studies that advocate for the deterministic nature[78] of femtosecond multiple filamentation. It is shown[78] that this process can be controlled in several ways, even if noise in the input beam modifies the initial growth of the filaments. The multifilamentation patterns are organized by acting on the distribution of either the intensity or the phase of the input beam. The number, the position, and the subsequent evolution of femtosecond multiple filaments can be controlled by reshaping the initial beam profile.

A couple of spectra at selected time delays between the probe and the pump are shown below (Fig. 3.8, Fig. 3.9, Fig. 3.10 and Fig. 3.11). The data in these figures have been scaled to have a maxim value of one.

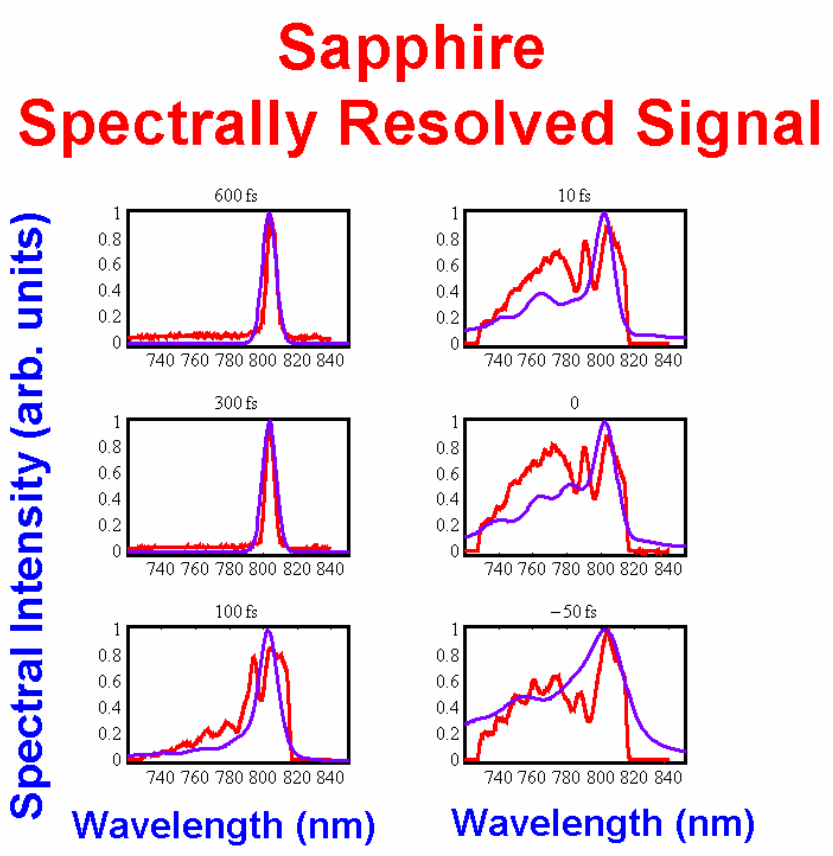

Figure 3.8 Sapphire-Spectra at selected time delays between the probe and the pump. The purple colored traces are the results from a 1-D calculation.

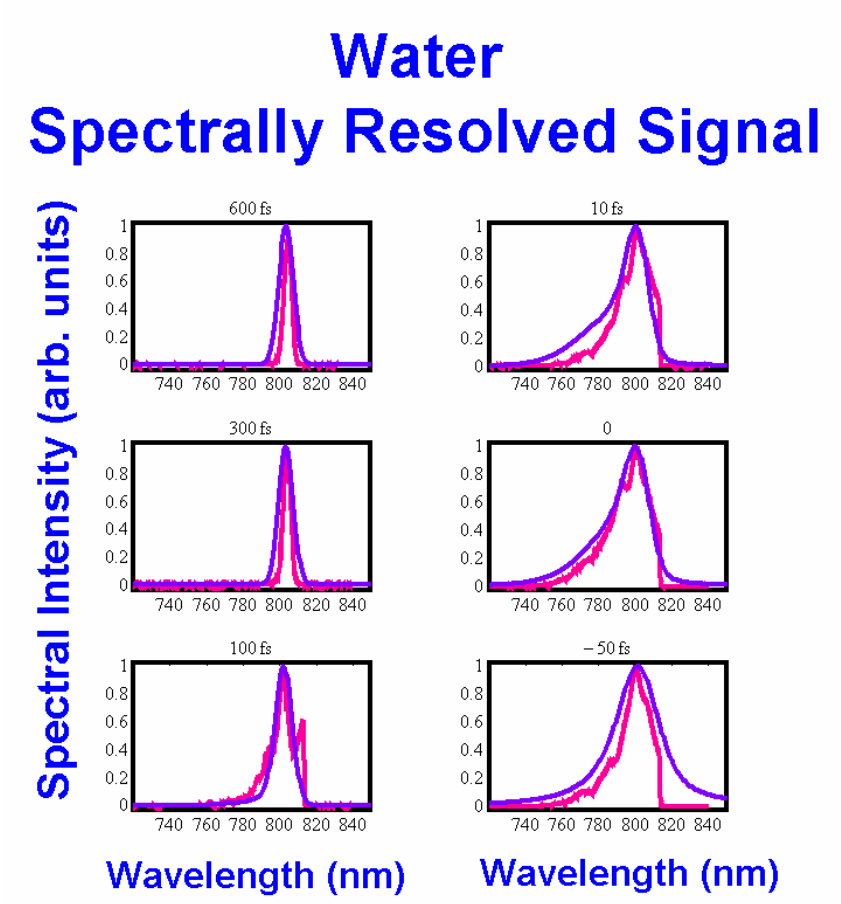

Figure 3.9 Water-Spectra at selected time delays between the probe and the pump. The purple colored traces are the results from a 1-D calculation.

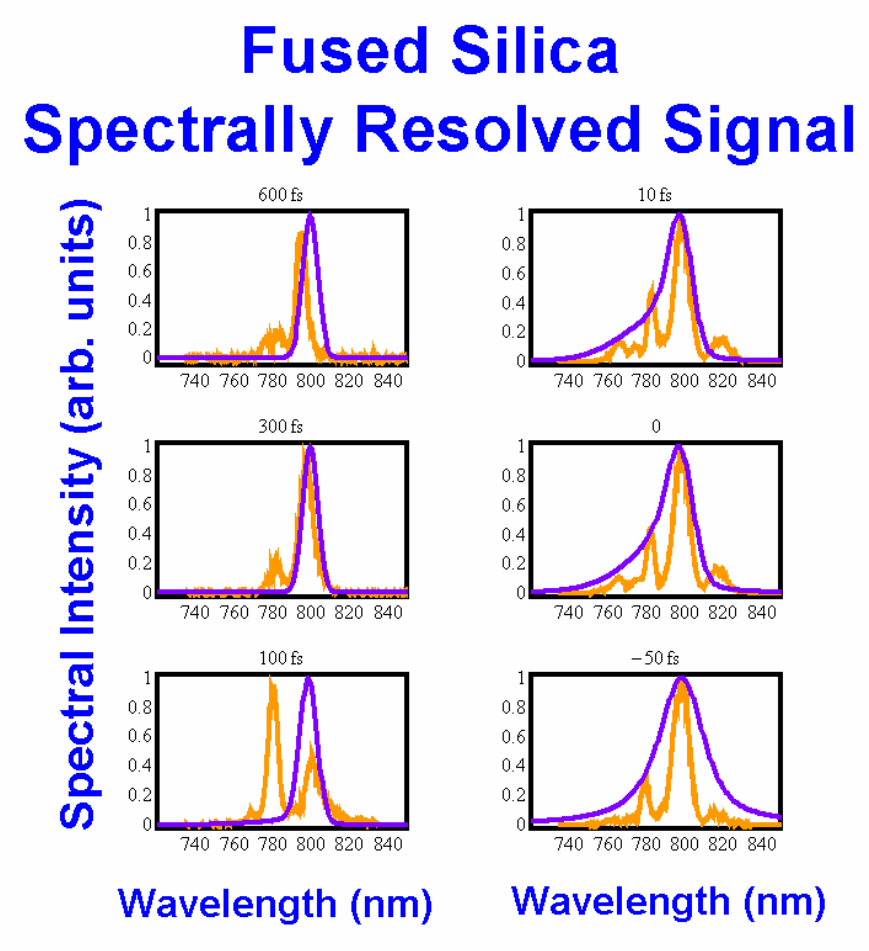

Figure 3.10 Fused Silica-Spectra at selected time delays between the probe and the pump. The purple colored traces are the results from a 1-D calculation.

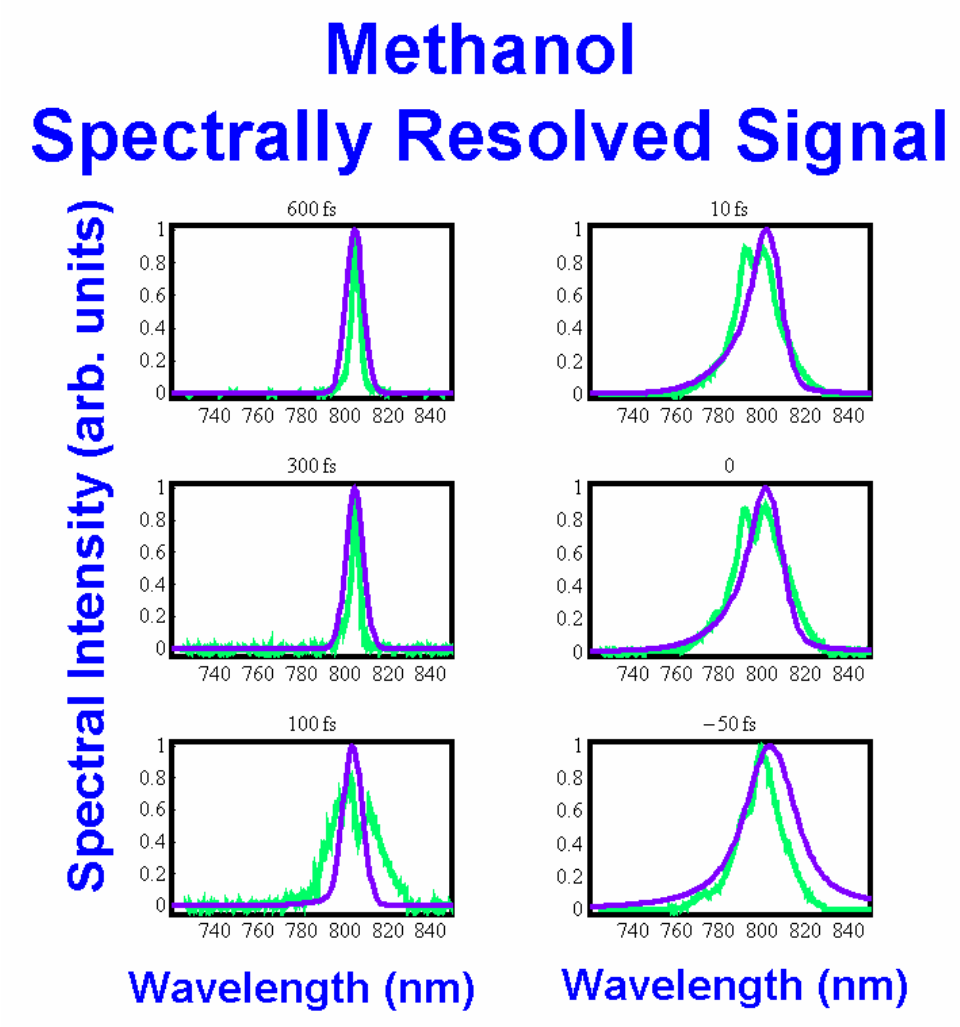

Figure 3.11 Methanol-Spectra at selected time delays between the probe and the pump. The purple colored traces are the results from a 1-D calculation.

Along with the experimental data we also present the results from a 1-D calculation. The simulation will be discussed at the end of this chapter.

3.6 Experimental Blue Shifts

The blue shifted spectra are basically determined by the strength of self-focusing in each material, the effect of the plasma defocusing and the band gap of the material. In our experiment we show that the time-delayed probe spectra provide a quantitative measure of the amount of plasma blue shifting and it is directly related to the electronic excitation rate.

We obtain the "peak blue shift" for each material by looking at the difference between the shortest wavelength and the probe carrier wavelength. The shortest wavelength is defined as being the wavelength of the scattered radiation whose spectral intensity is just above the background. The threshold differs from material to material and from run to run but it is always around 7% to 9% from the absolute maximum spectral intensity in each run. The peak value of the blueshifts thus obtained varies as a function of the threshold, but not significantly. Consider, for example, figure 3.12 that shows the time-varying blue shifting in sapphire for different thresholds.

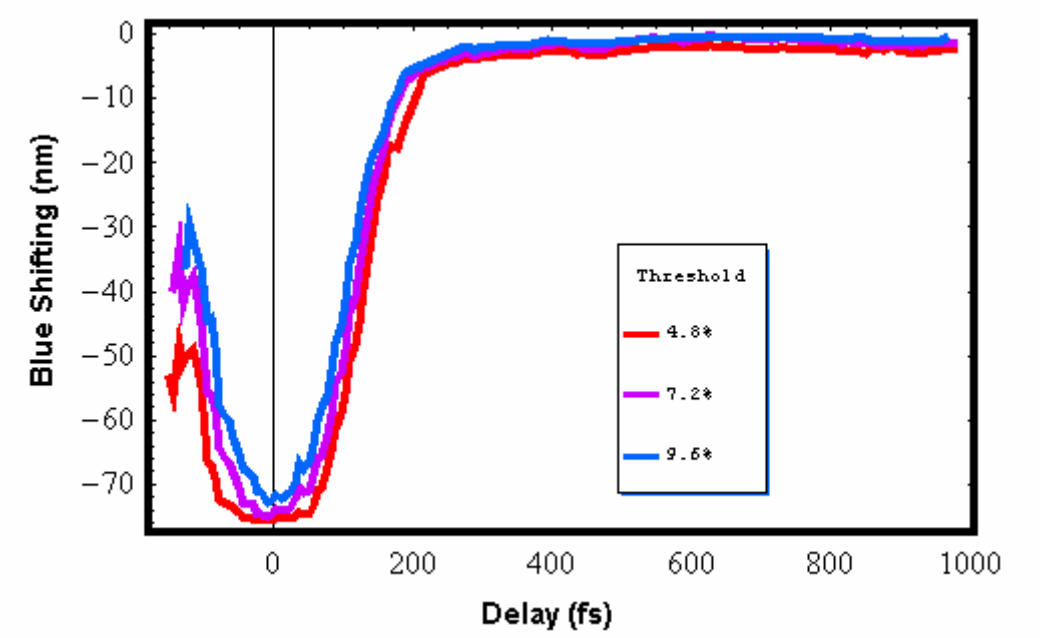

Figure 3.12 Time-varying blue shifting in sapphire for different thresholds. A typical threshold variation of about 4.8% results in a 3.7 nm difference in the peak blue shifting.

A typical threshold variation of about 4.8% results in a 3.7 nm difference in the peak blue shifting, which is about 4.8%. Sample results are shown in figure 3.13.

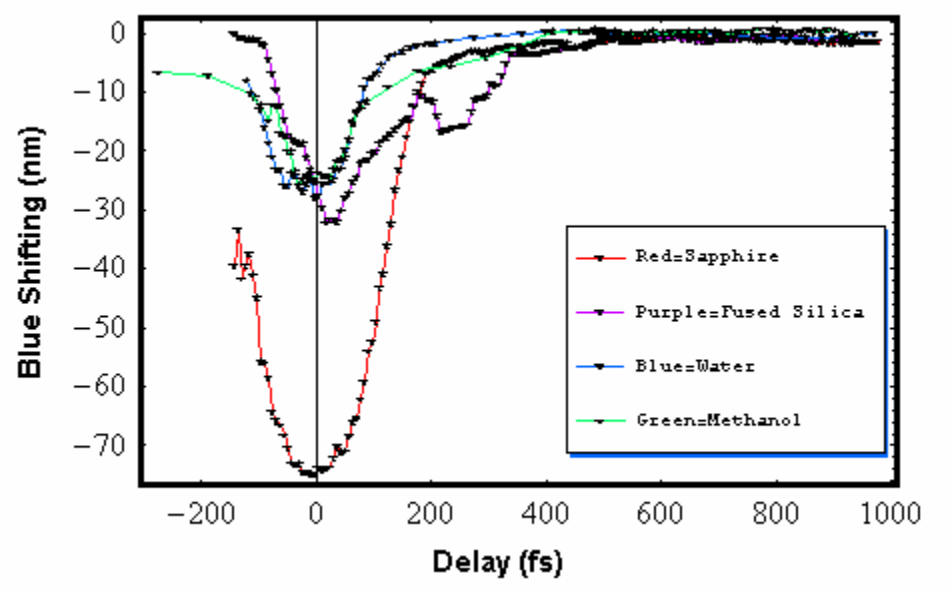

Figure 3.13 The largest blue-shifts ($\Delta\lambda \approx 75$ nm) were obtained in sapphire, while in water ($\Delta\lambda \approx 28$ nm), fused silica ($\Delta\lambda \approx 32$ nm) and methanol ($\Delta\lambda \approx 26$ nm) the shifts were more modest ($\Delta\lambda \approx 20$ nm).

The maximum blue-shifts were obtained in sapphire ($\Delta\lambda_{max} \sim 75$ nm), while in water ($\Delta\lambda_{max} \sim 28$ nm), fused silica ($\Delta\lambda_{max} \sim 32$ nm) and methanol ($\Delta\lambda_{max} \sim 26$ nm) the shifts were more modest. A possible explanation could be that ionization occurs less readily in sapphire.

Self-focusing in water (the nonlinear refractive index $n_2 \sim 10^{-14}$ cm^2/W)[55] is larger than that in sapphire ($n_2 \sim 3 \cdot 10^{-16}$ cm^2/W).[56] As a consequence, the intensities achieved in water could be larger and that translates into a larger number of electrons. Also it is easier to create electrons in water than in sapphire, since the band gap of the former is lower by about 1.5 eV. A large amount of plasma could easily cause the pump to defocus, drop the intensity, lower the ionization rate and therefore cause smaller blue

shifts. Fused silica ($n_2 \sim 2.5 \cdot 10^{-16}$ cm^2/W)[57] and methanol ($n_2 \sim 10^{-16}$ cm^2/W)[58] are nonlinear indices comparable to the nonlinear index of sapphire. However it is still easier to ionize fused silica and methanol than it is to ionize sapphire. In this case although the strength of the self-focusing is the same, a larger amount of plasma is created in the materials with smaller band gaps and the above arguments still holds.[33] This has been observed in the literature. We checked this hypothesis by making the following analysis.

We have seen that when a short pulse propagates through a medium, the refractive index of the medium can change according to the formula $n(t) = n_0 + n_2 I$ and the pulse creates a convergent lens for itself (Kerr effect). The free electrons generated by the intense field excitation also create a lens, but in this case a divergent one. We calculated the strengths of the convergent and the divergent lens, respectively, seen by the light and due to the Kerr and plasma effect by following Yariv's[5] treatment for lenslike media. According to Yariv, the complex field amplitude of the incident optical field $E_R(x, y)$ immediately to the right of an ideal thin lens can be related to the complex field amplitude $E_L(x, y)$ immediately to the left by

$$E_R(x, y) = E_L(x, y) \exp\left(+ ik \frac{x^2 + y^2}{2f} \right)$$

where f is the focal length and $k = 2 \cdot \pi \cdot n / \lambda$ (λ is the vacuum wavelength). The effect of the thin lens is to introduce a phase shift $k(x^2 + y^2)/2f$ that increases quadratically with the distance from the axis. A similar phase shift is introduced by a medium whose index of refraction varies according to

$$n(x,y) = n_0\left[1 - \frac{k_2}{k_1}\left(x^2 + y^2\right)\right]$$

where k_2 is a constant. If $k_2 > 0$ ($k_2 < 0$) the medium behaves like a convergent (divergent) lens. The behavior of a paraxial ray propagating through an optically inhomogeneous medium is described by the following differential equation

$$\frac{d^2 r}{dz^2} + \left(\frac{k_2}{k_1}\right) r = 0 .$$

This equation has a solution $r(z) = C_1 \cdot e^{i\sqrt{\frac{k_2}{k_1}}z} + C_2 \cdot e^{-i\sqrt{\frac{k_2}{k_1}}z}$. Assuming that at the input plane z = 0 the ray has a radius r_0 and slope r_0', we can calculate the constants C_1, C_2. At any plane z the radius and the slope of the ray are given by

$$r(z) = r_0 \cos\left(z\sqrt{\frac{k_2}{k_1}}\right) + r_0'\sqrt{\frac{k_1}{k_2}} \sin\left(z\sqrt{\frac{k_2}{k_1}}\right)$$

$$r'(z) = -r_0\sqrt{\frac{k_2}{k_1}} \sin\left(z\sqrt{\frac{k_2}{k_1}}\right) + r_0' \cos\left(z\sqrt{\frac{k_2}{k_1}}\right)$$

If we rewrite these results using a matrix formalism the result is

$$\begin{pmatrix} r(z) \\ r'(z) \end{pmatrix} = \begin{pmatrix} \cos\left(z\sqrt{\frac{k_2}{k_1}}\right) & \sin\left(z\sqrt{\frac{k_2}{k_1}}\right) \\ -\sqrt{\frac{k_2}{k_1}} \sin\left(z\sqrt{\frac{k_2}{k_1}}\right) & \cos\left(z\sqrt{\frac{k_2}{k_1}}\right) \end{pmatrix} \cdot \begin{pmatrix} r(0) \\ r'(0) \end{pmatrix}.$$

If we further assume that $r_0' = 0$ and $r_0' = n_0 \cdot r'(0)$, then the above matrix becomes

$$M = \sqrt{\frac{k_1}{k_2}} \cos\left(z\sqrt{\frac{k_2}{k_1}}\right) \cdot \begin{pmatrix} 1 & 0 \\ -n_0 \cdot \sqrt{k_2/k_1} \cdot \tan\left(z\sqrt{k_2/k_1}\right) & 0 \end{pmatrix}.$$

We compare the above matrix to the one describing a thin lens with the focal length f

$$M' = \begin{pmatrix} 1 & 0 \\ -1/f & 1 \end{pmatrix}.$$

Finally, we can conclude that a thin medium with a quadratically varying index of refraction and a length l is equivalent with a lens with the focal length

$$f^{convergent} = \frac{1}{n}\sqrt{\frac{k_1}{k_2}}\cot\left(l\sqrt{\frac{k_2}{k_1}}\right)$$

$$f^{divergent} = -\frac{1}{n}\sqrt{\frac{k_1}{k_2}}\coth\left(l\sqrt{\frac{k_2}{k_1}}\right)$$

where $f^{convergent}$ / $f^{divergent}$ is obtained when $k_2 > 0 / k_2 < 0$.

Next we are going to relate these calculated focal lengths to the Kerr effect and plasma formation. First let's look at the plasma effect. Assuming that the electrons are created by multiphoton excitation, it is reasonable to assume that the electron density has a spatial distribution as it is shown below

$$N_e(r) = N_e(0)\cdot e^{-k\frac{r^2}{R^2}}$$

$$\approx N_e(0)\left(1-\frac{kr^2}{R^2}\right)$$

where $N_e(r)$ is the electron density at distance r from the axis, $N_e(0)$ is the peak electron density (on-axis), k is the number of electron to cross the band gap and R is the radius of the filament. Combining the above formula with $n(t) = \left(n_0 - N_e(t)/N_{crt}\right)^{1/2}$, we can identify $\sqrt{k_1/k_2}$

$$\frac{k_2}{2k_1} = \frac{N_e(0)k}{2N_{crt}R^2}\frac{1}{n_0 - \dfrac{N_e(0)}{2N_{crt}}}.$$

Similarly, for the Kerr effect, we can write

$$n = \left(n_0 + n_2 I(0)\right)\cdot\left(1 - \frac{n_2 I(0)}{R^2}\frac{1}{n_0 + n_2 I(0)}r^2\right)$$

and identify $\sqrt{k_1 / k_2}$

$$\frac{k_2}{2k_1} = \frac{n_2 I(0)}{R^2}\frac{1}{n_0 + n_2 I(0)}$$

Finally, we make use of the fact that the peak densities $N_e(0)$ (we obtained the peak densities from the experimentally measured ionization rates, as it will be seen in the next subchapters) are about one tenth from the critical densities. The results are summarized in Table 3.2.

Material	$f^{divergent(plasma)}(\mu m)$	$f^{convergent(Kerr)}(\mu m)$
Sapphire	-56	15000
Water	-68	13000
Fused Silica	-65	720
Methanol	-90	760

Table 3.2 Focal lengths of the lenses due to the Kerr and plasma effects.

There are a couple of observations to be made about these values. First, the plasma effect is a very strong one and it must have a significant effect on defocusing the pump. Second, the Kerr effect in sapphire is much weaker than the one in water and methanol and therefore the light creates fewer electrons that would subsequently defocus the beam and drop the ionization rate. However, the Kerr effect is comparable to the one in fused silica, but we do not see the same dramatic blueshifting as we see in sapphire. A possible explanation could be that although the Kerr effect is comparable, the difference in band gaps makes it favorable to create more electrons in fused silica; hence the defocusing is more important.

3.7 Multiphoton Ionization Rates

In order to understand how our work fits into the larger picture of the ultrashort laser-plasma interaction, it is useful to make a review of what it has been done so far and of what we have learned about this type of interaction.

D. Du *et al*[59] studied breakdown in fused silica, for pulses with time durations between 150 fs and 7ns. They concluded that the contributing ionization mechanisms are the tunneling ionization and the avalanche ionization. The latter was found to dominate over the entire pulse-width range and the impact ionization rate was estimated by using Thornber's formula.

B. C. Stuart and coworkers[44] reported measurements of damage thresholds for fused silica and calcium fluoride. They used light at 1053 nm and 526 nm and pulse widths ranging from 270 fs and 1 ns. These researchers found that the multiphoton

ionization produced most of the electrons with only a small collisional avalanche required to achieve critical density. They developed a theoretical model where the avalanche ionization varied proportional with the intensity of the light and the MPI rate was given by the Keldysh theory. For pulse widths smaller then 30 fs they concluded that MPI alone is sufficient to damage the medium.

M. Lenzner *et al*[18] reported optical breakdown measurements on several dielectrics with different band gaps and pulses durations ranging between 5 fs and 5 ps. Their investigations confirm a linear scaling of the avalanche ionization with intensity and yield MPI rates that are order of magnitudes lower than those predicted by Keldysh theory. Their conclusions were that the optical breakdown in fused silica was dominated by the AI down to the 10 fs regime and that for smaller band gaps materials (like BBS) MPI took over for pulse durations smaller than 100 fs.

An-Chun Tien[45] *et al*, by performing damage threshold measurements for fused silica, questioned the applicability of an AI rate linearly scaled with laser intensity. Also, they found that Thornber's expression for AI along with the Keldysh's PI theory in solids describe the physical processes in dielectrics better than the linear scaling and the MPI approximation. They found that the AI predominates even in the case of sub-100 fs pulses.

M. Li and coworkers[19] measured optical breakdown threshold in dielectrics with different band gaps for 25 fs pulses. These researchers fitted their data with a model that assumed an AI rate that was linearly dependent on intensity and a MPI rate described by the multiphoton approximation. The absorption cross-sections for MPI did not match those given by Keldysh theory.

S. Tzortzakis *et al*[20] studied self-guided propagation of ultrashort IR laser pulses in fused silica. The electrons are created by MPI and AI (linear intensity dependence) with the absorption cross-section for the MPI given by Keldysh theory.

L. Sudrie and coworkers[21] investigated bulk damage induced by femtosecond IR pulses in silica. They matched their data by using the full Keldysh PI formula along with the avalanche ionization (linear intensity dependence). The same conclusion was reached by A. Couairon *et al*. [23]

We would like to point out that all the above experiments were studying damage and that the information about ionization processes was indirectly extracted. First, there had to be defined a "threshold" that varied from experiment to experiment. Second, once the damage threshold was calculated, various theories were employed to fit the data. The fitting parameters were the absorption cross-sections. Our method is much more direct and we hope that eliminates the uncertainties inherent in the indirect methods described above.

Regarding our data, once we obtain the blueshifting we can calculate the time-varying multiphoton excitation rates. We simply multiply the blueshifting value, at each delay, with the quantity ($-2cN_{crt}/L\lambda_0$). Our results are shown in figure 3.14 and figure 3.15. For all materials we chose a propagation length of $50\,\mu$m. The reason is the following: we do not know the length of the filament inside the media; however we know that the minimum propagation distance necessary to form a filament is $50\,\mu$m (as it will be discussed Chapter 5 of this thesis).

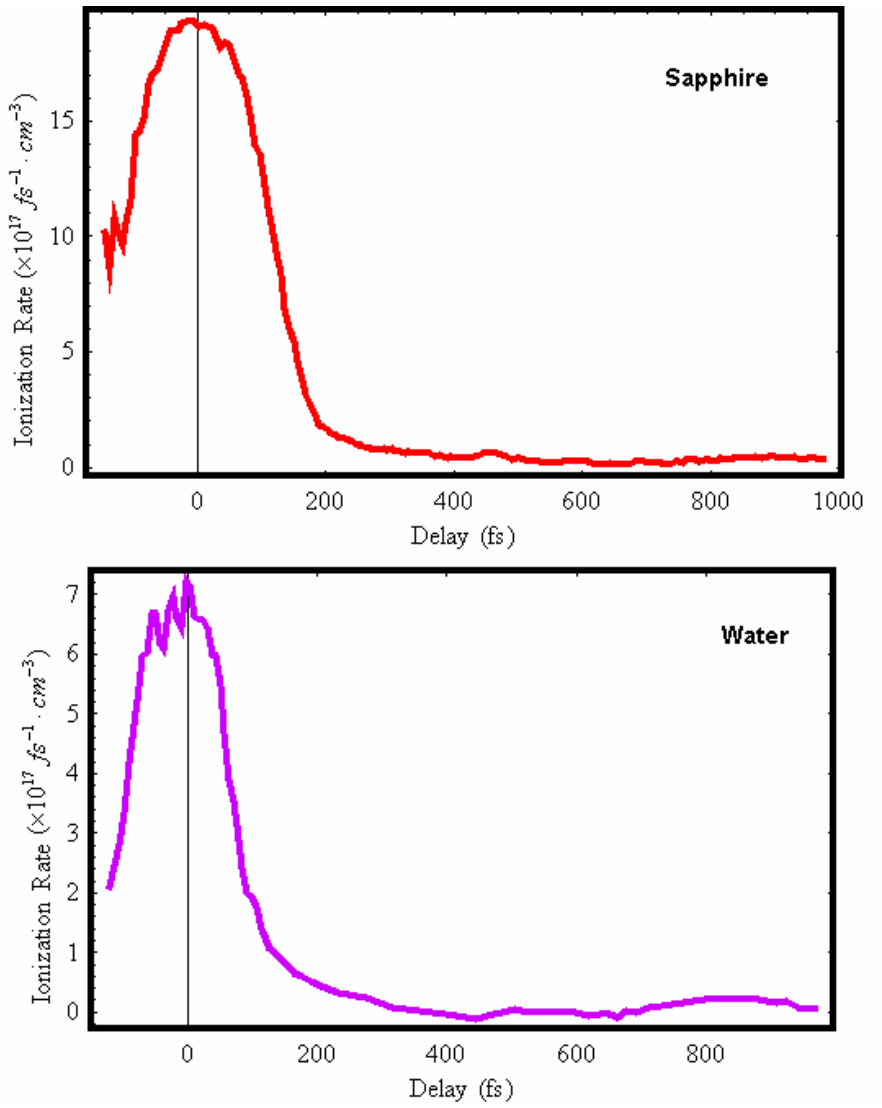

Figure 3.14 Sapphire/Water-time-varying multiphoton excitation rates. We obtain them by multiplying the blueshifting value, at each delay, with the quantity ($-2cN_{crt}/L\lambda_0$).

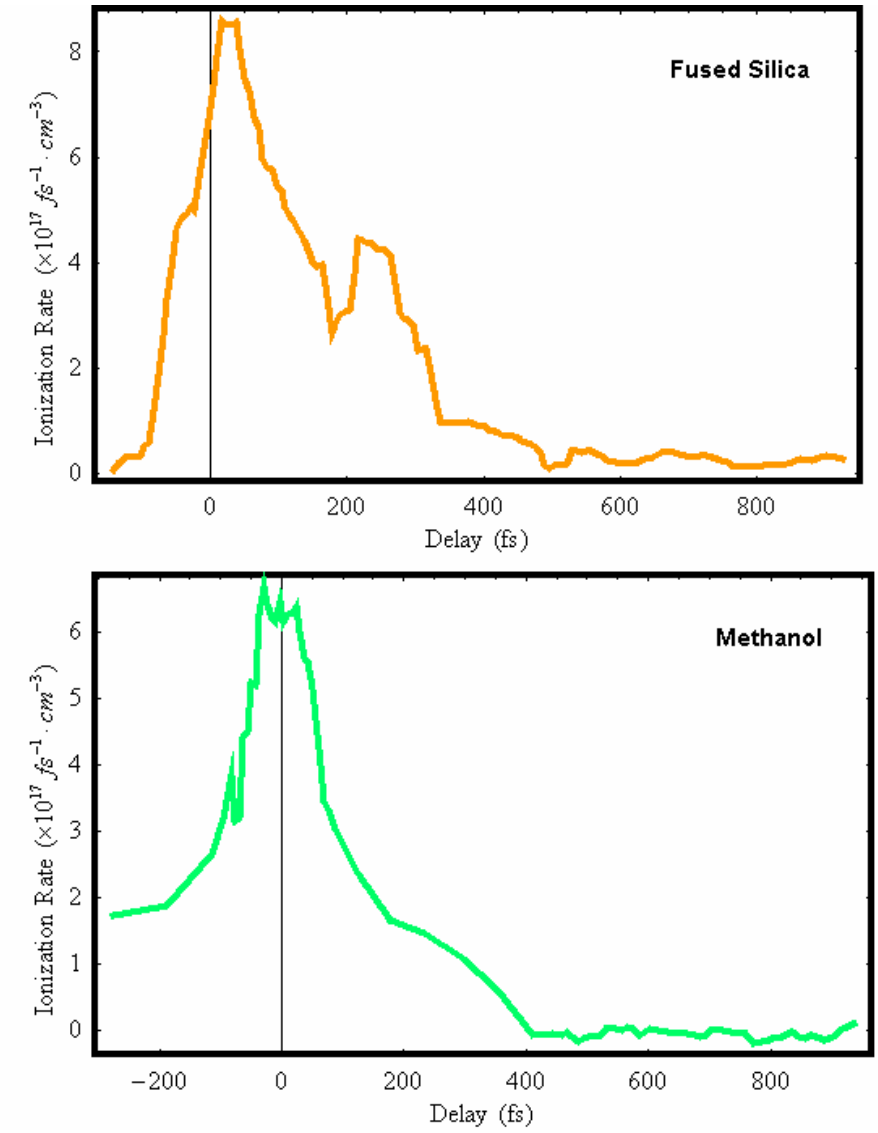

Figure 3.15 Fused Silica/Methanol-time-varying multiphoton excitation rates. We obtain them by multiplying the blueshifting value, at each delay, with the quantity ($-2cN_{crt}/L\lambda_0$).

This is extremely useful information. We not only get quantitative information about the plasma, but we also can get insight into the physics of the ionization processes. Recently in our lab, we have measured the size of the filament in a sapphire crystal and obtained a

diameter of roughly 20 micrometers. We then estimated the intensities (intensity = energy/(pulsewidth×area); the pulsewith τ = 100 fs) inside the dielectrics and extracted the values of ionization rates using Keldysh theory. Table 3.3 shows the measured peak rates and the rates given by the Keldysh theory. We also estimated the ionization rates by using Thornber's approach [25]

Material	Rate($fs^{-1} \cdot cm^{-3}$) Keldysh Theory	Rate($fs^{-1} \cdot cm^{-3}$) Measured	Rate($fs^{-1} \cdot cm^{-3}$) Thornber Theory
Sapphire	4.3×10^{14}	1.9×10^{18}	4.4×10^{19}
Fused Silica	2.3×10^{16}	8.6×10^{17}	2.4×10^{19}
Water	8.6×10^{14}	7.2×10^{17}	1×10^{19}
Methanol	2.8×10^{16}	6.6×10^{17}	1.7×10^{19}

Table 3.3 Comparison between measured and calculated ionization rates.

Our experimental results provide *quantitative* information about the excitation processes in solid media and they constitute a first step toward identifying the excitation mechanism. There is a widespread consensus in the field that in the ultra-short pulse regime, below the damage threshold, the dominant mechanism is the MPE and that the AI plays no role or its role is negligible. Our measured ionization rates are consistently larger that the theoretical rates. This could mean that (1) Keldysh theory does not

correctly describe the excitation in solids in the ultrafast regime, (2) If the multiphoton excitation (MPE) is the dominant process, then we have to assume that lower order MPE (if impurities introduce energy levels in the band gap, then the number of photons required to cross it decreases) plays an important role or (3) Avalanche ionization has a more important contribution than previously thought. The Thornber theory clearly does not apply to ionization in solids, in the ultrashort regime. The MPE and the AI have different intensity dependence and it should be possible to experimentally separate them. We performed an absorption experiment (to be described in the next chapter) that suggests that avalanche ionization contributes to the plasma formation, for ultrashort pulses, bellow the threshold damage.

3.8 Electron Densities Determination

Time integration of the calculated ionization rates results in values of the electron densities. Fig. 3.16 shows the electron density as a function of time delay between the pump and the probe in the case of sapphire. Also shown in the picture is the intensity of the scattered probe.

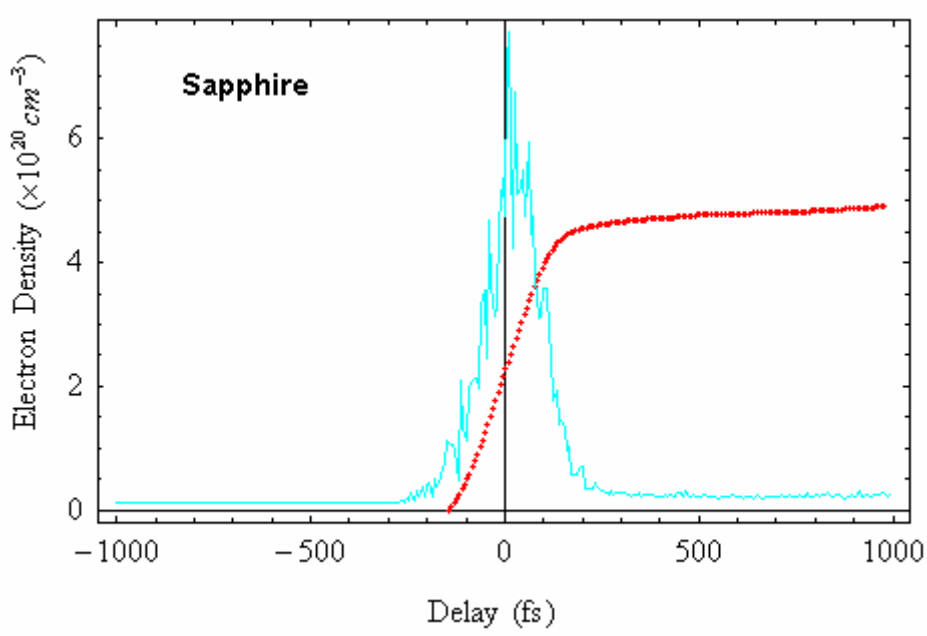

Figure 3.16 Sapphire- Electron density and the intensity of the scattered probe as a function of time delay between the pump and the probe.

Electrons are created in the leading edge of the pump and their density increases over a period of time of approximately 250 fs, after which it reaches a constant value. Fig. 3.17 shows the time-dependent densities for all four materials.

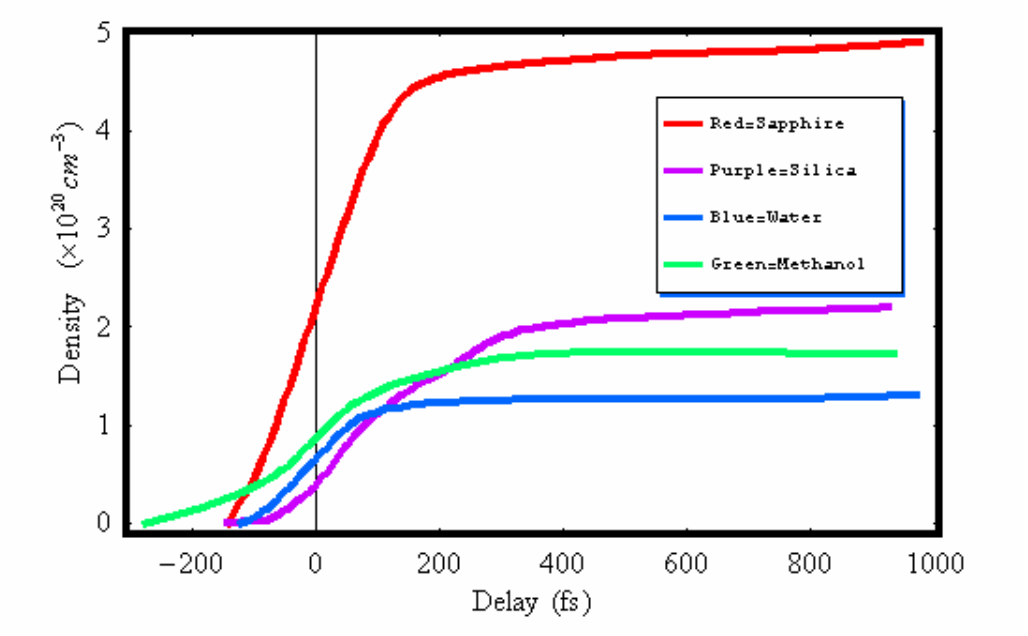

Figure 3.17 Time-varying electron densities for all four media.

The peak densities are summarized in Table 3.4.

Material	Peak Density (cm^{-3})
Sapphire	$4.9 \cdot 10^{20}$
Fused Silica	$2.2 \cdot 10^{20}$
Water	$1.3 \cdot 10^{20}$
Methanol	$1.7 \cdot 10^{20}$

Table 3.4 Peak electron densities for all four media

We also compared the values of our peak densities to the ones obtained by F. Quere *et al*, [60] which used a frequency domain interferometry technique. They measured the excited carrier density in SiO_2, MgO and Al_2O_3 irradiated by short laser pulses at intensities above and below damage threshold. For sapphire, the above cited research group assumed an intensity of $10^{14}\ W/cm^2$, which they said was below the damage threshold, and calculated a peak density of $8.0\times10^{19}\ cm^{-3}$. Our result for sapphire was roughly six times larger than this value and our intensity was roughly $1.3\times10^{13}\ W/cm^2$ and never reached the high value cited in Ref. 60. For fused silica they obtained a peak density value of $2.3\times10^{20}\ cm^{-3}$ for an intensity of $8.0\times10^{12}\ W/cm^2$. Our value was similar to this but it corresponded to a higher intensity $1.4\times10^{13}\ W/cm^2$.

3.9 Numerical Calculation

In section 3.5 of this chapter we showed spectra at selected time delays between the probe and the pump along with the results from a 1-D calculation

For this calculation we described the pulses as Gaussians both in time and space:

$$I_{pump}/I_{0,pump} = e^{-4\ln 2\frac{t^2}{\tau_{pump}^2}}\cdot e^{-4\ln 2\frac{r^2}{r_o^2}}$$

$$E_{probe}/E_{0,probe} = e^{-4\ln 2\frac{t^2}{\tau_{probe}^2}} e^{-i\omega t}$$

In the above equations τ_{pump} and τ_{probe} are the pulse widths (FWHM) of the pump and the probe and r_0 is the spot size (FWHM) of the pump. In this model we only took into account the multiphoton excitation:

$$\frac{\partial n_e}{\partial t}(r) = \sigma_k \cdot I_{pump}^k ,$$

where k is the number of photons required to cross the band gap and σ_k is the ionization cross-section.

The interaction between the pump and the materials was described by only taking into account the Kerr effect and the excitation of the medium. These processes give rise to a probe phase shift

$$\Delta\Phi^{probe} = (n_e + n_{Kerr}) \cdot \frac{2\pi}{\lambda_0} L$$

$$\approx (-\frac{\pi}{\lambda_0 N_{crt}} N_e + \frac{2\pi}{\lambda_0} n_2 I_{pump}) \cdot L$$

In the above phase shift expression n_e and n_{crt} are the contributions to the refractive index of the medium due to Kerr effect and plasma formation. We also used the fact that the conduction electrons generated in the process change the refractive index of the medium proportional to their time-varying density $n = (1 - N_e / N_{crt})^{1/2}$ and for $N_e << N_{crt}$ we can make the approximation $n \approx 1 - N_e / 2 \cdot N_{crt}$. The electron density and the critical density are indicated by N_e and N_{crt}.

The simulation stores the complex electric field of the scattered probe, after it propagated through a distance L, on a two dimensional grid in (r, t) space. The grid size and spacing is chosen by the user as needed. Typical time and space steps used in the

simulation are 1 fs and 1 μm, respectively. For a given simulation the peak of the input pulse is defined to be at t = 0, with negative times indicating the leading edge of the pulse and positive times indicating the trailing edge of the pulse. Typical grid size was 4096 points along the time axis and 10 points along the radial axis.

The user inputs the initial pulse shape, material parameters, propagation distance and the multiphoton ionization constant. The input pulse is always defined to have a Gaussian shape in the radial and time dimensions and the user chooses the FWHM, the peak intensity. We attempt to match the data by a trial and error process.

Although the calculation is very simple, it seems to describe the blue-shifting effect well. For the cases presented in this thesis, we ran the calculation with the parameters shown in Table 3.5

Material	$I_0^{pump}(W/cm^2)$	$\sigma_k(fs^{-1}\cdot cm^{2k-3}W^{-k})$	$\tau_{pump}(fs)$	$\tau_{probe}(fs)$	$L(\mu m)$
Sapphire	1	10^{19}	200	100	3000
Water	1	10^{18}	200	100	70
Fused Silica	1	10^{18}	200	100	70
Methanol	1	10^{18}	200	100	70

Table 3.5 Numerical values of the parameters used in the probe spectrum simulation.

The fused silica spectra show oscillations both at positive and at negative delays. The explanation consists in the fact that pump beam is not 100% horizontally polarized. Therefore part of the pump leaks through the polarizer that is supposed to block it and goes into the spectrometer. The effect of the spectrometer is that it broadens the pulses in time and therefore there is interference between the leaked light and the probe.

Note also that the agreement between the theory and experiment is quite good for fused silica, water and methanol, but is somewhat different for the sapphire. It is very likely that this simple model misses some processes that become important to the spectrum broadening in sapphire.

CHAPTER 4

IONIZATION MECHANISMS IN THE INTERACTION OF ULTRASHORT PULSES WITH SOLIDS – REVIEW OF THE FIELD

4.1 Introduction

The ionization of solid state media under the action of strong optical radiation can be caused by either of the two mechanisms. The first is direct photoionization which is usually itself divided into two regimes: multiphoton and tunneling. Electrons can be detached from atoms as a result of the multiphoton ionization, i.e., as a result of simultaneous absorption of several photons. In addition to the multiphoton ionization, electrons can be detached from atoms via tunneling through the barrier formed by the lattice potential and the time-varying applied field. The electric field of an electromagnetic wave behaves as if it were a static field if it does not vary greatly during the time taken by an electron to cross the potential barrier of an atom. It would appear that the multiphoton effect and the tunnel effect are completely different processes. However, in the classic paper by L.D. Keldysh[17], he showed that both mechanisms were

of common origin and were the limiting cases of the same process of the transition of an electron from a bound to state in an atom to a free state under the action of an alternating electric field. Keldysh obtained a formula for the probability of detaching an electron from an atom. The ionization rate formula was given in Chapter 2. This theory was applied to describe the ionization of gases by ultrashort lasers and was generally found to be lacking. More successful approaches (KFR[17,79,80] and ADK[81]) required a better treatment of the initial and/or final states, but still remained consistent with the view of ionization having multiphoton or tunneling character. The Keldysh parameter is still used and appears valuable. In the case of solid media the experiments indicate large discrepancies. The second mechanism is the avalanche ionization. In this case, if some "seed" electrons appear from photoionization in the region where the field is active, these electrons can acquire energy from the field. In a static electric field, a seed electron is simply accelerated along one direction until the first collision and the energy lost by scattering is transformed into heat. In an oscillating field, the electron oscillates, but it is found[74,75] that on average, the kinetic energy of its oscillation is also transformed in each collision with an atom into the energy of random motion, so that the velocity of the random motion increases. This classical representation is suitable for fields of moderately high frequencies, including the microwave range. In quantum language, which is appropriate in the optical frequency range, electrons acquire energy by absorbing photons during collisions with atoms, and this is the process of inverse bremsstrahlung emission of quanta. Having acquired enough energy (equal or larger than the band gap), an electron ionizes an atom and this produces two slow electrons which repeat the process

and so on. In this way the number of electrons increases readily resulting in "avalanche". This is an ultrafast picture of the process. For slow pulses, the seed electrons are thermal.

The ionization of solids by ultrashort, extremely powerful pulses is worth special attention and has generated a great amount of controversy. If the probability of n-photon ionization is proportional to the n-th power of the intensity: $w^{MPI} = C_n \cdot I^n$ (where C_n is the multiphoton ionization constant) and if a focal region of volume V contains $N_a = n_a \cdot V$ atoms, a pulse of duration τ generates [75]

$$N_1 = N_a V C_n I^n \tau$$

electrons. On the other hand the number of generations of electrons created in an avalanche ionization is proportional to $I \cdot \tau$ (see Chapter 1) or $I^{1/2} \cdot \tau$.[25] Clearly, in the case for high values of n and for high densities we can select such a short time τ that, in spite of a very high intensity, the avalanche does not develop.

In solid state media some of these qualitative predictions are brought into question. In this chapter I am going to review the experiments that have directly or indirectly dealt with the problem of ionization in the field of ultrashort, powerful laser pulses. I will discuss the results and conclusions obtained from these experiments and the significance of the results in the previous chapter. This review is also important for understanding of the following chapter.

There are three main points that are subject to controversy in this field:

- The intensity dependence of the avalanche ionization rate ($I \cdot \tau$ or $I^{1/2} \cdot \tau$?)
- The individual contribution of the multiphoton ionization versus the avalanche ionization in the below the breakdown threshold regime and

- The validity of Keldysh theory when applied to solid state media and in the case of ultrashort pulse.

4.2 History of the field

W. L. Smith *et al*[76] studied the production of continuum generation in H_2O and D_2O by 30 picosecond pulses at 1.06 μm and 21 picosecond pulses at 0.53 μm. They found that the production of the superbroadening is preceded by catastrophic self-focusing, filament formation and breakdown. The conclusion was that self-phase modulation of the rapidly varying index of the plasma provided seed light over a superbroadened spectral interval, which was largely independent on the host material. This seed was assumed to be further amplified by stimulated Raman gain and four-photon parametric interactions.

R.L. Fork and coworkers[47] obtained, in ethylene glycol, gigawatt white-light continuum pulses that extended continuously from 0.19 μm to 1.6 μm. They found that the temporal, spatial and spectral properties are consistent with self-modulation playing a prominent role in the generation of the continuum. They compared their results to the ones obtained by W. L. Smith *et al* and concluded that they did not see any clear evidence for avalanche ionization.

D. Du and coworkers[59] performed laser-induced breakdown experiments in fused silica (SiO_2) employing 150 fs -7 ns, 780 nm laser pulses. The experimental results showed that the breakdown thresholds increased when the pulse width became shorter

than a few picoseconds. They used Thornber's calculation of the avalanche coefficient, which predicted an avalanche ionization intensity dependence of $I^{1/2}$, to calculate the breakdown threshold and found an excellent agreement with the experimental data.

B. C. Stuart and coworkers[44] reported extensive measurements of damage thresholds for fused silica and calcium fluoride at 1053 nm and 526 nm for pulse durations ranging from 270 fs to 1 ns. In each of these band gap materials they observed a change in the damage mechanism and morphology for pulses shorter than 20 ps. More importantly, they observed a deviation from $\tau^{1/2}$ scaling reported by Du *et al*, finding no evidence for an increase in damage threshold with decreasing pulse width. They were able to fit the experimental by using a theoretical model that assumed that field-induced MPI produced free electrons which were then heated rapidly by the pulse, resulting in further ionization by collisions. In their model, the MPE rate was given by the strong field Keldysh ionization formula, while for avalanche ionization a linear intensity dependence was found to match the data. The avalanche ionization constant was found to be $\alpha = 10\ \mathrm{cm}^2/\mathrm{J}$.

M. Lenzner *et al*[18] also reported measurements of optical breakdown thresholds in dielectrics with different band gaps for laser pulse duration ranging from 5 ps to 5 fs, at 780 nm. For $\tau < 100$ fs, they found that the dominant channel for free electron generation was either avalanche or MPI, depending on the size of the band gap. In order to fit their data, they had to use MPI rates that were substantially lower than those predicted by the Keldysh theory. Avalanche ionization was assumed to depend linearly

on intensity. Typical value for the avalanche ionization constant were $\alpha^{fused\_silica} = (4 \pm 0.6)\ \mathrm{cm}^2/\mathrm{J}$ and $\alpha^{BBS} = (1.2 \pm 0.4)\ \mathrm{cm}^2/\mathrm{J}$.

A.-C. Tien and coworkers[45] also presented single-shot damage threshold measurements and modeling for fused silica at 800 nm as a function of pulse duration down to 20 fs. The experimental data is very well matched by a model that uses Thornber formula for the avalanche ionization rate (square root intensity dependence) and the full Keldysh formula for the photoionization rate.

A. Brodeur and S.L. Chin[16] investigated the supercontinuum generation during self-focusing in several transparent media by using 140-femtosecond Ti:sapphire laser pulses. A band gap threshold was found above which the width of the continuum increased with increasing band gap and below which there was no continuum generation. Multiphoton excitation of electrons into the conduction band was proposed as primary mechanism for these observations. They explained the ultrafast continuum by reviving Bloembergen's model[77] of ionization-enhanced self-phase modulation in the context of femtosecond pulses and multiphoton excitation. According to this model, during self-focusing a sharp intensity spike develops which is limited by MPE up to a density $N_e^{stop} \sim 10^{18}\ \mathrm{cm}^{-3}$ (in water). They estimated, based on the measured energy loss and self-focal dimensions, that the electron density created in water was $10^{18} < N_e < 10^{18}\ \mathrm{cm}^{-3}$. Based on these measurements they assumed that in their experiments self-focusing was stopped by MPE.

M. Li *et al*[19] measured the optical breakdown threshold in dielectrics with different band gaps for single and double 25 fs 800 nm transform-limited laser pulses.

Theoretical breakdown thresholds were calculated assuming a linear intensity dependence of the avalanche ionization rate and the MPI approximation of the Keldysh photoionization formula. The MPI rates that fitted the data were found to be several order of magnitude smaller than what the Keldysh theory predicted (for the same intensities). The impact ionization constants that fitted the data best were and α^{fused_silica} = 9 cm^2/J and α^{BBS} = 6 cm^2/J.

A. L. Gaeta[13] investigated theoretically the self-focusing dynamics of an ultrashort laser pulse both near and above the threshold at which the pulse effectively undergoes catastrophic collapse. He assumed that the electron density can grow in the presence of the laser field through avalanche ionization (linear dependence on the intensity) and multiphoton absorption. In all the cases he studied, Gaeta found that for pulses in the femtosecond regime, although multiphoton absorption provided the initial free electrons, avalanche ionization dominated the total production of plasma density.

S. Tzortzakis and coworkers[20] reported self-guided propagation of ultrashort infrared pulses in fused silica over several Rayleigh lengths. The experiments showed that self-guiding was accompanied by pulse splitting and time compression. Numerical simulations involving pulse self-focusing, temporal dispersion, and multiphoton were found to be in good agreement with the experimental results. No significant avalanche contribution is observed in the femtosecond filamentation in their experiment. The numerical simulation uses the MPI rate as given by Keldysh theory and a linear dependent avalanche rate with the ionization constant α^{fused_silica} = 1 cm^2/J.

H. Ward and L. Berge[22] investigated theoretically how femtosecond light pulses interact with solids. They found that with a power close to the self-focusing threshold, an

optical pulse evolves like a solitary wave with a temporal duration shrunk to a few femtoseconds through the defocusing action of the multiphoton ionization (described by Keldysh strong field formula).

L. Sudrie *et al*[21] studied bulk damage induced by femtosecond infrared pulses in fused silica both experimentally and numerically. The theoretical model uses the full Keldysh formula for the photoionization. In the case of the avalanche ionization they found that a linearly dependent ionization rate agreed with the experimental data better than a square root dependent one. It is found that the avalanche became significant only when the density of electrons created by photoionization exceeded 10^{19} cm^{-3}.

A summary of this review is presented in Table 4.1 and Table 4.2.

Group	Smith *et al*[76]	Fork *et al*[47]	Du *et al*[59]	Stuart *et al*[44]	Lenzner *et al*[18]	Tien *et al*[45]
Pulse	30 ps / 1.06 μm 21 ps/0.53 μm	80 fs/627 nm	780 nm 150 fs to 7 ns	526 / 1053nm 150 fs to 7 ns	780 nm 5 fs to 5 ps	800 nm 20 fs
Media	H_2O/ D_2O	Ethylene glycol	SiO_2	SiO_2 CaF_2	SiO_2 BBS	SiO_2

Table 4.1 Summary of the results found in the literature.

Table 4.1 (continued)

Group	Smith *et al*[76]	Fork *et al*[47]	Du *et al*[59]	Stuart *et al*[44]	Lenzner *et al*[18]	Tien *et al*[45]
PI/AI Dominant	AI	MPI	Tunneling	MPI		
AI I or $I^{1/2}$			$I^{1/2}$	I	I	$I^{1/2}$
Breakdown Study	No	No	Yes	Yes	Yes	Yes
Keldysh Theory Agreement			No	Yes	No	Yes

Group	Brodeur *et al*[16]	Li *et al*[47]	Gaeta *et al*[13]	Tzortzakis *et al*[20]	Ward *et al*[22]	Sudrie *et al*[21]
Pulse	140 fs / 796 nm	25 fs /800 nm	70 fs /800 nm	160 fs /800 nm	160 fs /790 nm	160 fs /800 nm

Table 4.2 Summary of the results found in the literature.

Table 4.2 (continued)

PI/AI Dominant	MPI		AI	MPI	MPI	AI
Media	15 media with BG b/w 3.3 eV and 11.8 eV	SiO_2 BBS	SiO_2	SiO_2	SiO_2	SiO_2
AI I or $I^{1/2}$			I	I	I	I
Breakdown Study	No	Yes	Yes	No	No	Yes
Keldysh Theory Agreement		No		Yes	Yes	Yes

From our experiment we were able to estimate both the multiphoton ionization constant and the avalanche ionization constant. The measured ionization rate for our fused silica sample was $1.1 \cdot 10^{18}$ $cm^{-3} \cdot fs^{-1}$, for a laser intensity of $1.4 \cdot 10^{13}$ $W \cdot cm^{-2}$. The multiphoton cross section will therefore be given by the formula σ_k = Rate/I_k, with k = 5 or 6, depending on the band gap and for a wavelength of 800 nm. For k = 6 we obtain σ_6^{FS} = 1.5×10^{14} $ps^{-1} \cdot cm^{9} \cdot TW^{-6}$. In the case of the avalanche ionization the cross section is

given by the formula α = Rate/ (I·n$_e$) and the measured quantities used provide a value of $\alpha^{FS} = 1.0\ \mathrm{cm}^2/J$. A comparison of these quantities ($\sigma_6^{FS}, \alpha^{FS}$) with other values obtained also experimentally is given in Table 4.3. First observation is that none of the experimental values for the multiphoton ionization constant matches the theoretical values given by Keldysh theory. While M. Lenzner *et al*[18] and M. Li *et al*[47] obtained values that were orders of magnitude smaller than what the Keldysh theory predicted, we calculated a constant that was two orders of magnitude larger than the theoretical value. In the case of the avalanche ionization constant, the calculated values, for band gaps between 6.5 eV to 9.0 eV varies from 7.6 cm^2/J[24] to 1 cm^2/J.[21]

Group	MPI Ionization Coefficient $\sigma_k\ (\mathrm{cm}^{-3}\cdot\mathrm{ps}^{-1}\cdot(\mathrm{cm}^2/\mathrm{TW})^k)$ SiO_2	AI Ionization Coefficient $\alpha\ (\mathrm{cm}^2/\mathrm{J})$ SiO_2
Lenzner *et al*[18]	$\sigma_6 = 6\times10^{8\pm0.9}$	$\alpha = (4\pm0.6)$
Li *et al*[47]	$\sigma_6 = 3\times10^4$	$\alpha = 9.0$
Our Results	$\sigma_6 = 1.5\times10^{14}$	$\alpha = 1.0$

Table 4.3 Comparison between our experimental results and results found in the literature, for fused silica.

As a conclusion of this brief review (there are many other studies that advance the same ideas as the papers presented in this chapter), we can say that the ionization processes in solid media, by ultrashort pulses, are far from being well understood. Many of the present studies point to the fact that very often the qualitative and the quantitative results vary as a function of experimental conditions and that there is a disagreement in the field about what ionization processes are involved and about what their relative contributions are. This thesis proposes an experimental technique that allows a direct measurement of the ionization rates as oppose to getting them from fitting parameters. We also present measurements that separate the two excitation processes and identify the relative role played by each in the ionization of the media.

CHAPTER 5

NONLINEAR ABSORPTION MECHANISMS

5.1 Introduction

Laser pulses with very low energies propagate through transparent materials unabsorbed and unmodified. When the energy, and therefore the intensity, of the pulses increases nonlinear processes come into play and make possible the promotion of electrons from the valence to the conduction band, hence the absorption of light in an otherwise transparent material. We reviewed in Chapter 2 the two classes of nonlinear excitation involved when ultrashort laser pulses propagate through transparent media: photoionization and avalanche ionization. Under the experimental conditions considered in this thesis, photoionization was a multiphoton process, not tunneling. In this chapter we present measurements that separate the two excitation processes and identify the relative role played by each in the ionization of media. The idea underneath these experiments is a very simple one: since the two ionization processes have different

intensity dependence, the absorption of light in the medium should differ similarly. Therefore it should be possible to distinguish the two mechanisms by looking at the energy dependence of the absorption.

5.2 Experimental Setup

Our experimental apparatus was simple. The 100 fs, nearly transform-limited light came from an optical parametric amplifier system operating at a repetition rate of 1 kHz and signal wavelengths ranging from 1200 nm to 1600 nm. The light was sent into a nonlinear crystal (BBO) that doubled the frequency of the light and generated new light (second harmonic of the OPA signal) with wavelengths spanning from 600 nm to 800 nm. We also performed the experiment at 400 nm by doubling the 800 nm light. We sent the fundamental and the second harmonic through a pair of prisms that not only dispersed the light and separated the infrared from the visible, but also compensated for the positive GVD acquired by the visible light in passing through the nonlinear crystal and the various optics employed in the experimental setup. The second harmonic was sent through a pair of polarizers, one of which had a motor attached to it. By rotating the motor we change the polarization of the light and therefore we change the amount of transmitted light through the second polarizer. The light is then focused by a 100 mm lens into a 3 mm sapphire substrate. Great care was taken to push the focus as close as possible to the back of the substrate and to still have continuum generation. The sapphire substrate had a device grade polish and its c axis was perpendicular to its surface. The transmitted light was recollected by a second lens and sent into a powermeter (Scientech

362). The powermeter had an analog output and the signal from it was sent into a digital to analog converter and subsequently into a computer.

A simplified picture of our experimental setup can be seen in fig. 5.1.

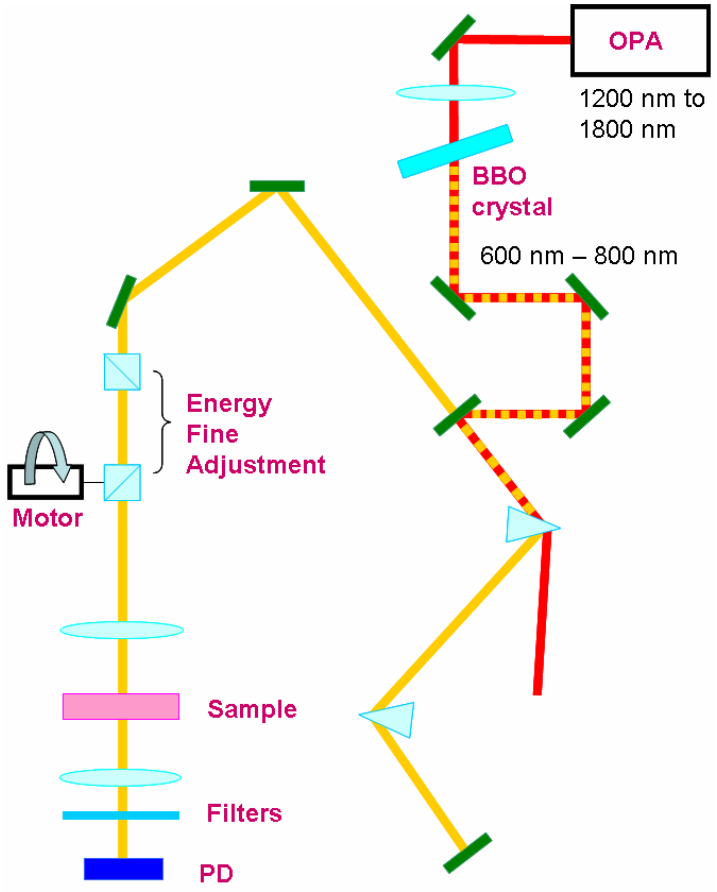

Figure 5.1 The experimental setup is straightforward. The beam was sent into a BBO crystal which generated visible light. We sent the pulses through a sapphire crystal and measured the absorption with a powermeter.

5.3 Nonlinear Absorption: Multiphoton Excitation versus Avalanche Ionization

First observation is that we generated white light for each laser pulse wavelength employed except when using light at 400 nm. No matter how hard we pumped the sapphire crystal we could not damage it or generate other colors for this particular wavelength. Sapphire has a band gap of 9 eV and when using the blue light it only takes three photons of this color to cross the band gap. For comparison it takes 5, 6 and 10 photons for light at 590 nm, 800 nm and 1280 nm to cross the same band gap. This means electrons are generated very easily with the blue light. The electrons defocus the beam and they stop the self-focusing and all the other nonlinear processes very early, making impossible the generation of white light. Figure 5.2 shows the transmitted light as a function of the input energy for three different colors.

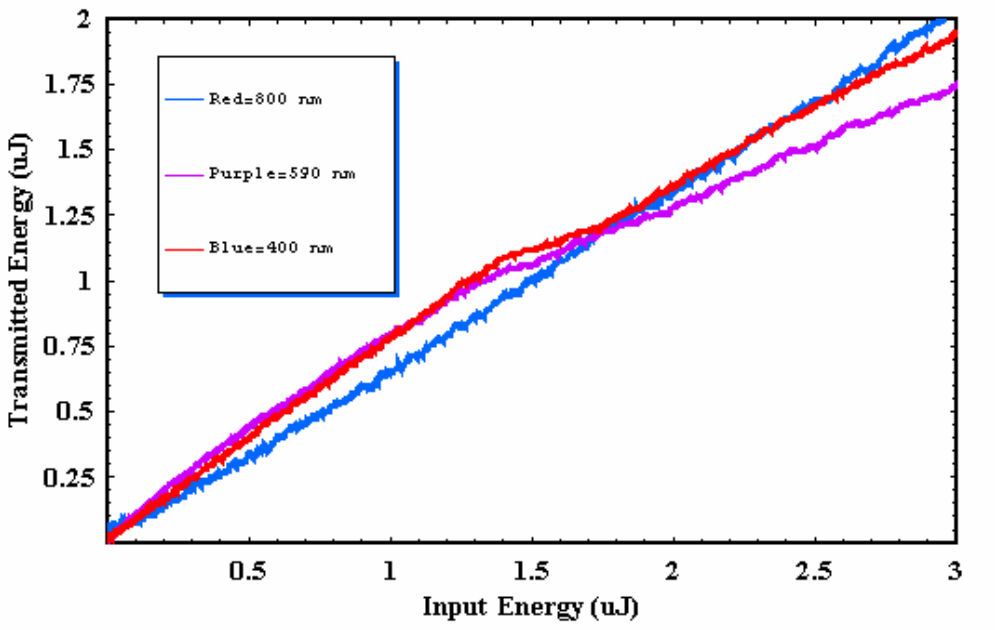

Figure 5.2 The transmitted energy shows that different mechanisms are at play for absorption of the light at 590 nm and 800 nm when compared to the results at 400 nm.

It is clearly seen from the picture above that there is a change in the slopes of the transmission curves corresponding to light at 590 nm and 800 nm. The point corresponding to this transition coincides with the point in energy at which the continuum generation is fully developed. Blue light never drives continuum generation and there is no change in the transmission curve slope. We wanted to investigate more closely what the change in slope meant. For each color we calculated the transmission of the light and the nonlinear absorption (the measured absorption corrected for the reflections on the faces of the crystal). Once we calculated the nonlinear absorption we simply took the logarithm of the absorption and the logarithm of the input energy and read the order of the nonlinearity. Figures 5.3 and 5.4 illustrate the way we analyze the data and it also shows the final experimental results.

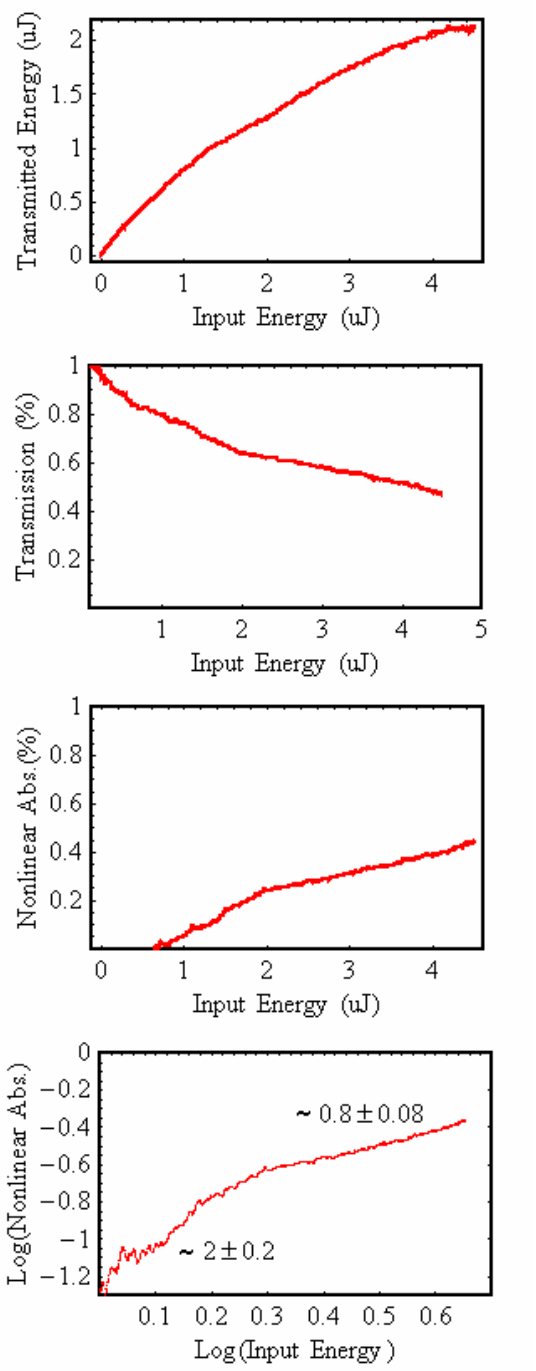

Figure 5.3 The nonlinear absorption at 590 nm shows a nonlinear slope of about 2 up to the point where the continuum generation is created and then a slope of about 0.8 after the white light has been created.

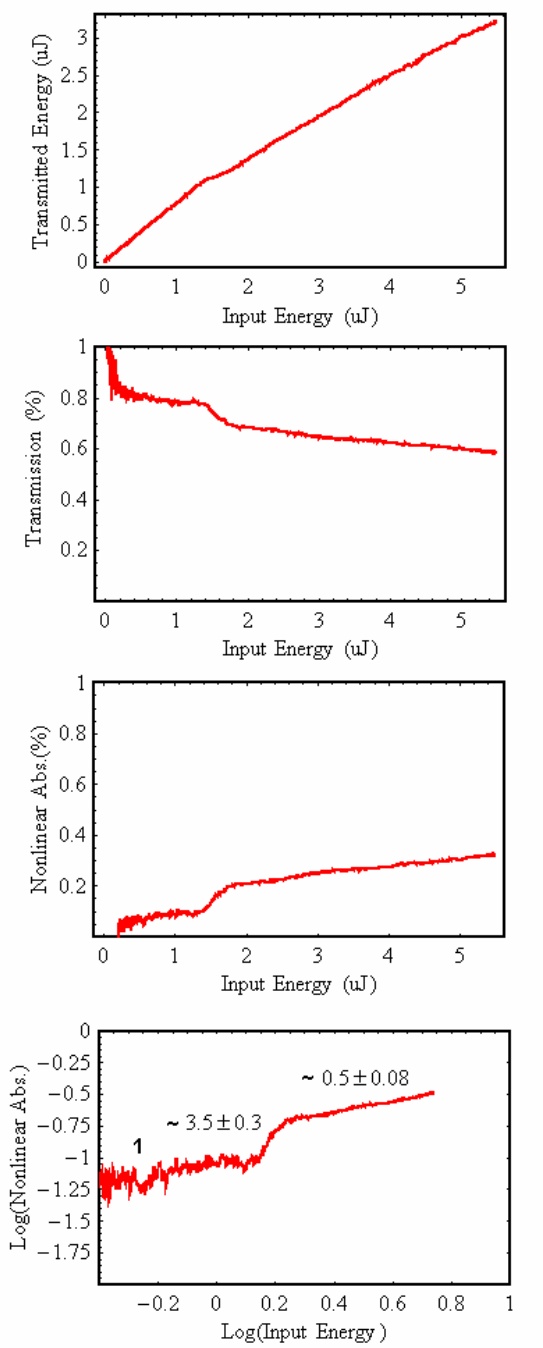

Figure 5.4 The nonlinear absorption at 800 nm shows a linear slope, followed by a nonlinear slope of about 3.5 up to the point where the continuum generation is created and then a slope of about 0.5 after the white light has been created.

One can observe from the pictures showing the results at 800 nm that for small input energies the light simply propagates linearly; this region corresponds to a slope equal to 1. In the data taken using 590 nm light, this region was lost when processing the experimental data. In order to find the transmission we have to divide the values of the transmitted energy by the values of the input energy. Mathematically, for very small energies, this means that we divide by very small numbers, hence numerical noise and loss of data. However, at the point where continuum generation first appears we can see a change of the slope in both set of data. There is a nonlinear slope in the curve that stops exactly at the point where the continuum generation is fully formed. We believe that the nonlinear slope is an indication of a multiphoton process corresponding to an absorption that varies as I^k, with k being the number of photons required to cross the band gap. Note that we did not get the slopes that we expected, 5 for 590 nm and 6 for 800 nm. This could be due to spatial averaging, imprecision in the detection or even to the existence of impurities in the band gap of the material which can lead to the modification of the order of the nonlinearity. When the multiphoton process stops, which is apparently when the continuum generation is fully formed, the slope changes to a sublinear one. We attribute this change in slope to a change in the ionization mechanism. Avalanche ionization becomes important and it is believed that the avalanche ionization rate[18,19,20,21,23] varies either as I or $I^{1/2}$.[25] We also wanted to know what the relative contribution of each of these processes is. In order to get an estimate we calculated the density of the electrons in the conduction band that is given by the following formula:[44]

$$\frac{dn_e}{dt} = \sigma_k I^k + \alpha I n_e,$$

where σ_k and α are the ionization cross-sections and n_e, I are the electron density and the intensity of the light (the intensity is assumed to be described by a Gaussian in time and space, but the calculation is performed for r = 0, where r represents the spatial extent of the beam). The ionization cross sections were estimated by using the experimentally measured ionization rates and intensities. More precisely, we estimated each of the cross-sections by assuming that the electrons are created exclusively by multiphoton ionization or avalanche ionization. We approximate the individual contributions of the two ionization processes. For example, the measured ionization rate for our fused silica sample was $1.1 \cdot 10^{18}$ $cm^{-3} \cdot fs^{-1}$. The intensity used to drive this ionization rate was $1.4 \cdot 10^{13}$ $W \cdot cm^{-2}$ and the electronic density in the conduction band was measured to be around 10^{20} cm^{-3} (as we showed in Chapter 3). The multiphoton cross section will therefore be given by the formula $\sigma_5 = \text{Rate}/I^5$. By using the numbers mentioned above, we obtain $\sigma_5^{FS} = 2 \cdot 10^{12}$ $fs^{-1} \cdot cm^7 \cdot TW^{-5}$. In the case of the avalanche ionization the cross section is given by the formula $\alpha = \text{Rate}/(I \cdot n_e)$ and the measured quantities used provide a value of $\alpha^{FS} = 1.0$ cm^2/J. It is useful to make a survey of the literature to see other results for the avalanche ionization cross sections.

M. Lenzer and coworkers[18] found, by fitting their experimental value, a value of $\alpha^{FS} = 4.0$ cm^2/J. M. Li *et al.*[19] obtained a result, also from using the ionization cross section as a fitting parameter, of $\alpha^{FS} = 9.0$ cm^2/J.

S. Tzartzarkis and coworkers[20] and L. Sudrie and coworkers[21] calculated the avalanche ionization cross section by using the Drude model[61] and the theoretical value was $\alpha^{FS} = 1.0$ cm^2/J.

Our numerical value for the avalanche ionization cross-section in fused silica is close to the other values used in the literature. We also calculated the ionization cross-sections for the other transparent media studied: sapphire, water, and methanol. A summary of our calculated cross-sections is presented in Table 5.1.

Material	$\sigma_k (fs^{-1} \cdot W^{-k} \cdot cm^{-3+2k})$	$\alpha(cm^2 \cdot J)$
Sapphire	4×10^{11}	1.5
Fused Silica	2×10^{12}	1.0
Water	2×10^{13}	0.9
Methanol	1.6×10^{14}	0.8

Table 5.1 The multiphoton and avalanche ionization cross-sections calculated by using numerical values measured experimentally for the ionization rates and intensities.

Figures 5.5, 5.6, 5.7 and 5.8 show the results of the electronic densities in the conduction band of the sapphire crystal, fused silica, water and methanol. The electronic densities were calculated by using the values in Table 5.1.

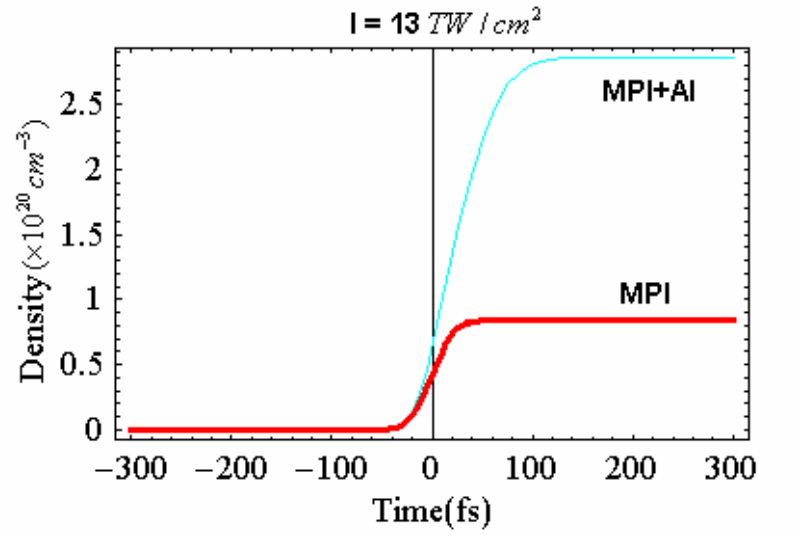

Figure 5.5 Sapphire - the red curve shows the electronic density obtained by taking into account only the contribution of the multiphoton ionization. The blue curve shows the result obtained by taking into account both the multiphoton and the avalanche ionization.

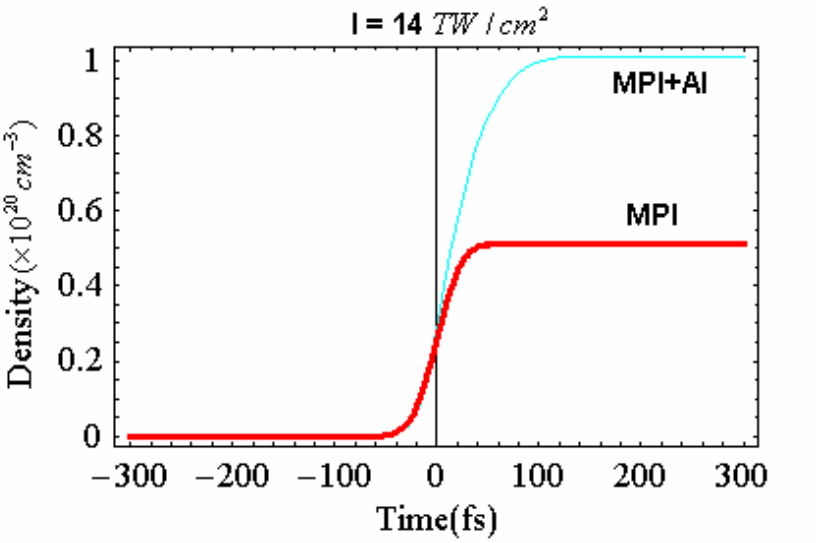

Figure 5.6 Fused Silica - the red curve shows the electronic density obtained by taking into account only the contribution of the multiphoton ionization. The blue curve shows the result obtained by taking into account both the multiphoton and the avalanche ionization.

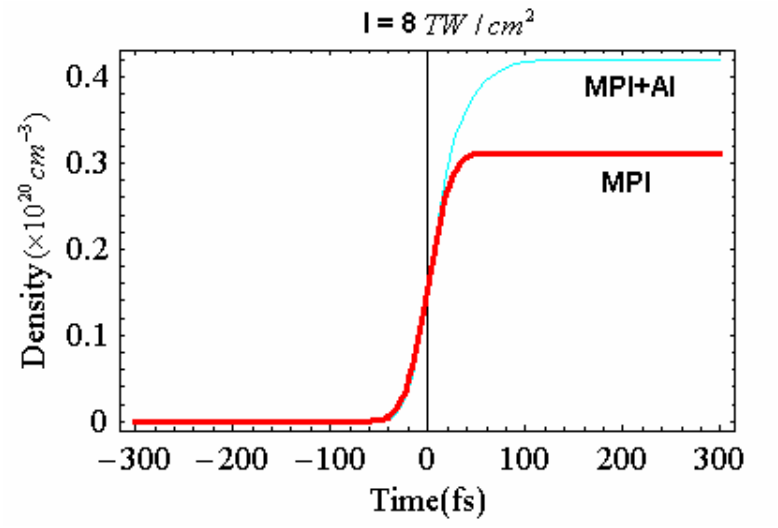

Figure 5.7 Water - the red curve shows the electronic density obtained by taking into account only the contribution of the multiphoton ionization. The blue curve shows the result obtained by taking into account both the multiphoton and the avalanche ionization.

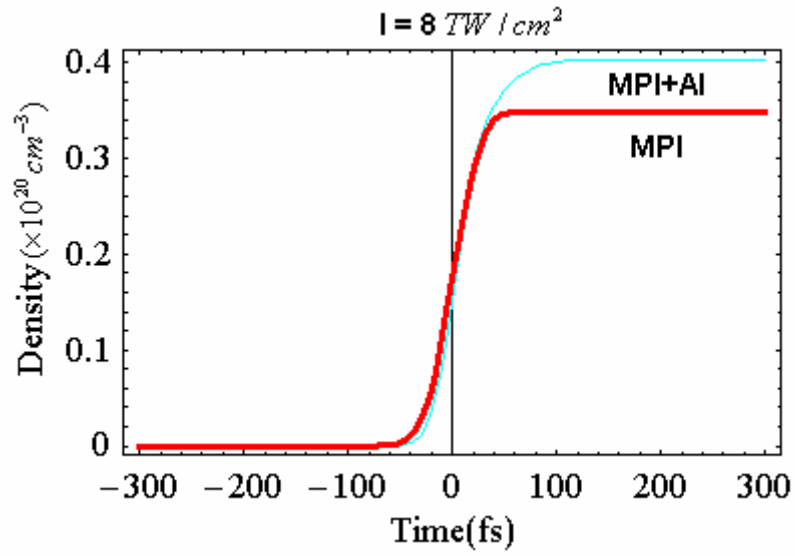

Figure 5.8 Methanol - the red curve shows the electronic density obtained by taking into account only the contribution of the multiphoton ionization. The blue curve shows the result obtained by taking into account both the multiphoton and the avalanche ionization.

From our result we can see that the avalanche ionization has a very important contribution (~ 70%) in sapphire and its contribution decreases (15% in methanol) as the band gap of the materials decreases. This is quite a different result from the widely circulated idea[18,19,20,21,22,23] that for ultrashort pulses, below the breakdown threshold, the avalanche ionization has a negligible contribution and that the main contribution comes from the multiphoton ionization process.

In conclusion we performed a simple experiment that allowed us to separate the individual contributions of the two main ionization mechanisms contributing to the creation of free electrons in condensed matter during the propagation of a short pulse laser. We find that in a regime below the breakdown threshold both mechanisms contribute to the ionization. However the contribution of the avalanche ionization seems to increase with the decreasing of the band gap. Our result challenges most of previous studies where the avalanche ionization was thought to play a minor role, if any and it separates, for the first time to our knowledge, the contribution of the two mechanisms to the creation of electrons in the conduction band in a solid.

CHAPTER 6

NONLINEAR PROPAGATION MEASURAMENTS USING A PRISM TECHNIQUE

6.1 Introduction

Obviously, one step towards understanding intense laser propagation is measuring the pulse as it travels through the medium. However you cannot place your detector inside the medium and if you wait until the light exits you have lost the information you sought to find. Several schemes have been presented to get around this problem. [82,83]
We describe a very simple approach that works spectacularly well: use of a prism to provide a variable path length.

One of the first experiments addressing the dynamics of femtosecond laser propagation in condensed matter, below the damage threshold, was the one performed by T.-W. Yau and coworkers. [62] They measured the ultrafast field evolution, in fused silica, with a three-dimensional phase-retrieval cross-correlation technique. They found that the

pulses do not focus down catastrophically; instead they are trapped momentarily to a quasi-stable single filament 20-25 μm in diameter in 4 mm propagation, without a measurable dependence on the peak power. This technique is a powerful tool for deciphering the spatiotemporal field evolution during nonlinear propagation.

Z. Wu and coworkers also performed a systematic study of the filamentation of ultrashort pulses in fused silica. They observed multiple foci for numerical apertures (NA) smaller that 0.65 and a long filament for NA = 0.85. A model in which the propagation was analogous to the movement of a classical particle in a potential well represented a qualitative explanation of the experimental results.

W. Liu *et al.*[64] also observed the phenomenon of multiple refocusing in a liquid (methanol). They show that this phenomenon is the manifestation of the interchange of energy between a wide background of the radiation and the narrow near-axis region with r < 10 μm. This study of multiple refocusing widens the concept of filament to an extended region along which the intensity is changing weakly.

A. Dubietis and coworkers studied in a series of papers[65,66,67] the phenomenon of self-guided propagation of femtosecond lasers in water. They observed light filaments with diameters of 20 μm – 60 μm that persisted over a distance of 20 mm. Their studies revealed that light filaments are not sustained by static balance between Kerr-induced self-focusing and plasma-induced self-focusing, but instead they require an important energy refilling by the surrounding radiation that one can by no means consider them in terms of solitonlike beams. They also showed that the light filaments can reconstruct themselves after hitting a beam stopper in the presence and in the absence of a nonlinear

medium. A possible scenario by which conical wave components are generated inside the medium by the distributed stopper or reflector created by nonlinear losses or plasma was presented.

Our experiment proposes a simple technique that allows easy access to directly measure the plasma induced blue shifting and the plasma dynamics as a function of propagation length. We find that the supercontinuum generation, the plasma formation, self-focusing, self-phase modulation and all the other nonlinear processes involved in the ultrashort laser propagation can require only a small threshold propagation distance, as short as 50 μm. We measured a light filament over a range up to 2.0 mm and observed that the blue-shifting was the same over the entire length of the filament. This allows us to directly estimate the ionization rates and study plasma dynamics in a very direct manner, without resort to fitting by numerical models.

.

6.2 Experimental Setup

The experimental approach as applied to the study of intense field propagation in a sapphire prism is shown in Figure 6.1 and it is similar to the one described in Chapter 3. The pump pulse propagates through the prism driving intense field excitation (IFE), continuum generation and suffering self-focusing. The delay time is defined as being negative when the probe pulse precedes the pump. At positive delays the probe comes after the pump. The weak probe pulse scatters from the plasma and can be detected in both the forward and backward directions. The probe is separated from the pump using polarizers as shown. An experimental run consisted on measuring the scattered light

spectrum while changing the time delay between the two pulses, at various path lengths. The propagation distance through the crystal is changed by simply translating the prism as it is shown in Figure 6.1.

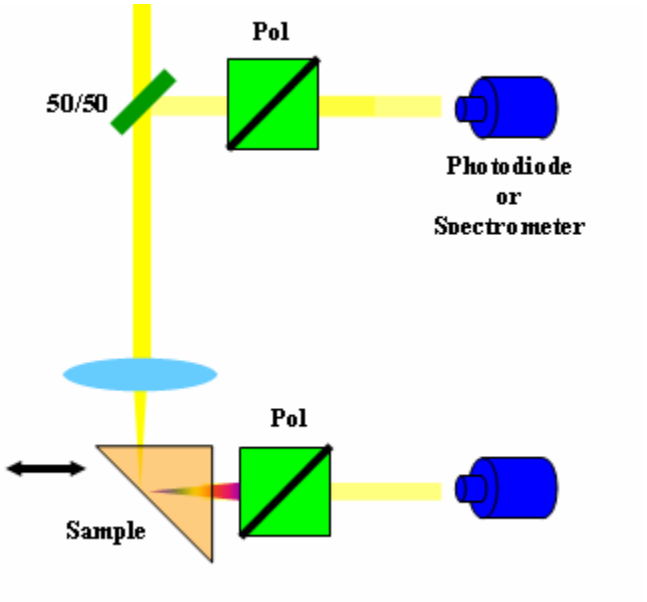

Figure 6.1 The experimental setup is straightforward. A double pulse with variable delay appropriate for a pump-probe experiment enters the beamsplitter from above. The two pulses for our work were distinguished by having orthogonal polarizations.

Typical results for a path length of 3 mm are shown in Fig. 6.2. The reflected probe is proportional to the plasma size and density in the medium. A fast rise on the same time scale as the pump pulse is followed by a slow exponential decay. There are actually two exponential decays: one that fits the data from 0 ps to 85 ps, with the time constant of roughly 77 ps and the other one fits the data from 85 ps to 150 ps with a time

constant of 55 ps. The spike at zero delay is not a plasma effect, but is due to four-wave mixing between the pump and probe and provides a convenient zero-delay marker. The four-wave mixing signal and the plasma reflected probe have different angular distributions so they can be separated if desired.

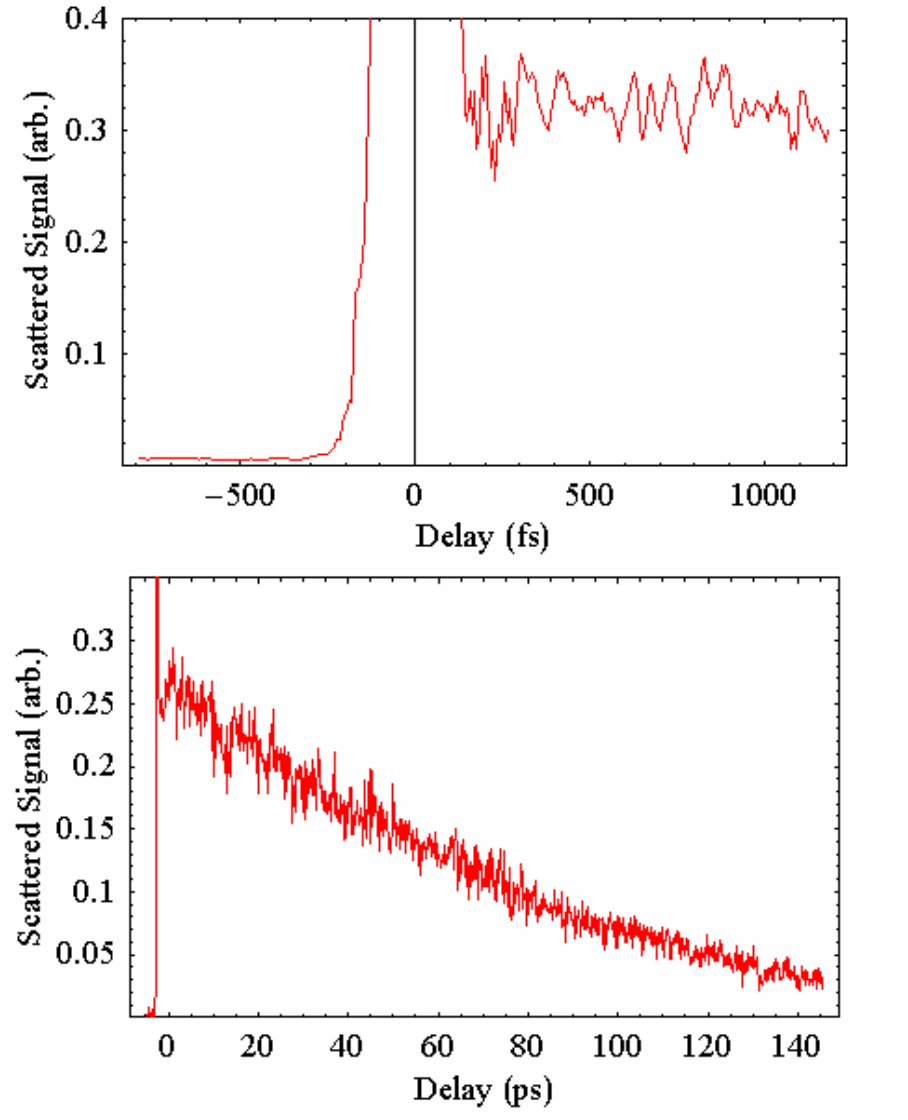

Figure 6.2 Reflected probe light when using a 3 mm path length in sapphire.

The four-wave mixing signal actually has an interferometric component (averaged out in the above figures) due to beating between different terms in the third-order nonlinear susceptibility (see Figure 6.3).

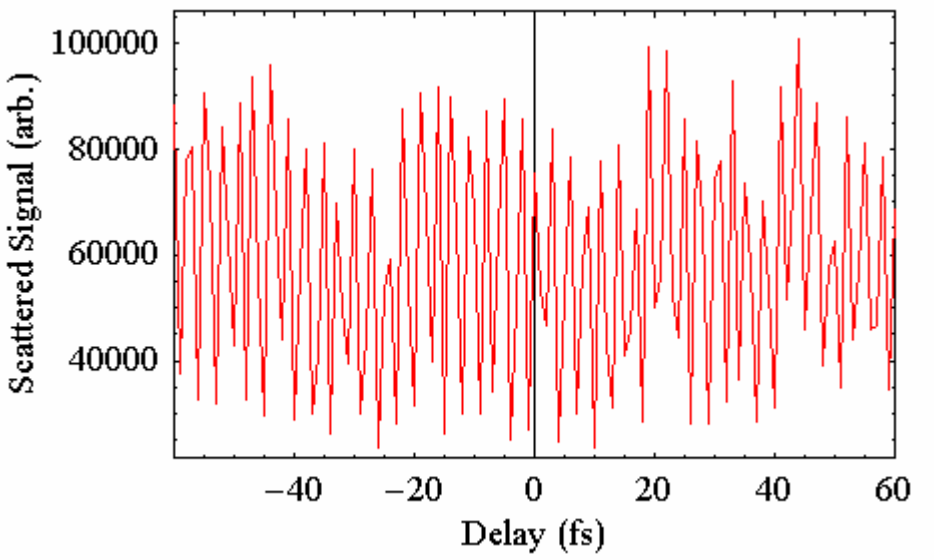

Figure 6.3 The four-wave mixing signal actually has an interferometric component due to beating between different terms in the third-order nonlinear susceptibility.

The reflected signal is significantly weaker than the forward scattered one, as it could be seen in Figure 6.4. Therefore the data showed throughout this thesis represents the forward scattered light unless stated otherwise. Analysis of the intensity and spectrum of the probe directly yields the excitation rate and other information. The path length is varied by simply translating the prism along the direction shown.

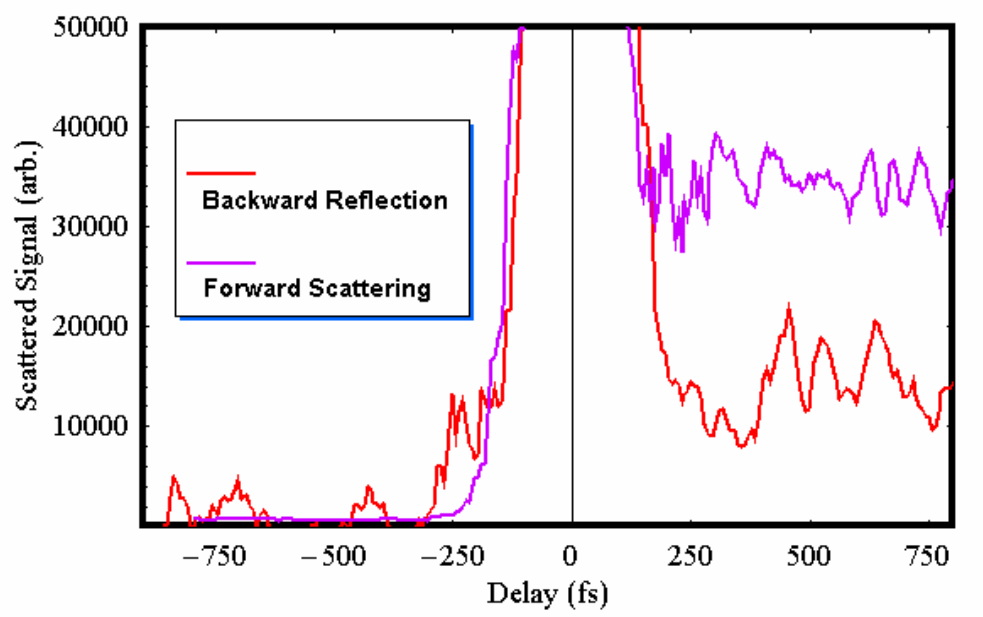

Figure 6.4 The weak probe pulse scatters from the plasma and can be detected in both the forward and backward directions. The reflected signal is significantly weaker as it can be seen in this picture for a propagation distance of 2.3 mm.

6.3 Experimental Results - Signal Structure, Supercontinuum Generation Threshold Distance

On first inspection it seems that the total path length through the crystal is constant as the prism is translated. However only the path length from the entrance to the hypotenuse contributes for experiments where continuum generation, self-focusing and all the other nonlinear processes are involved. It turns out the reflection from the hypotenuse disrupts the intense pulse nonlinear propagation. Path length dependence can be observed precisely in real time over a wide range of path lengths. The validity of the

technique was verified in several ways. First, the results were compared to standard optical window samples at 0.2, 1.0 and 3.0 mm for sapphire and found to be similar (see Figure 6.5).

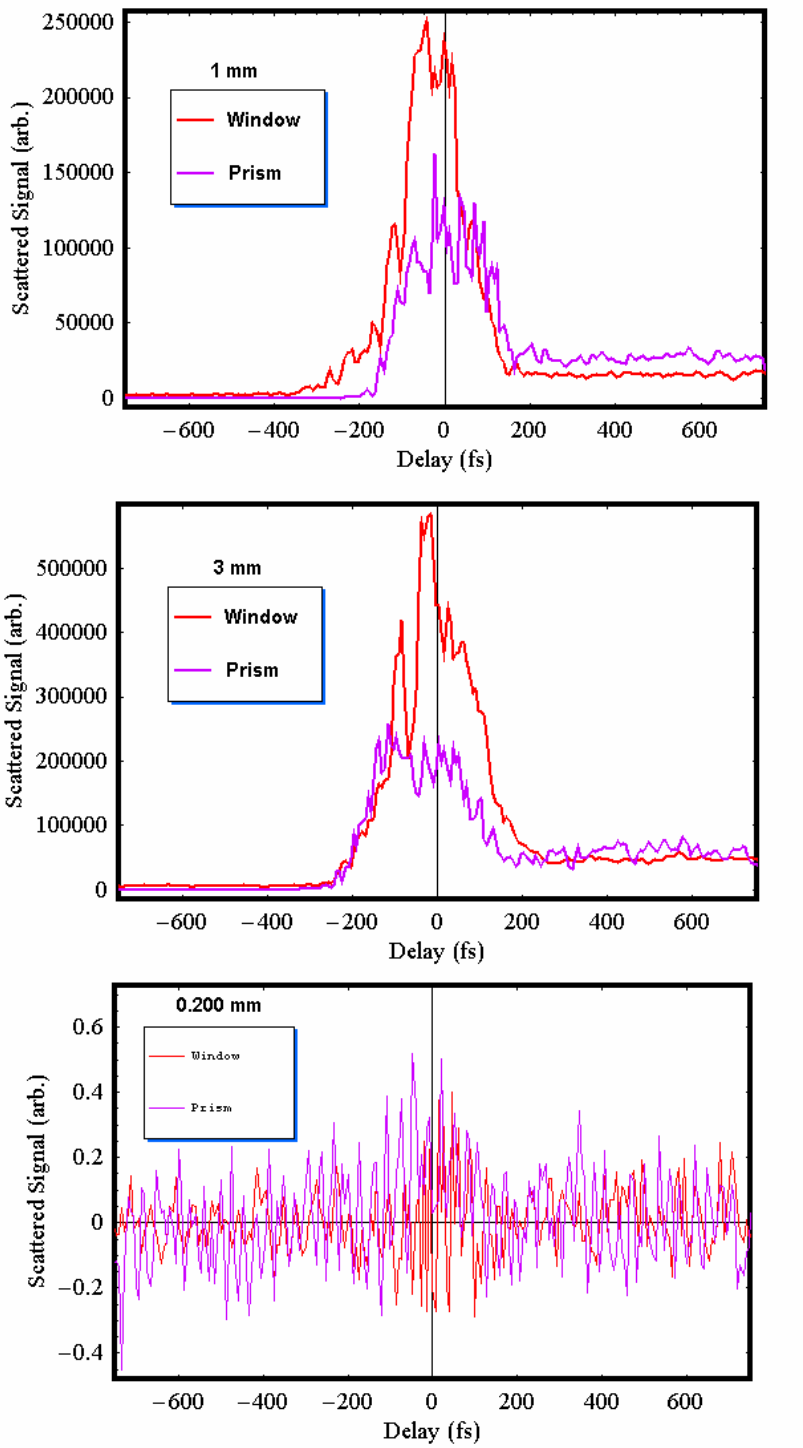

Figure 6.5 The prism results were compared to standard optical flat samples at 1.0 and 3.0 mm for sapphire and fused silica and were found to be similar.

Second, threshold behavior was observed for continuum generation and plasma formation for small path length changes (< 50 μm). If the path length was indeterminate because of propagation after the hypotenuse, this would not be the case (see Figure 6.6). And third, light was injected at an angle so that transmission through the hypotenuse did occur. This causes significant distortion in the beam because of non-normal incidence on the entrance face. A signal could still be measured and was qualitatively similar to what we measured previously.

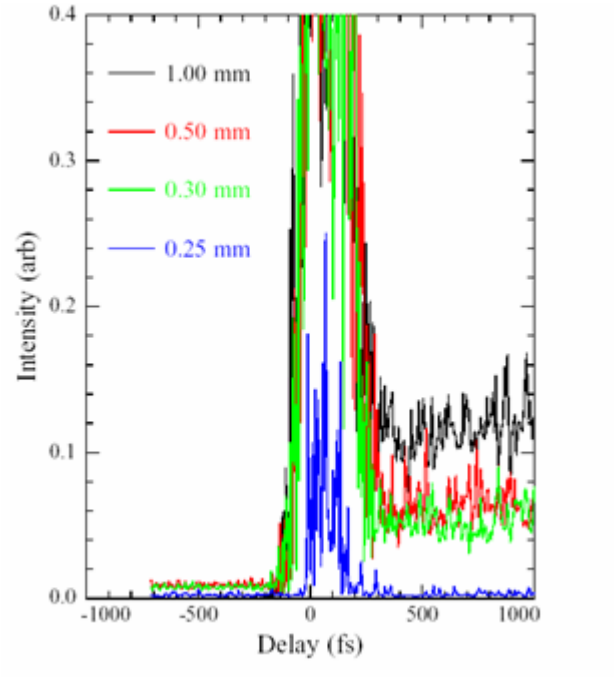

Figure 6.6 Threshold behaviors were observed for continuum generation and IFE for small path length changes (< 50 μm). If the path length was indeterminate because of propagation after the hypotenuse, this would not be the case.

Figure 6.6 shows propagation distance resolved data. It can be seen that there is a sharp drop between the 250 μm and 300 μm data. At 250 μm, the four-wave mixing signal is present, not being a threshold process, but no plasma is observed. Continuum generation also shuts off. The data indicate that for our focusing conditions the pulse requires 250 μm to begin drastic self-focusing. It then self-focuses over the next 50 μm and changes very little over the next 750 μm.

6.4 Scattered Signal versus Propagation Distance – Measurement of the Filament Length

We repeated the measurements described in the previous subsections for path lengths between 250 μm and 5.6 mm. The measurements were performed with a spatial resolution of 10 μm for propagation distances between 0.250 mm and 0.300 mm and with a resolution of 100 μm for path lengths between 0.300 mm and 2.1 mm. After a path length of 2.1 mm we increased the resolution up to 0.5 mm. The experimental results show that the signal increased rapidly over the first 1.8 mm and then remained constant up until a propagation distance of roughly 2.5 mm. After this point the signal varies widely and almost chaotically. Figure 6.7 shows the dependence of the scattered light on the propagation distance, for two different data sets.

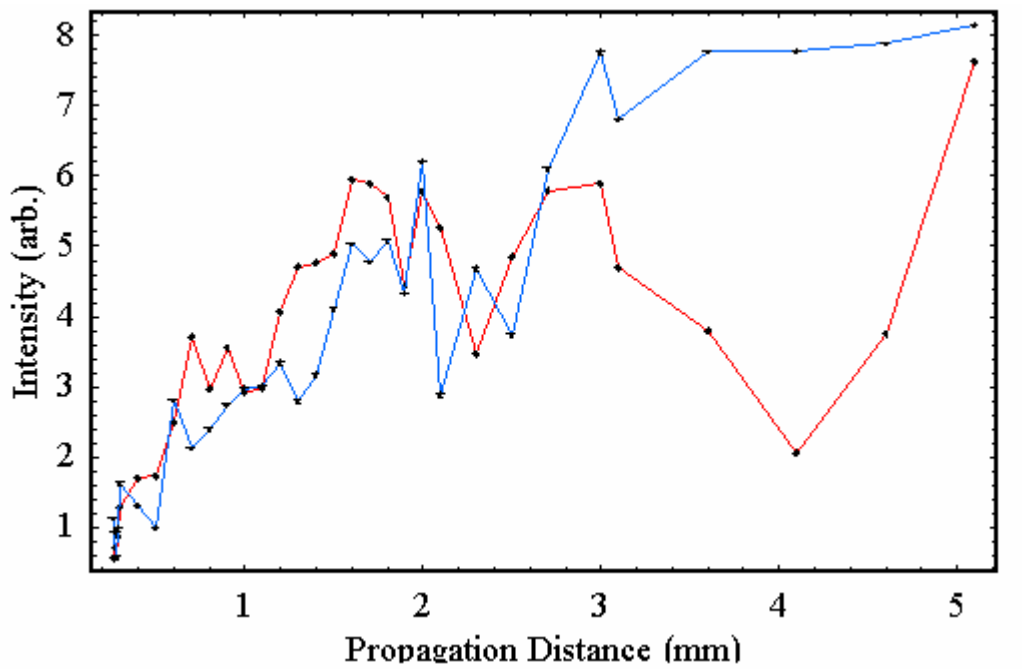

Figure 6.7 Scattered signal behavior was observed for various path length changes. The signal increased over roughly 1.8 mm and then it stayed almost constant up until 2.5 mm.

We know that the scattered signal depends on both the density and the size of the plasma. We have seen that the light self-focuses over the first 50 μm and then collapses down to a filament. The density is clamped down to a constant value inside the filament and therefore is reasonable to assume that the increase in the scattered signal is due to the increase in the filament length. We estimate that under our experimental conditions a filament of approximately 1.8 – 2.0 mm was formed. After this distance diffraction takes over and the filament breaks, the result being a chaotic behavior in our scattered signal.

6.5 Spectrally Resolved Plasma Signal

The prism technique described above is also used to study the spectrum of the scattered plasma signal. In this case, the forward scattered light is spectrally resolved using a spectrometer. The scattered probe intensity, essentially proportional to the plasma density, is measured as a function of pump-probe pulse delay and path-length. Representative data for sapphire are shown in Figure 6.8.

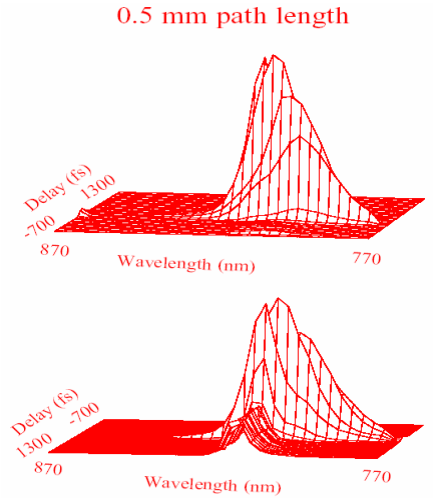

Figure 6.8 Spectrally resolved signal for a propagation distance of 0.5 mm.

At large negative delays, the probe comes first and so no signal is observed. At small negative delays, the probe samples the leading edge of the pump and suffers a large blue shift - this is the signature of plasma generation and is due to the time-varying decrease in the index of refraction as IFE takes place. Near zero delay there is significant

broadening to the blue and red due to cross-phase modulation, plasma effects and four-wave mixing. At large positive delays, the probe scatters from the slowly decaying plasma and experiences little or no spectral modification. Figure 6.9 shows spectra of the scattered signal at various propagation distances.

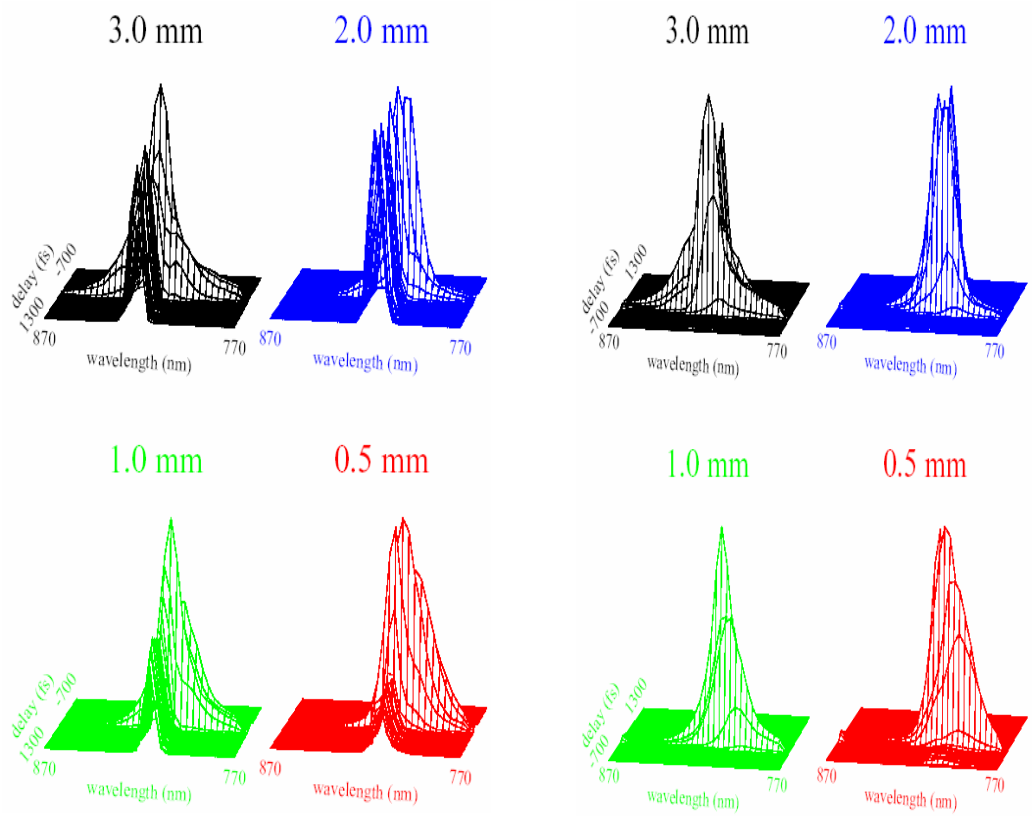

Figure 6.9 Spectrally resolved signal for various propagation distances.

It can be clearly seen that the spectra maintain the same structure for all the propagation distances. However, for large distances we observe an increased contribution from other processes (cross-phase modulation, for example). In conclusion, if we want to

study and separate the process of plasma formation from all the other phenomena, we must use thin samples. We can take a closer look at the 3D data by observing spectra of the scattered light at selected delay times (see Figures 6.10 and 6.11).

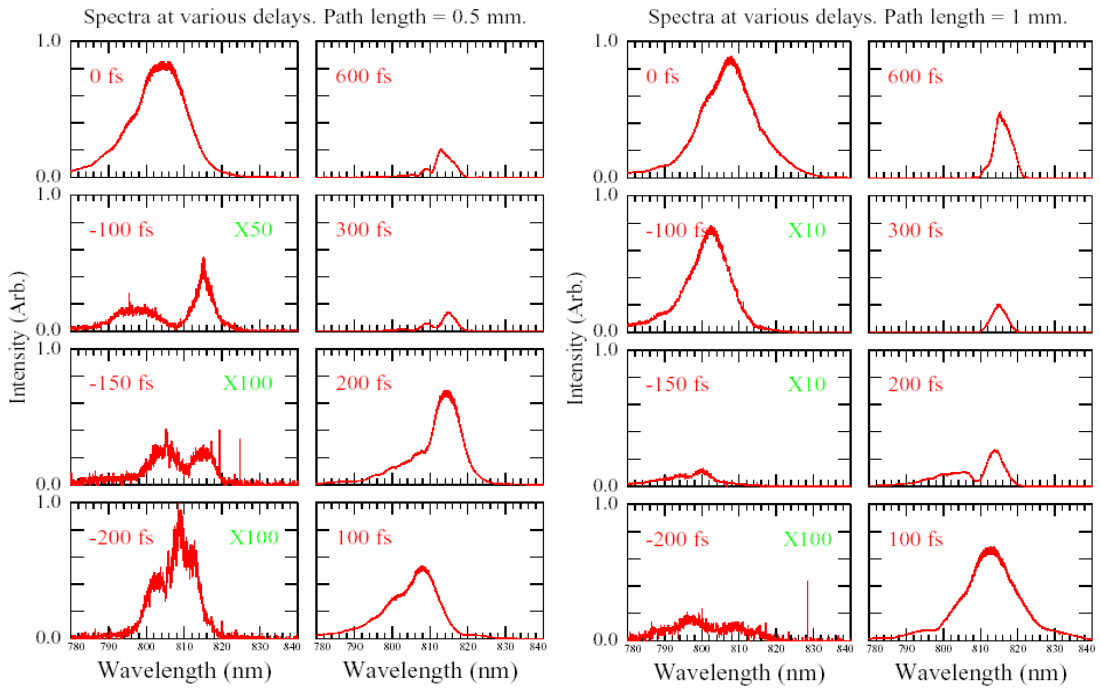

Figure 6.10 Selected spectra from Figure 6.9. The delay for the spectra and the relative size of the signal are indicated in each graph.

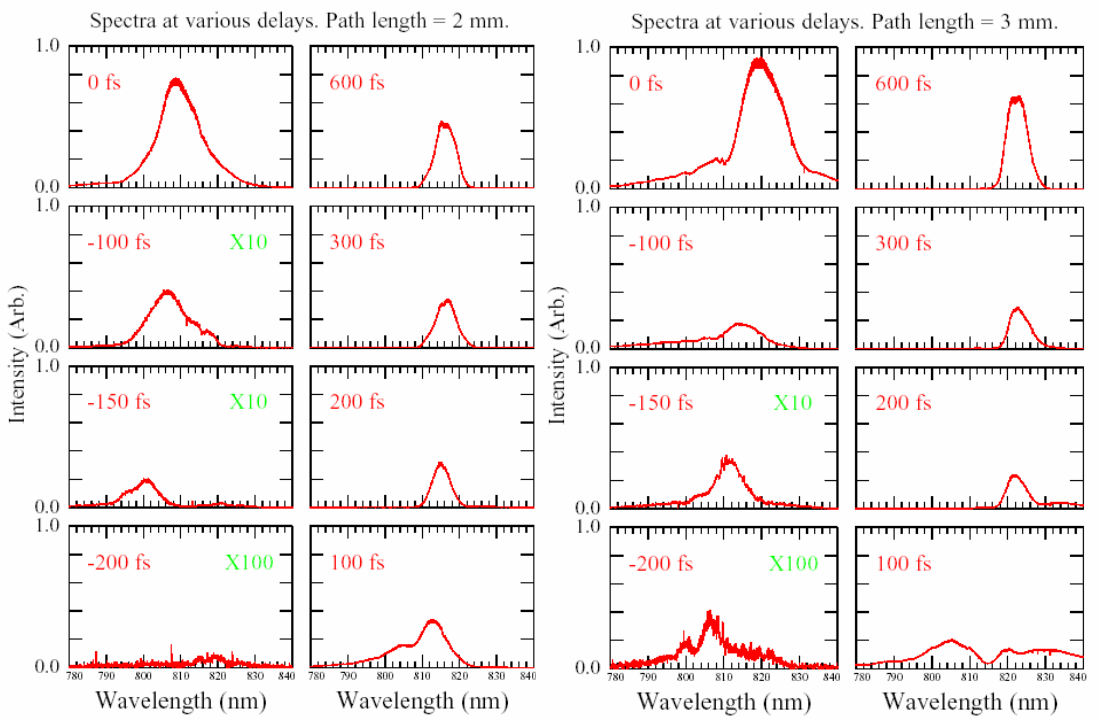

Figure 6.11 Selected spectra from Figure 6.9. The delay for the spectra and the relative size of the signal are indicated in each graph.

The measured spectra provide a wealth of quantitative and qualitative information. We can monitor, at each delay, how the probe light was affected by the interaction with the electron plasma. Moreover, we can actually read the plasma induced blue shifting at each pump-probe delay, for each propagation length. The results are summarized in Figure 6.12.

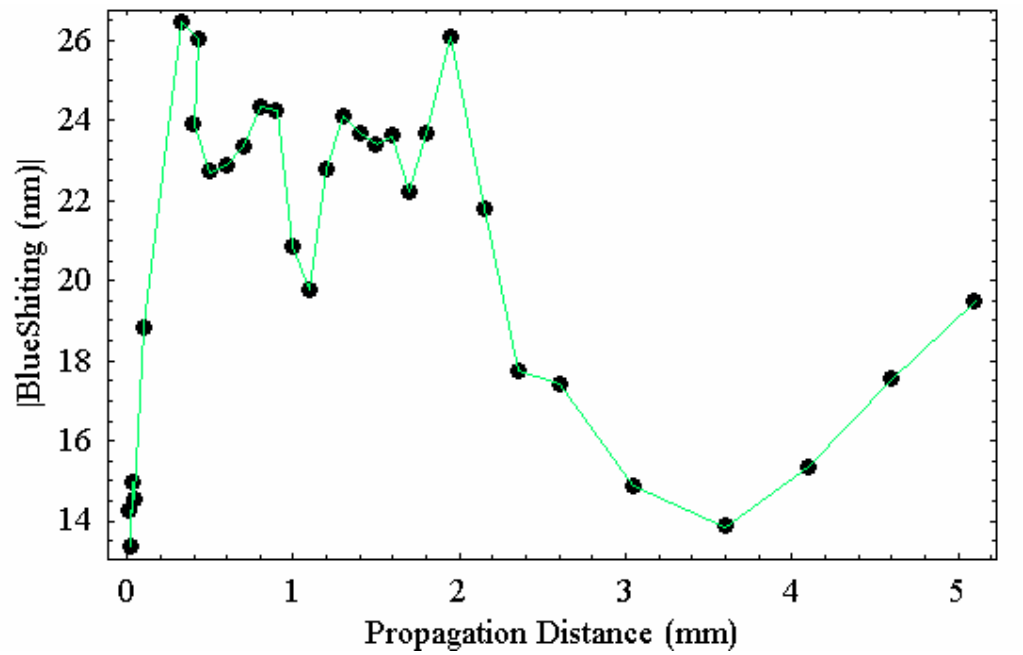

Figure 6.12 Plasma induced blue shifting for various propagation distances. The blue shifting increases rapidly over the first 50 μm, stays constant up until 2 mm and then decreases.

The blue shifting increased rapidly over the first 50 μm, suggesting that electron density increased rapidly in time over the same distance. This is in good agreement with the observation that the light self-focuses over a distance of 50 μm. Once the light forms a filament, the ionization rate inside the plasma column is constant, hence a constant blue shift at each path length up to 1.8 – 2.0 mm. After 2 mm the filament is destroyed, the intensity of the light drops dramatically and so do the ionization rate and the amount of blue shifting. This is a very important piece of information since it enables us to correctly use this "threshold" distance when calculating the ionization rates.

In conclusion we used an experimental technique that allowed us not only to monitor in real time the dynamics of the plasma formation, the changes induced in the spectrum of the plasma and the length of the filament, but also to obtain quantitative information (the amount of blue shifting) about the ionization rates inside the filament. This is a direct measurement and we get all the information without employing a theoretical model to fit our data and then extract numerical values for certain parameters related to plasma properties, as is the case with the damage studies, for example.

CHAPTER 7

CONCLUSIONS

The study of the interaction of ultrashort laser pulses with transparent materials is an active research area and will certainly continue for some time. The reasons are that the physics of the extremely nonlinear processes remains unknown and new applications drive more research in this area. Some unsolved issues are addressed in this thesis, but others still remain unsolved.

Using a pump-probe technique, electron plasmas were excited in several transparent materials by femtosecond laser pulses and plasma induced spectral modifications were observed. By measuring the plasma induced blue shifting, the peak ionization rates and conduction band electron densities were determined. In particular, we found that blue shifted spectra are determined by the strength of self-focusing in each material, the effect of the plasma defocusing and the band gap of the material. In our experiment we show that the time-delayed probe spectra provide a quantitative measure of the amount of plasma blue shifting and it is directly related to the electronic excitation

rate. The maximum blue-shifts were obtained in sapphire ($\Delta\lambda_{max} \sim 75$ nm), while in water ($\Delta\lambda_{max} \sim 28$ nm), fused silica ($\Delta\lambda_{max} \sim 32$ nm) and methanol ($\Delta\lambda_{max} \sim 26$ nm) the shifts were more modest. These values translate in ionization rates of the order of 10^{17}-10^{18} electrons/ ($fs^{-1} \cdot cm^{3}$). There is a widespread consensus in the field that in the ultra-short pulse regime, below the damage threshold, the dominant mechanism is the multiphoton ionization and that the avalanche ionization plays no role or its role is negligible. Our measured ionization rates are consistently larger that the theoretical rates given by Keldysh theory. This is in accord to what some research groups found, but it contradicted others.

Absorption experiments, that separate the two excitation processes and identify the relative role played by each in the ionization of the media, were also performed. The idea underneath these experiments is a very simple one: since the two ionization processes have different intensity dependence, the absorption of light in the medium should have a different dependence. Therefore it should be possible to distinguish the two mechanisms by looking at the energy dependence of the absorption. First observation is that we generated white light for each laser pulse wavelength employed except when using light at 400 nm. No matter how hard we pumped the sapphire crystal we could not damage it or generate other colors for this particular wavelength. We observed from the experimental results using light at 1200 nm, 800 nm and 590 nm that for small input energies the light simply propagated linearly; this region corresponded to a slope equal to 1. However, at the point where the continuum generation first appeared we observed a change of the slope in both set of data. There was a nonlinear slope in the curve that stoped exactly at the point where the continuum generation was fully formed. We

considered the nonlinear slope as an indication of a multiphoton process corresponding to an absorption that varies as I^k, with k being the number of photons required to cross the band gap. When the multiphoton process stoped, which was when the continuum generation fully developed, the slope changed to a sublinear one. We attributed this change in slope to a change in the ionization mechanism. From our result we could see that the avalanche ionization had a very important contribution (~ 70%) in sapphire and its contribution decreased (15% in methanol) as the band gap of the materials decreased. Our result challenges most of previous studies where the avalanche ionization was thought to play a minor role, if any and it separates, for the first time to our knowledge, the contribution of the two mechanisms to the creation of electrons in the conduction band in a solid.

LIST OF REFERENCES

1. John David Jackson, *Classical Electrodynamics* (John Wiley & Sons, New York, 1999).

2. S. A. Akhmatov and R. V. Khokhlov, Problems *of Nonlinear Optics* (Gordon and Breach Science Publishers, New York, 1972).

3. Robert W. Boyd, *Nonlinear Optics* (Academic Press, San Diego, 2003).

4. Govind P. Agrawal, Robert W. Boyd, *Contemporary Nonlinear Optics* (Academic Press, Boston, 1992).

5. Amnon Yariv, *Quantum Electronics*, (John Wiley & Sons, New York,1989)

6. James S. Carey, Eli N. Glazer and Eric Mazur, *Spectroscopy of Systems with Spatially Confined Structures* (R. Di Bartolo - Editor), (Kluwer Academic Publishers, Netherlands, 2003) , 213.

7. Mansoor Sheik-Bahae and Michael P. Hasselbeck, *OSA Handbook of Optics*, Vol. IV, Chapter 17, (2000).

8. Robert Guenther, *Modern Optics*, (John Wiley & Sons, New York, 1990).

9. B. La Fontaine, F. Vidal, Z. Jiang, C. Y. Chien, D. Corntois, A. Desparois, T. W. Johnston, J.-C. Kiefer, H. Pepin, H. P. Mercure, Phys. Plasmas **6**, 1815 (1999).

10. A. Dubietis, G. Tamosauskas, I. Diamin and A. Varanivicius, Opt. Lett **28**, 1269 (2003).

11. R. Y. Chiao, E. Garmire and C. H. Townes, Phys. Rev. Lett. **13**, 479 (1964).

12. J. H. Marburger, Prog. Quantum. Electron. 4, **35** (1975).

13. Alexander L. Gaeta, Phys. Rev. Lett. **84**, 3582 (2000).

14. D. Ashkenasi, A. Rosenfeld, H. Varel, M. Wahmer, E.E.B. Campbell, Appl. Surface Science **120**, 65 (1997).

15. A. Brodeur and S. L. Chin, J. Opt. Soc. Am. B. **16**, 637 (1999).

16. A. Brodeur and S. L. Chin, Phys. Rev. Lett. **80**, 4406 (1998).

17. L. V. Keldysh, Sov. Phys. JETP **20**, 1307 (1965).

18. M. Lenzner, J. Kruger, S. Sartania, Z. Cheng, Ch. Spielmann, G. Mourou, W. Kautek and F. Krausz, Phys. Rev. Lett **80**, 4076 (1998).

19. Ming Li, Saipriya Menon, John P. Nibarger and George N. Gibson, Phys. Rev. Lett **82**, 2394 (1999).

20. S. Tzortzakis, L. Sudrie, M. Franco, B. Prade, A. Mysyrowicz, A. Cuairon and L. Berge, Phys. Rev. Lett. **87**, 213902 (2001).

21. L. Sudrie, A. Cuairon, M. Franco, B. Lamouroux, B. Prade, S. Tzortzakis and A. Mysyrowicz, Phys. Rev. Lett. **89**, 186601 (2002).

22. Helene Ward and Luc Berge, Phys. Rev. Lett. **90**, 053901 (2003).

23. A. Cuairon, L. Sudrie, M. Franco, B. Prade and A. Mysyrowicz, Phys. Rev. B **71**, 125435 (2005).

24. Q. Feng, J. V. Moloney, A. C. Newell, E. M. Wright, K. Cook, P. K. Kennedy, D. X. Hammer, B. A. Rockwell, C. R. Thompson, IEEE Journal of Quantum Electronics **33**, 127 (1997).

25. K. K. Thornber, J. Appl. Phys. **52**, 279 (1981).

26. S. C. Rae and K. Burnett, Phys. Rev. A **46**, 1084 (1992).

27. S. P. LeBlanc and R. Sauerbrey, J. Opt. Soc. Am. B **13**, 72 (1996).

28. R. R. Alfano, P. L. Baldeck, P. P. Ho, G. P. Agrawal, J. Opt. Soc. Am. B **6**, 824 (1989).

29. William M. Wood, Craig W. Siders and M. C. Downer, IEEE Transactions on Plasma Science **21**, 20 (1993).

30. Robert R. Alfano, *The Supercontinuum Laser Source*, (Springer-Verlag, New York, 1989).

31. R. R. Alfano, L. S. Shapiro, Phys. Rev. Lett. **24**, 584 (1970).

32. J. Kasparian, R. Sauerbrey, D. Mandelain, S. Niedermeier, J. Yu, J.-P. Wolf, Y.-B. Andre, M. Franco, B. Prade, S. Tzortzakis, A. Mysyrowicz, M. Rodriguez, H. Wille, L. Woste, Opt. Lett. **25**, 1397 (2000).

33. Chris B. Shaffer, *Interaction of Femtosecond Laser Pulses with Transparent Materials*, Ph.D. Thesis, (Harvard University, 2001).

34. U. Morgner, F. X. Krtner, S. H. Cho, Y. Chen, H. A. Haus, J. G. Fujimoto, E. P. Ippen, V. Scheuer, G. Angelow, T. Tschudi, Opt. Lett. **6**, 411 (1999).

35. E. Innerhofer, T. Sdmeyer, F. Brunner, R. Hring, A. Aschwanden, R. Paschotta, C. Hnninger, M. Kumkar, U. Keller, Opt. Lett. **28**, 367 (2003).

36. L. Krainer, R. Paschotta, S. Lecomte, M. Moser, K. J. Weingarten, U. Keller, IEEE J. Quantum Electronics **38**, 1331 (2002).

37. A. J. D. Maria, D. A. Stetser and H. Heynau, Appl. Phys. Lett. **8**, 174 (1966).

38. Douglass Schumacher, Notes for the Ultrafast Laser Techniques and Experimentation Class (The Ohio State University, 2002).

39. M. T. Asaki, Opt. Lett. **18**, 977 (1993).

40. Robert Szipocs, Karapat Ferencz, Christian Spielmann, Ferenc Krausz, Opt. Lett. **19**, 201 (1994).

41. U. Keller, Nature **424**, 831 (2003).

42. D. Strickland and G. Mourou, Opt. Comm. **56**, 219 (1985).

43. D. M. Simanovskii, H. A. Schwettman, H. Lee and A. J. Welch, Phys. Rev. Lett. **91**, 107601 (2003).

44. B. C. Stuart, M. D. Feit, A. M. Rubenchick, B. W. Shore and M. D. Perry, Phys. Rev. Lett. **74**, 2248 (1995).

45. An-Chun Tien, Sterling Backus, Henry Kapteyn, Margaret Murnane and Gerard Mourou, Phys. Rev. Lett. **82**, 3883 (1999).

46. S. Henz and J. Herrmann, Phys. Rev. Lett. **59**, 2528 (1999).

47. R. L. Fork, C. V. Shank, C. Hirlimann, R. Yen, W. J. Tomlinson, Opt. Lett. **8**, 1 (1983).

48. Baldassare Di Bartolo (Ed.), *Ultrafast Dynamics of Quantum Systems, Physical Processes and Spectroscopic Techniques* (Plenum Press, New York, 1998).

49. J. R. Marquès, J. P. Geindre, F. Amiranoff, P. Audebert, J. C. Gauthier, A. Antonetti, and G. Grillon, Phys. Rev. Lett. **76**, 3566 (1996).

50. C. Quoix, G. Grillon, A. Antonetti, J.-P. Geindre, P. Audebert and J.-C. Gauthier, European Journal of Physics, Appl. Phys. **5**, 163 (1999).

51. Jennifer L. Tate, *Intense Laser Propagation in Sapphire*, Ph.D. Thesis, (The Ohio State University, 2004).

52. C. A. Sacchi, J. Opt. Soc. Am. B **8**, 337 (1991).

53. C. H. Fan, J. Sun, J. P. Longtin, J. Appl. Phys. **91**, 2530 (2002).

54. A. P. Joglekar, H. Liu, G. J. Spooner, E. Meyhofer, G. Mourou, A. J. Hunt, Apl. Phys. B **77**, 25 (2003).

55. Mihaela Balu, Joel Hales, David J. Hagan and Eric W. Van Stryland, Opt. Express **10**, 3594 (2005).

56. Arkady Major, Fumiyo Yoshino, Irkalis Nikolakakos, J. Stewart Aitchison, Peter W. E. Smith, Opt. Lett. **29**, 602 (2004).

57. A. J. Taylor, G. Rodriguez, Tracy Sharp Clement, Opt. Lett. **21**, 1812 (1996).

58. W. Liu, S. L. Chin, O. Kosareva, I. S. Golubtsov, V. P. Kandidov, Opt. Comm. **225**, 193 (2003).

59. D. Du, X. Liu, G. Korn, J. Squier, G. Mourou, Appl. Phys. Lett. **64**, 3071 (1994).

60. S. Guizard, P. Martin, G. Petite, O. Gobert, P. Meynadier, M. Perdrix, Appl. Phys. Lett. **68**, 459 (1999).

61. N. V. Ashcroft and N. D. Mermin, *Solid State Physics* (Holt, Rinehart and Winston, Ney York, 1976).

62. T.-W. Yau, C.-H. Lee, J. Wang, J. Opt. Soc. Am. B **17**, 1626 (2000).

63. Z. Wu, H. Jiang, L. Luo, H. Guo, H. Yang and Q. Gong, Opt. Lett. **27**, 448 (2002).

64. A. Dubietis, E. Gaizuskas, G. Tamosauskas and P. Di Trapani, Phys. Rev. Lett. **92**, 253903 (2004).

65. A. Dubietis, E. Kucinskas, G. Tamosauskas, E. Gaizuskas, M. A. Porras and P. Di Trapani, Opt. Lett. **29**, 2893 (2004).

66. S. L. Chin, La Physique du Canada **60**, 273 (2004).

67. J. Kasparian, M. Rodriguez, G. Méjean, J. Yu, E. Salmon, H. Wille, R. Bourayou, S. Frey, Y.-B. André, A. Mysyrowicz, R. Sauerbrey, J.-P. Wolf, L. Wöste, Science **301**, 61 (2003).

68. Jiung-Cheung Wang and Juen-Kai Wang, J. Opt. Soc. Am. B **21**, 45 (2005).

69. Masatoshi Saruwatari, IEEE JST **6**, 1363 (2000).

70. Th. Udem, S.A. Diddams, K. R. Vogel, C. W. Oates, E. A. Curtis, W. D. Lee, W. M. Itano, R. E. Drullinger, J. C. Bergquist and L. Hollberg, Phys. Rev. Lett. **86**, 4996 (2001).

71. David J. Jones, Scott A. Diddams, Jinendra K. Ranka, Andrew Stentz, Robert S. Windler, John L. Hall and Steven T. Cundiff, Science **288**, 635 (2000).

72. J.-F. Lami, S. Petit and C. Hirliman, Phys. Rev. Lett. **82**, 1032 (1999).

73. G. Fibich, Phys. Rev. Lett. **76**, 4356 (1996).

74. Juen Wang, *Femtosecond Nonlinear Optics in Gases and Solids*, Ph.D. Thesis, (Harvard University, 1992).

75. Yu. P. Raizer, *Laser-Induced Discharge Phenomena* (Plenum Publishing, New York, 1977).

76. W. L. Smith, P. Liu and N. Bloemberger, Phys. Rev. A **15**, 2396 (1977).

77. N. Bloemberger, Opt. Comm. **8**, 285 (1973).

78. G. Mechain A. Couairon, M. Franco, B. Prade, and A. Mysyrowicz, Phys. Rev. Lett. **93**, 035003 (2004).

79. F. H. M. Faisal, J. Phys. B **6**, L89 (1973).

80. H. R. Reiss, Phys. Rev. A **22**, 1786 (1980).

81. M. V. Ammosov, N. B. Delone and V. P. Krainov, Sov. Phys. JETP **64**, 1191 (1965).

82. K. D. Moll and Alexander L. Gaeta, Opt. Lett. **29**, 995 (2004).

83. A. Matijosius, J. Trull, P. Di Trapani, A. Dubietis, R. Pirskarskas, A. Varanavicius and A. Piskarskas, Opt. Lett. **29**, 1123 (2004).